Triple oxygen isotope ratios of bioapatite

Dissertation

zur Erlangung des mathematisch-naturwissenschaftlichen Doktorgrades
"Doctor rerum naturalium"
der Georg-August-Universität Göttingen

im Promotionsprogramm Geowissenschaften / Geographie
der Georg-August University School of Science (GAUSS)

vorgelegt von

Dingsu Feng

aus Renhuai (China)

Göttingen, 2022

Abstract

Bioapatite is the major crystalline component of bone and tooth materials. Recent studies demonstrated that bioapatite carries information of animals' physiology and living environmental conditions and retains its original isotope composition over millions of years. The triple oxygen isotope ratios of bioapatite for land-living mammals have proved to be a powerful tool to reconstruct paleo-atmospheric CO_2 concentration.

This thesis investigates variations in the triple oxygen isotope composition of bioapatite from a large collection of samples, including modern marine vertebrates, terrestrial mammals, birds and dinosaurs. In the following I will show and discuss: i) a new technique for high-precision triple oxygen isotope analysis of bioapatite; ii) a suite of triple oxygen isotope data of bioapatite from sharks and marine mammals; iii) a comprehensive triple oxygen isotope data set of terrestrial mammals with varying body sizes from different habitats; iv) triple oxygen isotope data for a collection of modern birds and dinosaurs from Late Cretaceous and Late Jurassic; vi) the methodology developed to obtain high precision triple oxygen isotope data.

This thesis is organized in 5 chapters. Chapter 1 contains background, state of the art and main definitions and notations used throughout the thesis.

In chapter 2, a new analytical protocol for high-precision triple oxygen isotope analyses is presented, together with triple oxygen isotope data of tooth enamel from 16 modern sharks and marine mammals. Results show that the analyzed sharks and mammals clearly separate from one another on a triple oxygen isotope plot. This is interpreted as the result of different proportions of metabolic oxygen in the bioapatite of marine vertebrates, i.e. more significant for marine mammals than for sharks. Data are then quantitatively discussed and interpreted in the framework of oxygen mass balance model for both sharks and marine mammals. Our data prove that triple oxygen isotope composition of bioapatite for, in particular, marine mammals is a suitable new proxy for the $\Delta'^{17}O$ of atmospheric O_2.

In chapter 3, a comprehensive set of triple oxygen isotope data form 127 modern terrestrial mammals is presented and discussed. The data set covers a wide range of body masses from different environments and living conditions. Taxon specific oxygen mass balance models are presented and compared with the measured data. The results indicate that, due to their higher metabolic rates, small mammals are more sensitive to changes in air $\Delta'^{17}O$ than large

mammals. This makes tooth enamel from small mammals a well suited archive for $\Delta'^{17}O$ of past atmospheric molecular O_2.

Chapter 4 contains triple oxygen isotope data of 11 modern birds and 9 dinosaurs. Modern birds' data show similar variations in $\Delta'^{17}O$ values to the terrestrial mammals. Hence, the mass balance model developed for terrestrial mammals is applied to estimate the oxygen isotopic balance of the studied dinosaurs. Fossil tooth enamel carries the O_2 anomaly of ancient atmospheric air and holds the potential to be used as a proxy to reconstruct atmospheric paleo-CO_2 levels. From the tooth enamel of four dinosaurs we estimate a Late Cretaceous atmospheric $p$$CO_2$ of 817 ± 579 ppmv. A higher atmospheric CO_2 level of 1605 ± 934 ppmv is obtained from the tooth enamel of five Late Jurassic specimens. These values are comparable to those reported in literature, obtained from different proxies.

Chapter 5 shows the different methods experimented and all the extensive tests conducted for obtaining high precision triple oxygen isotope data of bioapatite. Pros and cons of the different approaches are discussed and the novel method is explained in detail.

The final purpose of this thesis is threefold: to show that triple oxygen isotope data of tooth enamel from modern marine vertebrates and terrestrial mammals can be used to assess their physiology. To demonstrate that fossilized enamel of metabolically similar marine and terrestrial vertebrate is a new proxy for past atmospheric CO_2 and global primary productivity. To reconstruct the Mesozoic atmospheric CO_2 concentrations through high precision triple oxygen isotope analysis of tooth enamel from dinosaurs.

Acknowledgements

Table of contents

Table of Contents

Chapter 1 Introduction

1   Background

Svante A. Arrhenius (1859-1927) was the first to discuss that variations in atmospheric carbon dioxide (CO_2) concentrations are related to the large climate variability, which is evident from the geological record (Arrhenius, 1896). The study of the degree of coupling between atmospheric CO_2 and global temperature is one of the most important challenges of modern climate research. Reconstruction of past atmospheric CO_2 partial pressure (pCO_2) is vital to investigate the relevance of atmospheric CO_2 concentration as a potential driver of large temperature fluctuations during earth's history and the causality of the co-evolution of pCO_2 and climate change. Furthermore, accurate estimates of ancient Earth atmospheric CO_2 level during greenhouse periods is an essential tool for predicting the response of our planet to the modern intensive rise in CO_2 concentration.

Larger fluctuations in temperature and atmospheric CO_2 levels have been suggested for the Paleogene, the Mesozoic and the Precambrian (Bao et al., 2008). Temperatures are estimated on basis of the $\delta^{18}O$ of carbonates and pCO_2 are estimated by geochemical modeling (GEOCRAB, Berner and Kothavala, 2001; Berner, 2006; Berner, 2008) or from a variety of geological proxies. Several CO_2 proxies are widely applied, such as air inclusions in ice cores for the past 800,000 years (e.g., Petit et al., 1999; Lüthi et al., 2008; Foster et al., 2017), the carbon isotope composition of pedogenic minerals (Cerling, 1991; Ekart et al., 1999; Royer et al., 2001; Nordt et al., 2003; Lowenstein and Demicco, 2006; Retallack, 2009), the carbon isotope composition of phytoplankton (Pagani et al., 2005; Seki et al., 2010), the abundance of stomatal pores on fossil leaves (Retallack, 2001; Royer et al., 2001; Beerling and Royer, 2002; Fletcher et al., 2008; Smith et al., 2010), boron isotopes, and B-Ca ratios in carbonate shells (Pearson et al., 2009; Tripati et al., 2009; Seki et al., 2010).

Bao et al. (2008) presented a novel approach, based on triple oxygen isotope anomalies of sulfates, for the reconstruction of atmospheric pCO_2. The authors estimated a high pCO_2 level of ~ 12,000 ppm in the early Cambrian (750 Ma) and suggested that the sulphate $\Delta'^{17}O$ values can be useful in evaluating extreme levels of atmospheric CO_2 or O_2 that have occurred throughout Earth's history. Pack et al. (2013) reconstructed the atmospheric pCO_2 level from Eocene to Miocene on the basis of triple oxygen isotope composition of bioapatite from terrestrial mammals. The basic principle of this method is that mammals inhale air O_2 to

maintain their metabolism. Reaction products equilibrate with body water and transfer the oxygen isotope signature of air O_2 into the bones and tooth enamel.

For this thesis I have used a similar approach as in Pack et al. (2013) and conducted high-precision triple oxygen isotope analyses of bioapatite. I have here greatly extended the data set of Pack et al. (2013), by measuring the bioapatite of 164 different samples in total, including marine vertebrates, terrestrial mammals, birds and dinosaur fossils from Late Cretaceous and Late Jurassic. Moreover, I have developed a new analytical protocol which allows to reduce the $\Delta'^{17}O$ uncertainty down to ± 11 ppm.

Ultimate goals of this thesis are to use triple oxygen isotopes of bioapatite and mass balance modelling to understand the physiology of the extant and extinct animals, to demonstrate that the fossilized enamel of marine and terrestrial vertebrates is a valuable new paleo-CO_2 barometer, that can be used to estimate the Mesozoic atmospheric pCO_2.

2 Triple oxygen isotope systematics

2.1 Basic definitions

Oxygen is the third most abundant element in the solar system (Lodders, 2003). It has three stable isotopes with different natural abundances (^{16}O, 99.757%; ^{17}O, 0.038%; ^{18}O, 0.205%). Variations in isotope ratios are commonly expressed in form of the δ-notation (McKinney et al., 1950) given by:

$$\delta = \left(\frac{R_{\text{sample}}}{R_{\text{reference}}} - 1 \right) \times 1000$$
<div align="right">Eq. 1</div>

where R is the ratio of the heavy to light stable isotope in the sample and the reference material. Delta values are reported in per mil (‰).

Thus, for oxygen, R is given by $^{17}O/^{16}O$ and $^{18}O/^{16}O$ and their δ values are defined as:

$$\delta^{17}O^{\text{sample}}_{\text{VSMOW2}} = 1000 \times \left(\frac{(^{17}O/^{16}O)_{\text{sample}}}{(^{17}O/^{16}O)_{\text{VSMOW2}}} - 1 \right)$$
<div align="right">Eq. 2</div>

$$\delta^{18}O^{\text{sample}}_{\text{VSMOW2}} = 1000 \times \left(\frac{(^{18}O/^{16}O)_{\text{sample}}}{(^{18}O/^{16}O)_{\text{VSMOW2}}} - 1 \right)$$
<div align="right">Eq. 3</div>

Throughout this thesis, isotopic values are reported in the linearized notation, expressed by the following equations (Hulston and Thode, 1965; Young et al., 2002):

$$\delta'^{17}O^{sample}_{VSMOW2} = 1000 \times \ln \left(\frac{\delta^{17}O^{sample}_{VSMOW2}}{1000} + 1 \right)$$

$$\delta'^{18}O^{sample}_{VSMOW2} = 1000 \times \ln \left(\frac{\delta^{18}O^{sample}_{VSMOW2}}{1000} + 1 \right)$$

Isotope values are anchored to VSMOW2 using the composition of San Carlos olivine ($\delta^{18}O$ = 5.3‰ and $\Delta'^{17}O$ = -52 ppm, Pack et al., 2016; Sharp et al., 2016; Wostbrock et al., 2020).

2.2 The $\Delta'^{17}O$ parameter and the reference line

For oxygen mass-dependent fractionation processes, i.e. equilibrium and kinetic oxygen isotope exchange reactions, the mass-dependent fractionation law is characterized by the exponent relating the fractionation factors for $^{18}O/^{16}O$ and $^{17}O/^{16}O$ as (Young et al., 2002):

$$\frac{(^{17}O/^{16}O)_{sample}}{(^{17}O/^{16}O)_{VSMOW2}} = \left(\frac{(^{18}O/^{16}O)_{sample}}{(^{18}O/^{16}O)_{VSMOW2}} \right)^{\theta}$$

The exponent θ (Young et al. (2022) used a different terminology β) differs for equilibrium and kinetic fractionation processes because kinetic fractionation results from differences in the effective molecular mass of the involved gases (or liquids) whereas equilibrium fractionation depends on the atomic masses of the involved isotopes. In theory, the exponent θ value vary between 0.50 to 0.53 (Young et al., 2002; Pack and Herwartz, 2014). In this study, the exponent for triple isotope fractionation between phase A and B, is presented as θ to indicate that the fractionation between any two phases follows well established steady thermodynamic rules.

Since θ is variable for different processes and at different boundary conditions, isotopic fractionation of oxygen may result in a deviation of a given phase from a defined reference line in the $\delta'^{17}O$ vs. $\delta'^{18}O$ space. This anomaly can be expressed as $\Delta'^{17}O$, defined by the following equation:

$$\Delta'^{17}O = \delta'^{17}O^{sample}_{VSMOW2} - \lambda_{RL} \times \delta'^{18}O^{sample}_{VSMOW2}$$

Where $\Delta'^{17}O$ represents the vertical offset from a given reference line (λ_{RL}) in a triple oxygen isotope plot (Figure 1, (I) and (II)). λ_{RL} = 0.528 is used throughout this work to enable direct comparability with most other triple oxygen isotope data reported in literatures (Meijer and Li, 1998; Luz and Barkan, 2010; Sharp et al., 2018; Passey and Ji, 2019; Whiteman et al., 2019).

Figure 1. (I): $\delta'^{17}O$ vs. $\delta'^{18}O$ plot, showing: the triple oxygen isotope composition of modern air O_2 (red star, Pack, 2021), a reference line with a slope $\lambda_{RL} = 0.528$ (solid black line), and the magnitude of the isotopic anomaly (i.e. $\Delta'^{17}O$) for modern air O_2 depicted as the vertical distance from the reference line. The fractionation between two generic phases, A and B (light blue solid circles), is indicated along with the triple isotope fractionation slope which represents the fractionation exponent (θ, solid grey line). (II): $\Delta'^{17}O$ vs. $\delta^{18}O$ diagram showing the oxygen isotope composition of modern air O_2 (red star, Pack, 2021) and the equilibrium fractionation relation between water and vapor at 25 °C (blue solid circles). The equilibrium fractionation exponent $\theta_{water-vapor}$ is obtained from Barkan and Luz (2005).

2.3   Equilibrium fractionation: θ and α

The exponent θ for equilibrium fractionation depends on the partition function ratio of the oxygen-bearing isotopologues. Triple oxygen isotope mass dependent fractionation is characterized by θ relating the two fractionation factors ($\alpha^{17/16}, \alpha^{18/16}$). These two fractionation factors of the coexisting phases A and B are defined as (Young et al., 2002):

$$\alpha_{A-B}^{17/16} = \frac{\delta^{17/16}O_A + 1000}{\delta^{17/16}O_B + 1000} \qquad \text{Eq. 8}$$

$$\alpha_{A-B}^{18/16} = \frac{\delta^{18/16}O_A + 1000}{\delta^{18/16}O_B + 1000} \qquad \text{Eq. 9}$$

The two fractionation factors are related by the power law:

$$\alpha_{A-B}^{17/16} = \left(\alpha_{A-B}^{18/16}\right)^{\theta_{A-B}} \qquad \text{Eq. 10}$$

Values for θ vary depending upon the process (Figure 1, (I) and (II)). So far, the experimental results for equilibrium fractionation processes are still rare.

Figure 2: Overview of equilibrium exponent (θ) for different equilibrium process. Open symbols are based on the experimental studies, solid symbols are based on the theoretical predictions.

For apatite-water fractionation, Pack et al. (2013) determined a θ value of 0.523 ± 0.002 at 37 °C by using the rostral bone of a harbor porpoise (*Phocoena phocoena*), as shown in Figure 2. Hayles et al. (2018) presented new calibrations based on statistical thermodynamics and density functional theory for fluorapatite and water, yielding a value of $\theta = 0.5242$ at ~ 37 °C.

For silicate-water fractionation (5 °C), Sharp et al. (2016) presented a θ value of 0.5238 ± 0.0001. The respective theoretical estimate is $\theta = 0.5247$ at the same temperature (Hayles et al., 2018). For water-vapor fractionation (11 °C $\leqslant$ T $\leqslant$ 42 °C), θ was experimentally determined to 0.529 ± 0.001 (Barkan and Luz, 2005). For the CO_2-water equilibrium (2 °C $\leqslant$ T $\leqslant$ 37 °C), Hofmann et al. (2012) experimentally determined a $\theta = 0.522 \pm 0.002$. Recently, Cao and Liu (2011) showed theoretical values for CO_2-water, quartz-water and calcite-water equilibrium isotope exchange reactions, and at ~ 37 °C, the θ value for CO_2-water equals

0.5246. Guo and Zhou (2019) examined the systematics of triple oxygen isotope fractionation in the DIC-H_2O-CO_2 system, and at ~ 20 °C, θ value for HCO_3^- to water equals 0.5252.

3 Stable oxygen isotopes of bioapatite

3.1 Background of bioapatite studies

Abraham Gottlob Werner, a German geologist, was the first describing and naming this mineral back in 1788 in a scientific paper entitled *"Geschichte, Karakteristik, und kurze chemische Untersuchung des Apatits"*. The name apatite derives from the Greek word, which means "deceiver", and that because mineralogists had repeatedly misclassified up to that point.

Over the past 50 years, carbonates, and the phosphate group (PO_4^{3-}) in bioapatite ($Ca_{10-a}(Na,K,NH_4)_{2a}(PO_4)_{6-y}[(CO_3)_{2x+(3/2)y}(F,OH)_{2-2x}]$; modified after Fleet et al., 2004) have been utilized as a powerful archive for reconstruction of paleoclimate, paleoenvironment, paleodiet, migration, and thermo-physiology. Although carbonates are among the most frequently used materials for environmental and physiological reconstruction, phosphates are thought to be far more resistant to diagenesis alteration than carbonates, which makes them especially attractive for paleontological and geological applications (Longinelli and Nuti, 1973; Ayliffe and Chivas, 1990; Luz et al., 1990; Delgado Huertas et al., 1995; Koch et al., 1995; Fricke and O'Neil, 1996; Fricke, 2003; Crowley et al., 2008; Fricke et al., 2011; Pack et al., 2013; Passey et al., 2014).

3.2 The $\delta^{18}O$ of apatite

It has been proved that marine phosphate forms in equilibrium with ambient water (Kolodny et al., 1983; Shemesh et al., 1983). In these studies $\delta^{18}O$ values of phosphate were used to reconstruct ocean temperatures and the samples have demonstrated that phosphates are resistant to diagenesis. Longinelli and Nuti (1973) first envisioned using oxygen isotope data of bones and teeth from mammals to determine meteoric water values in ancient continental environments. Later on, Longinelli (1984) and Luz et al. (1984) presented simple mass-balance box models for relationship between the body water and the drinking water $\delta^{18}O$, following the idea that – for a confined system – the overall isotopic composition of all input fluxes must be equal to the isotopic composition of the sum of fluxes leaving the system. Since then, $\delta^{18}O$ values of mammalian bone and tooth enamel have been widely used for various applications, such as reconstructing precipitation and relative humidity (Ayliffe and

Chivas, 1990; Luz et al., 1990; Cormie et al., 1994; Delgado Huertas et al., 1995), seasonal climate variations and ecology (Koch et al., 1989; Bryant and Froelich, 1995; Sharp and Cerling, 1998), diet, habitat and migration (Koch et al., 1995; Fricke and O'Neil, 1996; Kohn, 1996; Fricke, 2003; Crowley et al., 2008; Fricke et al., 2011). For example, Ayliffe and Chivas (1990) found that the $\delta^{18}O$ of kangaroos and macropods correlate with environmental relative humidity. Luz et al. (1990) presented variations in $\delta^{18}O$ of phosphate from deer bones serve as proxies for local relative humidity and precipitation. Bryant and Froelich (1995) used $\delta^{18}O$ of fossil biogenic phosphate for paleoclimate reconstruction. Kohn (1996) modelled that the $\delta^{18}O$ values of terrestrial and aquatic animals account for diet and physiological adaptation. $\delta^{18}O$ heterogeneity in tooth enamel values was reported for animals with different behaviors and physiological parameters (Levin et al., 2006). The turnover of oxygen in the body water ($\delta^{18}O$) in small mammals was explored by Podlesak et al. (2008). Blumenthal et al. (2017), using tooth enamel values of modern and fossil mammals, showed that past climates were similar to the climate in eastern Africa today.

3.3   The $\Delta'^{17}O$ of apatite

It is worth noting that the above reported studies are limited exclusively to $\delta^{18}O$ analysis. Explanation for this is that it was long believed that no additional information could be obtained from the $\delta^{17}O$ value of a sample. Isotopic fractionation associated with the overwhelming majority of physical and chemical processes on Earth results, in fact, in changes of the $^{17}O/^{16}O$ ratio by approximately half the magnitude of the corresponding changes in the $^{18}O/^{16}O$ ratio. Furthermore, being ^{17}O the rarest among the three stable isotopes of oxygen, precise determinations of $\delta^{17}O$ values of rock and minerals present some complexities. These include extensive cleaning of O_2 gas through cryofocusing and gas chromatography before its introduction into the inlet system of a mass spectrometer.

Pack et al. (2013) first suggested that $\Delta'^{17}O$ of bioapatite of land-living mammals can be used as a proxy for the $\Delta'^{17}O$ of ambient air and hence pCO$_2$. Mammals consume metabolic O_2 to burn carbohydrate, fat, and protein. In the Earth's atmosphere, the formation of photochemical ozone is a mass independent fractionation (MIF) process, which results in a negative ^{17}O isotope anomaly in air O_2 (Heidenreich and Thiemens, 1986; Figure 1, red star). The anomaly of air O_2 is transferred to the metabolic reaction products CO_2 and H_2O. Both, CO_2 and H_2O equilibrate with body water, so the initial anomaly is transferred from inhaled air O_2 to body water of mammals (or other air-breathing animals). Bioapatite crystallizes in

isotopic equilibrium with body water (Figure 3). It has been proposed by Yung et al. (1991) and observed by Blunier et al. (2002) that the $\Delta'^{17}O$ of air O_2 varies with atmospheric CO_2 concentrations. Higher than modern CO_2 concentrations results in lower $\Delta'^{17}O$ values (i.e., larger anomaly) of O_2, whereas lower CO_2 leads to a smaller ^{17}O anomaly of air O_2. Apart of atmospheric CO_2 concentration, $\Delta'^{17}O$ of atmospheric O_2 also depends on the global primary production (GPP; Luz et al., 1999; Young et al., 2014). So the reconstruction of $\Delta'^{17}O$ of paleo air O_2 may provide information on the atmospheric CO_2 concentrations at that time. Bioapatite partly incorporates anomalous air O_2 and, hence, may be used for pCO_2 reconstruction (Pack et al., 2013; Gehler et al., 2016).

Passey et al. (2014) and Lehmann et al. (2021) report high-precision $\Delta'^{17}O$ datasets of vertebrate biogenic carbonates and proposed the application of $\Delta'^{17}O$ for paleoenvironmental studies of continental environments where vertebrate body water may record an isotopic signal of evaporated water sources and atmospheric oxygen. Whiteman et al. (2019) suggested that $\Delta'^{17}O$ of mammal bioapatite provides direct insights into the metabolic rates.

Figure 3: Sketch illustrating how the air O_2 is transferred via the body water into bioapatite. The mammals inhale air O_2 and the anomaly ($\Delta'^{17}O$) of air O_2 is transferred to body water, then recorded in the tooth enamel. Due to this relationship, the inhaled air oxygen composition can be derived from tooth enamel. The $\Delta'^{17}O$ of air O_2 correlates with atmospheric concentration (pCO_2) and global primary production (GPP). Hence, the isotopic

composition of bioapatite carries information on the atmospheric $p\text{CO}_2$. Combining oxygen mass balance models with the inhaled air O_2 data allows for the calculation of the bioapatite composition.

4   Carbonate isotopes

4.1   Basic definition

Besides its phosphate group, bioapatite also contains a carbonate group (CO_3^{2-}). Carbon has two stable isotopes with different natural abundances (^{12}C, 98.93%; ^{13}C, 1.07%). In analogy to equations 2 and 3, the $\delta^{13}C$ (reported in permille) is defined as:

$$\delta^{13}\text{C} = \left(\frac{(^{13}\text{C}/^{12}\text{C})_{\text{sample}}}{(^{13}\text{C}/^{12}\text{C})_{\text{VPDB}}} - 1 \right) \times 1000 \qquad \text{Eq. 21}$$
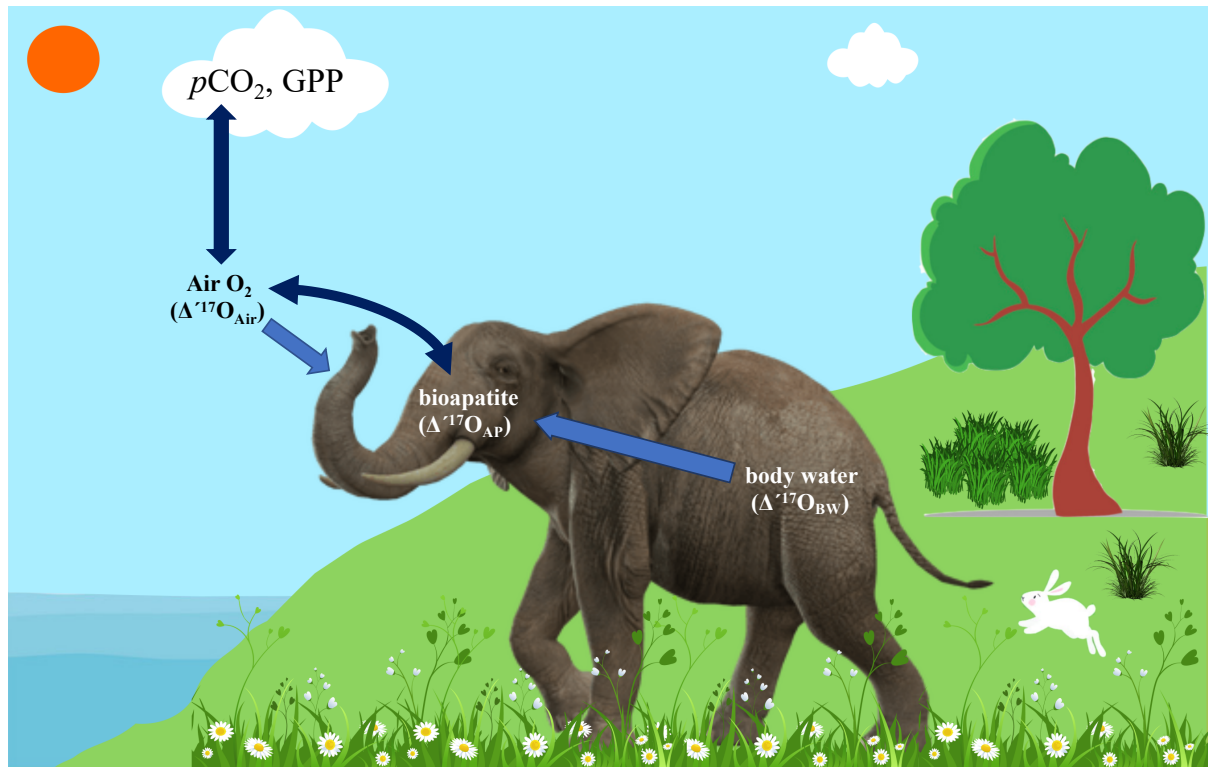
The abbreviation VPDB stands for Vienna Pee Dee Belemnite, the international reference material for carbon isotope studies.

4.2   Stable carbon isotopes in bioapatite

Carbon isotopes of bioapatite are widely used to reconstruct paleoclimatic conditions and paleodiet. Dietary reconstruction is important for paleontological and archaeological studies, especially for those on extinct animals.

The isotopic composition of plant food ingested by mammals carries information about environmental conditions. Different type of vegetation cover, physiological behaviors, niche partitioning, and $\delta^{13}C$ in the ingested food are well recorded in bioapatite. Deniro and Epstein (1978a; 1978b) first presented that $\delta^{13}C$ of bone in two sympatric hyrax species show evidence for different feeding patterns and $\delta^{13}C$ is mainly controlled by ingested food. Ericson et al. (1981) and Sullivan and Krueger (1981) applied the $\delta^{13}C$ of fossil mammals' bone for dietary reconstructions. Since then, a large number of studies has been presented using the $\delta^{13}C$ in bioapatite for both modern and fossil mammals (e.g. Kohn, 1996; Cerling et al., 1997; Sharp and Cerling, 1998; MacFadden et al., 1999; Kohn et al., 2005; Tütken and Vennemann, 2009).

5   Focus of study

The aim of this thesis is to reconstruct the $p\text{CO}_2$ concentrations using the triple oxygen isotope composition of bioapatite as a proxy. To do so, I explored the triple oxygen isotopic compositions of teeth from sharks and marine mammals, terrestrial mammals, modern birds,

and fossil samples from the Late Cretaceous and Late Jurassic. The thesis is subdivided into 4 main parts:

Chapter 2: Isotopically anomalous metabolic oxygen in marine vertebrates as physiology and atmospheric proxy

The analytical protocol for high-precision triple oxygen analyses of bioapatite is explored and it is demonstrated that traces of anomalous respired oxygen can be found in sharks and marine mammals whereas differences between gill-breathing sharks and lung-breathing marine mammals are observed. This study also explores the usability of triple oxygen isotopes analysis of marine vertebrates as a new tool for physiological studies and clarifies if ^{17}O in fossil tooth enamel of marine vertebrates can be used as a new proxy archive for past pCO$_2$ and *GPP*.

Chapter 3: Triple oxygen isotopes of modern terrestrial mammalian tooth enamel-new implications for paleoenvironmental and physiological research

To improve the understanding of extinct and extant animal physiology and behavior, detailed triple oxygen isotope mass balance models of modern terrestrial analogues covering a wide range of body masses, metabolic rates, and habitates are presented and compared to experimental data.

Chapter 4: Triple oxygen based reconstruction of Mesozoic atmospheric CO$_2$ concentrations from dinosaur tooth enamel

To reconstruct Late Cretaceous and Late Jurassic pCO$_2$ concentrations, different dinosaurs' tooth enamel samples from both geological periods were collected and analyzed for their triple oxygen isotopic signals. To explore the physiology of the extinct dinosaurs, modern birds' bioapatite triple oxygen isotope data were added to the sample set.

Chapter 5: Techniques for high-precision analysis of triple oxygen isotope ratios of bioapatite

In order to investigate the best approach to analyze oxygen from the phosphate group in bioapatite and for obtaining high precision data, different techniques are tested and presented. The successful analytical protocol is discussed in detail along with problems and analytical difficulties.

6   References

Arrhenius S. (1896) On the Influence of Carbonic Acid in the Air Upon the Temperature of the Ground. **5**, 1–15.

Ayliffe L. K. and Chivas A. R. (1990) Oxygen isotope composition of the bone phosphate of Australian kangaroos: Potential as a palaeoenvironmental recorder. *Geochim. Cosmochim. Acta* **54**, 2603–2609.

Bao H., Lyons J. R. and Zhou C. (2008) Triple oxygen isotope evidence for elevated CO_2 levels after a Neoproterozoic glaciation. *Nature* **453**, 504–506.

Barkan E. and Luz B. (2005) High precision measurements of $^{17}O/^{16}O$ and $^{18}O/^{16}O$ ratios in H_2O. *Rapid Commun. Mass Spectrom.* **19**, 3737–3742.

Beerling D. J. and Royer D. L. (2002) Fossil plants as indicators of the phanerozoic global carbon cycle. *Annu. Rev. Earth Planet. Sci.* **30**, 527–556.

Berner R. A. and Kothavala Z. (2001) Geocarb III: A revised model of atmospheric CO_2 over phanerozoic time. *Am. J. Sci.* **301**, 182–204.

Berner R. A. (2006) GEOCARBSULF: A combined model for Phanerozoic atmospheric O_2 and CO_2. *Geochim. Cosmochim. Acta* **70**, 5653–5664.

Berner R. A. (2008) Addendum to "Inclusion of the Weathering of Volcanic Rocks in the GEOCARBSULF Model": (R. A. Berner, 2006, V. 306, p. 295-302). *Am. J. Sci.* **308**, 100–103.

Blunier T., Barnett B., Bender M.L., Hendricks M.B. (2002) Biological oxygen productivity during the last 60,000 years from triple oxygen isotope measurements. *Global Biogeochemical Cycles* **16**, 1-13.

Blumenthal S. A., Levin N. E., Brown F. H., Brugal J. P., Chritz K. L., Harris J. M., Jehle G. E., Cerling T. E. and O'Connell J. (2017) Aridity and hominin environments. *Proc. Natl. Acad. Sci. U. S. A.* **114**, 7331–7336.

Bryant D. J. and Froelich P. N. (1995) A model of oxygen isotope fractionation in body water of large mammals. *Geochim. Cosmochim. Acta* **59**, 4523–4537.

Cao X. and Liu Y. (2011) Equilibrium mass-dependent fractionation relationships for triple oxygen isotopes. *Geochim. Cosmochim. Acta* **75**, 7435–7445.

Cerling T. E. (1991) Carbon dioxide in the atmosphere: evidence from Cenozoic and Mesozoic paleosls. *Am. J. Sci.* **291**, 377–400.

Cerling T. E., Harris J. M., MacFadden B. J., Leakey M. G., Quade J., Eisenmann V. and Ehieringer J. R. (1997) Global vegetation change through the Miocene/Pliocene

boundary. *Nature* **389**, 153–158.

Cormie A. B., Schwarcz H. P. and Gray J. (1994) Relation between hydrogen isotopic ratios of bone collagen and rain. *Geochim. Cosmochim. Acta* **58**, 377–391.

Crowley B. E., Koch P. L. and Davis E. B. (2008) Stable isotope constraints on the elevation history of the Sierra Nevada Mountains, California. *Bull. Geol. Soc. Am.* **120**, 588–598.

Daniel Bryant J. and Froelich P. N. (1995) A model of oxygen isotope fractionation in body water of large mammals. *Geochim. Cosmochim. Acta* **59**, 4523–4537.

Delgado H.A., Iacumin P., Stenni B., Sánchez C.B. and Longinelli A. (1995) Oxygen isotope variations of phosphate in mammalian bone and tooth enamel. *Geochim. Cosmochim. Acta* **59**, 4299–4305.

Deniro M. J. and Epstein S. (1978a) Carbon isotopic evidence for different feeding patterns in two hyrax species occupying the same habitat. *Science (80-.).* **201**, 906–908.

Deniro M. J. and Epstein S. (1978b) Influence of diet on the distribution of carbon isotopes in animals. *Geochim. Cosmochim. Acta* **42**, 495–506.

Ekart D. D., Cerling T. E., Montañez I. P. and Tabor N. J. (1999) A 400 million year carbon isotope record of pedogenic carbonate: Implications for paleoatmospheric carbon dioxide. *Am. J. Sci.* **299**, 805–827.

Ericson J. E., Sullivan C. H. and Boaz N. T. (1981) Diets of Pliocene mammals from Omo, Ethiopia, deduced from carbon isotopic ratios in tooth apatite. *Palaeogeogr. Palaeoclimatol. Palaeoecol.* **36**, 69–73.

Fleet, M. E., Liu, X., and King, P. L. (2004) Accommodation of the carbonate ion in apatite: An FTIR and X-ray structure study of crystals synthesized at 2–4 GPa. *American Mineralogist*, **89** 1422–1432.

Fletcher B. J., Brentnall S. J., Anderson C. W., Berner R. A. and Beerling D. J. (2008) Atmospheric carbon dioxide linked with Mesozoic and early Cenozoic climate change. *Nat. Geosci.* **1**, 43–48.

Foster G. L., Royer D. L. and Lunt D. J. (2017) Future climate forcing potentially without precedent in the last 420 million years. *Nat. Commun.* **8**, 1–8.

Fricke H. C. and O'Neil J. R. (1996) Inter- and intra-tooth variation in the oxygen isotope composition of mammalian tooth enamel phosphate: Implications for palaeoclimatological and palaeobiological research. *Palaeogeogr. Palaeoclimatol. Palaeoecol.* **126**, 91–99.

Fricke H. C. (2003) Investigation of early Eocene water-vapor transport and paleoelevation using oxygen isotope data from geographically widespread mammal remains. *Bull.*

Geol. Soc. Am. **115**, 1088–1096.

Fricke H. C., Hencecroth J. and Hoerner M. E. (2011) Lowland-upland migration of sauropod dinosaurs during the Late Jurassic epoch. *Nature* **480**, 513–515.

Gehler A., Gingerich P. D. and Pack A. (2016) Temperature and atmospheric CO_2 concentration estimates through the PETM using triple oxygen isotope analysis of mammalian bioapatite. *Proc. Natl. Acad. Sci. U. S. A.* **113**, 7739–7744.

Guo W. and Zhou C. (2019) Triple oxygen isotope fractionation in the DIC-H_2O-CO_2 system: A numerical framework and its implications. *Geochim. Cosmochim. Acta* **246**, 541–564.

Hayles J., Gao C., Cao X., Liu Y. and Bao H. (2018) Theoretical calibration of the triple oxygen isotope thermometer. *Geochim. Cosmochim. Acta* **235**, 237–245.

Heidenreich J. and Thiemens M. (1986) A non-mass-dependent oxygen isotope effect in the production of ozone from molecular oxygen: The role of molecular symmetry in isotope chemostry. *The Journal of Chemical Pyhsic*s **84**, 2129-2136.

Hofmann M. E. G., Horváth B. and Pack A. (2012) Triple oxygen isotope equilibrium fractionation between carbon dioxide and water. *Earth Planet. Sci. Lett.* **319**–**320**, 159–164.

Hulston J R and Thode H G (1965) Variations in the S^{33} S^{34} and S^{36} Contents of Meteorites and Their Relation to Chemical and Nuclear Effects. *J. Geophys. Res.* **70**, 3475–3484.

Koch P. L., Fisher D. C. and Dettman D. (1989) Oxygen isotope variation in the tusks of extinct proboscideans: a measure of season of death and seasonality. *Geology* **17**, 515–519.

Koch P. L., Heisinger J., Moss C., Carlson R. W., Fogel M. L. and Behrensmeyer A. K. (1995) Isotopic tracking of change in diet and habitat use in African elephants. *Science (80-.).* **267**, 1340–1343.

Kohn M. J. (1996) Predicting animal $\delta^{18}O$: Accounting for diet and physiological adaptation. *Geochim. Cosmochim. Acta* **60**, 4811–4829.

Kohn M. J., McKay M. P. and Knight J. L. (2005) Dining in the Pleistocene - Who's on the menu? *Geology* **33**, 649–652.

Kolodny Y., Luz B. and Navon O. (1983) Oxygen isotope variations in phosphate of biogenic apatites, I. Fish bone apatite-rechecking the rules of the game. *Earth Planet. Sci. Lett.* **64**, 398–404.

Levin N. E., Cerling T. E., Passey B. H., Harris J. M. and Ehleringer J. R. (2006) A stable isotope aridity index for terrestrial environments. *Proc. Natl. Acad. Sci. U. S. A.* **103**, 11201–11205.

Lehmann S. B., Levin N. E., Passey B. H., Hu H. T., Cerling T. E., Miller J. H., Arppe L. A.,

Beverly E.J., Hoppe K.A., Luyt J. and Sealy J. (2021) Triple oxygen isotope distribution in modern mammal teeth and potential geologic applications. *Geochim. Cosmochim. Acta*, in review.

Lodders K. (2003) Solar system abundances and condensation temperatures of the elements. *Astrophys. J.* **591**, 1220–1247.

Longinelli A. and Nuti S. (1973) Revised phosphate-water isotopic temperature scale. *Earth Planet. Sci. Lett.* **19**, 373–376.

Longinelli A. (1984) Oxygen isotopes in mammal bone phosphate: A new tool for paleohydrological and paleoclimatological research? *Geochim. Cosmochim. Acta* **48**, 385–390.

Lowenstein T. K. and Demicco R. V. (2006) Elevated eocene atmospheric CO_2 and its subsequent decline. *Science (80-.).* **313**, 1928.

Lüthi D., Le Floch M., Bereiter B., Blunier T., Barnola J. M., Siegenthaler U., Raynaud D., Jouzel J., Fischer H., Kawamura K. and Stocker T. F. (2008) High-resolution carbon dioxide concentration record 650,000-800,000 years before present. *Nature* **453**, 379–382.

Luz B., Kolodny Y. and Horowitz M. (1984) Fractionation of oxygen isotopes between mammalian bone-phosphate and environmental drinking water. *Geochim. Cosmochim. Acta* **48**, 1689–1693.

Luz B., Cormie A. B. and Schwarcz H. P. (1990) Oxygen isotope variations in phosphate of deer bones. *Geochim. Cosmochim. Acta* **54**, 1723–1728.

Luz B., Barkan E., Bender M.L., Thiemens M.H., Boering K.A. (1999) Triple-isotope composition of atmospheric oxyen as a tracer of biosphere productivity. *Nature* **400**, 547-550.

Luz B. and Barkan E. (2010) Variations of $^{17}O/^{16}O$ and $^{18}O/^{16}O$ in meteoric waters. *Geochim. Cosmochim. Acta* **74**, 6276–6286.

MacFadden B. J., Solounias N. and Cerling T. E. (1999) Ancient diets, ecology, and extinction of 5-million-year-old horses from Florida. *Science (80-.).* **283**, 824–827.

McKinney C. R., McCrea J. M., Epsein S., Allen H. A. and Urey H. . (1950) Improvements in Mass Spectrometers for the Measurement of Small Differences in. *Rev. Sci. instrucments* **21**, 724–730.

Meijer H. A. J. and Li W. J. (1998) The use of electrolysis for accurate $\delta^{17}O$ and $\delta^{18}O$ isotope measurements in water. *Isotopes Environ. Health Stud.* **34**, 349–369.

Nordt L., Atchley S. and Dworkin S. (2003) Terrestrial evidence for two greenhouse events in

the latest Cretaceous. *GSA Today* **13**, 4–9.

Pack A., Gehler A. and Süssenberger A. (2013) Exploring the usability of isotopically anomalous oxygen in bones and teeth as paleo-CO_2-barometer. *Geochim. Cosmochim. Acta* **102**, 306–317.

Pack A. and Herwartz D. (2014) The triple oxygen isotope composition of the Earth mantle and understanding $\delta^{17}O$ variations in terrestrial rocks and minerals. *Earth Planet. Sci. Lett.* **390**, 138–145.

Pack A., Tanaka R., Hering M., Sengupta S., Peters S. and Nakamura E. (2016) The oxygen isotope composition of San Carlos olivine on the VSMOW2-SLAP2 scale. *Rapid Commun. Mass Spectrom.* **30**, 1495–1504.

Pack A. (2021) Isotopic Traces of Atmospheric O_2 in Rocks, Minerals, and Melts. *Rev. Mineral. Geochemistry* **86**, 217–240.

Pagani M., Zachos J. C., Freeman K. H., Tipple B. and Bohaty S. (2005) Atmospheric science: Marked decline in atmospheric carbon dioxide concentrations during the Paleogene. *Science (80-.).* **309**, 600–603.

Passey, B.H., Hu, H., Ji, H., Montanari, S., Li, S., Henkes, G.A., Levin, N.E. (2014) Triple oxygen isotopes in biogenic and sedimentary carbonates. *Geochim. Cosmochim. Acta* **141**, 1.

Passey B. H. and Ji H. (2019) Triple oxygen isotope signatures of evaporation in lake waters and carbonates: A case study from the western United States. *Earth Planet. Sci. Lett*. **518**, 1–12.

Passey, B.H., Levin, N.E. (2021) Triple oxygen isotopes in carbonates, biological apatites, and continental paleoclimate reconstruction. *Rev. Mineral. Geochemistry* **86**, 429–626.

Pearson P. N., Foster G. L. and Wade B. S. (2009) Atmospheric carbon dioxide through the Eocene-Oligocene climate transition. *Nature* **461**, 1110–1113.

Petit J. R., Jouzel J., Raynaud D., Barnola J. M., Basile I., Bender M., Chappellaz J., Davis M., Delaygue G., Delmotte M., Kotlyakov V. M., Legrand M., Lipenkov V. Y., Loriu C., Pepin L., Ritz C., Saltzman E. and Stievenard M. (1999) Climate and atmospheric history of the past 420,000 years from the Vostok ice core, Antarctica. *Nature* **399**, 348–358.

Podlesak D. W., Torregrossa A. M., Ehleringer J. R., Dearing M. D., Passey B. H. and Cerling T. E. (2008) Turnover of oxygen and hydrogen isotopes in the body water, CO_2, hair, and enamel of a small mammal. *Geochim. Cosmochim. Acta* **72**, 19–35.

Retallack G. J. (2001) A 300-million-year record of atmospheric carbon dioxide from fossil

plant cuticles. *Nature* **411**, 287–290.

Retallack G. J. (2009) Refining a pedogenic-carbonate CO_2 paleobarometer to quantify a middle Miocene greenhouse spike. *Palaeogeogr. Palaeoclimatol. Palaeoecol.* **281**, 57–65.

Royer D. L., Berner R. A. and Beerling D. J. (2001) Phanerozoic atmospheric CO_2 change: Evaluating geochemical and paleobiological approaches. *Earth-Science Reviews*. **54**, 349-392.

Seki O., Foster G. L., Schmidt D. N., Mackensen A., Kawamura K. and Pancost R. D. (2010) Alkenone and boron-based Pliocene pCO_2 records. *Earth Planet. Sci. Lett.* **292**, 201–211.

Sharp Z. D. and Cerling T. E. (1998) Fossil isotope records of seasonal climate and ecology: Straight from the horse's mouth. *Geology* **26**, 219–222.

Sharp Z.D., Gibbons J.A., Maltsev O., Atudorei V., Pack A., Sengupta S., Shock E.L., Knauth L.P. (2016) A calibration of the triple oxygen isotope fractionation in the SiO_2 - H_2O system and applications to natural samples. *Geochim. Cosmochim. Acta* **186**, 105–119.

Sharp Z. D., Wostbrock J. A. G. and Pack A. (2018) Mass-dependent triple oxygen isotope variations in terrestrial materials. *Geochemical Perspect. Lett.* **7**, 27–31.

Shemesh A., Kolodny Y. and Luz B. (1983) Oxygen isotope variations in phosphate of biogenic apatites, II. Phosphorite rocks. *Earth Planet. Sci. Lett.* **64**, 405–416.

Smith R. Y., Greenwood D. R. and Basinger J. F. (2010) Estimating paleoatmospheric pCO_2 during the Early Eocene Climatic Optimum from stomatal frequency of Ginkgo, Okanagan Highlands, British Columbia, Canada. *Palaeogeogr. Palaeoclimatol. Palaeoecol* **293**, 120–131.

Sullivan C. H. and Krueger H. W. (1981) carbon isotope analysis of separate chemical phases in modern and fossil bone. *Nature* **292**, 333–334.

Tripati A. K., Roberts C. D. and Eagle R. A. (2009) Coupling of CO_2 and Ice sheet stability over major climate transitions of the last 20 million years. *Science (80-.)* **326**, 1394–1397.

Tütken T. and Vennemann T. (2009) Stable isotope ecology of Miocene large mammals from Sandelzhausen, southern Germany. *Palaontologische Zeitschrift* **83**, 207–226.

Veizer J., Godderis Y. and François L. M. (2000) Evidence for decoupling of atmospheric CO_2 and global climate during the Phanerozoic eon. *Nature* **408**, 698–701.

Werner A.G. 1788. Geschichte, Karakteristik, und kurze chemische Untersuchung des Apatits. *Bergmännisches Journal* **1**, p76.

Whiteman J. P., Sharp Z. D., Gerson A. R. and Newsome S. D. (2019) Relating $\Delta^{17}O$ Values of

Animal Body Water to Exogenous Water Inputs and Metabolism. *Bioscience* **69**, 658–668.

Wostbrock J. A. G., Cano, E. J. and Sharp, Z. D. (2020) An internally consistent triple oxygen isotope calibration of standards for silicates, carbonates and air relative to VSMOW2 and SLAP2. *Chem. Geol.* **533**, 119432.

Young E. D., Galy A. and Nagahara H. (2002) Kinetic and equilibrium mass-dependent isotope fractionation laws in nature and their geochemical and cosmochemical significance. *Geochim. Cosmochim. Acta* **66**, 1095–1104.

Young E. D., Yeung L. Y., Kohl I. E. (2014) On the $\Delta^{17}O$ budget of atmospheric O_2. *Geochim. Cosmochim. Acta* **135**, 102-125.

Yung Y.L., DeMore W.B., Pinto J.P. (1991) Isotopic exchange between carbon dioxide and ozone via O (^{1}D) in the stratosphere. *Geophysical Research Letters* **18**, 13-16.

Chapter 2 Isotopically anomalous metabolic oxygen in marine vertebrates as physiology and atmospheric proxy

Dingsu Feng, Thomas Tütken, Niklas Löffler, Gert Tröster & Andreas Pack, 2022. This work is in review in *Geochimica et Cosmochimica Acta*.

Abstract

Triple oxygen isotope data of tooth enamel (phosphate) from 16 modern marine vertebrates (sharks, mammals) from different marine habitats are presented. Marine mammal data show a clear signature of isotopically anomalous metabolic oxygen in their bioapatite. This is related to a low flux ratio of isotopically normal drinking and food water to anomalous metabolic oxygen. Traces of anomalous metabolic oxygen are also observed in shark bioapatite. Sharks and mammals have overlapping $^{18}O/^{16}O$ ratios, but distinct ^{17}O signatures. Our new data suggest that triple oxygen isotopes are a valuable new tracer to assess the physiology of extant and extinct marine vertebrates and may provide a new proxy for past atmospheric CO_2 mixing ratios and global primary biosphere production.

1   Introduction

It has been suggested by Bender et al. (1994) and shown by experiments of Luz et al. (1999) that molecular oxygen (O_2) in air carries a unique isotope anomaly in ^{17}O. This anomaly is inherited from mass-independent fractionation in the stratosphere (e.g., Luz et al., 1999; Young et al., 2014; Thiemens, 2006). The size of the ^{17}O anomaly of O_2 negatively correlates with the atmospheric CO_2 mixing ratio (pCO_2) and positively correlates with the global primary biosphere productivity (GPP; Bao et al., 2008; Young et al., 2014). The negative correlation between the ^{17}O anomaly of air O_2 and pCO_2 is due to the variable reservoir of stratospheric CO_2 with large positive ^{17}O anomaly, which is counterbalanced by O_2 with a negative anomaly. Photosynthetic O_2 has no ^{17}O anomaly. Primary O_2 production hence shifts air O_2 towards normal oxygen, i.e., O_2 without ^{17}O anomaly.

Respiration of anomalous air O_2 by heterotrophic organisms transfers the anomaly to their body water, from which the anomaly is then archived in their bioapatite (teeth, bones; Pack et al., 2013) or biocarbonate (e.g., egg shells; Passey et al., 2014). The size of the anomaly in the biominerals provides information about physiology (e.g., metabolic rates) or the bio- and atmosphere at the animal's lifetime (GPP, pCO_2).

Pack et al. (2013) showed that the triple oxygen isotope composition of bioapatite along with a mass balance model of land-living mammals can be used as proxy for the ^{17}O anomaly of ambient air O_2 and hence pCO$_2$ in combination with *GPP*. Gehler et al. (2016) used the triple isotope composition of fossil bioapatite to determine the pCO$_2$ across the Paleocene-Eocene thermal maximum. Passey et al. (2014) demonstrated that anomalous inhaled O_2 also leaves an imprint on the triple isotope composition of egg shell calcite (see also review by Passey and Levin, 2021). Whiteman et al. (2019) suggested that the triple oxygen isotope composition of mammal bioapatite provides direct insights into the metabolic rates.

Except of the data point in Pack et al. (2013, harbor porpoise), no triple oxygen isotope data have yet been published on marine vertebrates. For $^{18}O/^{16}O$, Longinelli and Nuti (1973) and Kolodny et al. (1983) assumed that marine vertebrate body water has the same composition than ambient seawater. Pack et al. (2013) extended this assumption to $^{17}O/^{16}O$ of a marine mammal. This implies that bioapatite of marine mammal does not carry an ^{17}O anomaly.

Here, we present an analytical protocol for high-precision triple oxygen isotope analyses along with the first triple isotope data of tooth enamel of a set of marine vertebrates (sharks, dolphins and whales). A mass balance model is developed to better understand the observed oxygen isotope compositions. The goal is to demonstrate whether traces of anomalous respired oxygen are also found in marine vertebrates and whether differences are observed between gill-breathing sharks and lung-breathing marine mammals. The overarching goal is to demonstrate if the triple oxygen isotopes of marine vertebrates is a new tool for physiological studies and if ^{17}O in fossil tooth enamel of marine vertebrates may be a new proxy archive for past pCO$_2$ and *GPP*.

2   Materials and Methods

2.1   Definitions

The oxygen isotope data are reported in the conventional $\delta^{17}O$ (Eq. 1) and $\delta^{18}O$ (Eq. 2) notation as:

$$\delta^{17}O^{sample}_{VSMOW2} = 1000 \times \left(\frac{(^{17}O/^{16}O)_{sample}}{(^{17}O/^{16}O)_{VSMOW2}} - 1 \right) \qquad \text{Eq. 1}$$

$$\delta^{18}O^{sample}_{VSMOW2} = 1000 \times \left(\frac{(^{18}O/^{16}O)_{sample}}{(^{18}O/^{16}O)_{VSMOW2}} - 1 \right) \qquad \text{Eq. 2}$$

The $\delta'^{17}O$ (Eq. 3) and $\delta'^{18}O$ (Eq. 4) notation were introduced as the linearized version of the

δ-notation (Hulston and Thode, 1965; Young et al., 2002):

$$\delta'^{17}O_{VSMOW2}^{sample} = 1000 \times \ln \left(\frac{\delta^{17}O_{VSMOW2}^{sample}}{1000} + 1 \right) \qquad \text{Eq. 3}$$

$$\delta'^{18}O_{VSMOW2}^{sample} = 1000 \times \ln \left(\frac{\delta^{18}O_{VSMOW2}^{sample}}{1000} + 1 \right) \qquad \text{Eq. 4}$$

We define triple oxygen isotope deviations from a given reference line ($\lambda_{RL} = 0.528$) in the

form

of the $\Delta'^{17}O$ value (Eq. 5).

$$\Delta'^{17}O_{0.528} = \delta'^{17}O_{VSMOW2}^{sample} - 0.528 \times \delta'^{18}O_{VSMOW2}^{sample} \qquad \text{Eq. 5}$$

The triple oxygen isotope fractionation between phases (A, B) is described by the

fractionation factor $\alpha_{A\text{-}B}$ and the triple oxygen isotope fractionation exponent $\theta_{A\text{-}B}$ (Young et

al., 2002) as:

$$\alpha_{A-B}^{17/16} = \left(\alpha_{A-B}^{18/16} \right)^{\theta_{A\text{-}B}} \qquad \text{Eq. 6}$$

Each equilibrium fractionation process has an individual θ value. The fractionation factors

$\alpha_{A-B}^{17/16}$ and $\alpha_{A-B}^{18/16}$ are the ratios of the $^{17}O/^{16}O$ and $^{18}O/^{16}O$, respectively, of coexisting phases

A and B presented as:

$$\alpha_{A-B}^{17/16} = \frac{\delta^{17/16}O_A + 1000}{\delta^{17/16}O_B + 1000} \qquad \text{Eq. 7}$$

$$\alpha_{A-B}^{18/16} = \frac{\delta^{18/16}O_A + 1000}{\delta^{18/16}O_B + 1000} \qquad \text{Eq. 8}$$

2.2 Marine vertebrae sampling

Tooth enameloid of 11 marine sharks and enamel of 5 marine mammals was separated from

dentine using a micro drill equipped with a diamond tip. The sampled taxa cover a wide body

mass range of approximately 1 up to 57,000 kg and body temperature estimates from 1 to

37 °C. A detailed overview of the individual taxa and the related physical characteristic are

presented in Table 1. The ambient ocean temperatures were derived from mean annual

seawater temperatures with an estimated uncertainty of ± 2 °C. For samples of taxa that lack

precise information of the catch area, we referred to the annual seawater temperatures of their

main habitats. The Greenland shark sample was analyzed for its clumped isotopic composition (i.e. biomineralization temperature) in a previous study (Löffler et al., 2019).

Table 1: List of all modern marine animals of which tooth enamel was separated and analyzed for their triple oxygen isotopic composition.

Sample	Name	Scientific name	Order	Sample origin	Sea temperature on average (°C)
M149	Blacktip shark	*Carcharhinus limbatus*	Carcharhiniformes	Blackpool Sea Life centre, UK	23 ± 2
M150	Sand tiger shark	*Carcharias taurus*	Lamniformes	Blackpool Sea Life centre, UK	23 ± 2
M151	Sandbar shark	*Carcharhinus plumbeus*	Carcharhiniformes	Blackpool Sea Life centre, UK	23 ± 2
M152	Sand tiger shark	*Carcharias taurus*	Lamniformes	–	15 ± 2
M153	Great white shark	*Carcharodon carcharias*	Lamniformes	South Africa	19.2 ± 2
M154	Greenland shark	*Somniosus microcephalus*	Squaliformes	Iceland	1 ± 2 (Löffler et al. 2019)
M155	Gulper shark	*Centrophorus granulosus*	Squaliformes	intermediate deep sea	12.9 ± 2
M111	Porbeagle	*Lamna nasus*	Lamniformes	–	7.5 ± 2
M156	Leafscale gulper shark	*Centrophorus squamosus*	Squaliformes	Madagascar	27 ± 2
M157	Shortfin mako shark	*Isurus oxyrinchus*	Lamniformes	Philippines	29 ± 2
M158	Sandbar shark	*Carcharhinus plumbeus*	Carcharhiniformes	Red Sea	22 ± 2
					Body temperature (°C)
M108	Oceanic dolphin	Delphinidae	Artiodactyla	–	37 ± 2
M107	Oceanic dolphin	Delphinidae	Artiodactyla	–	37 ± 2
M105	Harbour porpoise	*Phocoena phocoena*	Artiodactyla	North Sea	37 ± 2
M106	Beluga whale	*Delphinapterus leucas*	Artiodactyla	–	37 ± 2
M109	Sperm whale	*Physeter macrocephalus*	Artiodactyla	Westerhever, Germany	37 ± 2

– : unknown.

2.3   Bioapatite sample preparation

Powdered tooth enamel was treated with 2% NaClO for 45 minutes and 0.1% CH_3COOH for 15 minutes, then rinsed with distilled water 5 times for each step and dried overnight at 70 °C (Lee-Thorp et al., 2007). After the chemical pretreatment, samples were heated under oxygen-free atmosphere to 1000 °C for 30 minutes in a horizontal furnace to remove organic material as well as carbonate and hydroxyl groups. The furnace was flushed with 10% H_2 mixed with 90% N_2 using a gas flow controller set to 50 mL min^{-1}.

The organic and inorganic carbon content in bioapatite was analyzed using a gradual heating method on a LECO RC612 multi-phase carbon analyzer (LECO, St Joseph, MI, USA), calibrated against LECO carbon standards (1 wt.% C, 4.98 wt.% C, 12 wt.% C). After weighing in 20 mg of the bioapatite, the sample was introduced into the combustion chamber of the LECO carbon analyzer. With a preprogrammed temperature profile of 150 °C–900 °C, the samples were fed with an O_2+N_2 mixture (1:1 at 3.5 bar) reacted with a gas flow of 2.5 mL min^{-1}. Molecular oxygen is used for oxidation of organic matter and N_2 for transporting

the resulting CO_2 to the UV detector. The LECO carbon standards were measured between measuring each sample twice to calibrate the values. Results are illustrated in Figure 1.
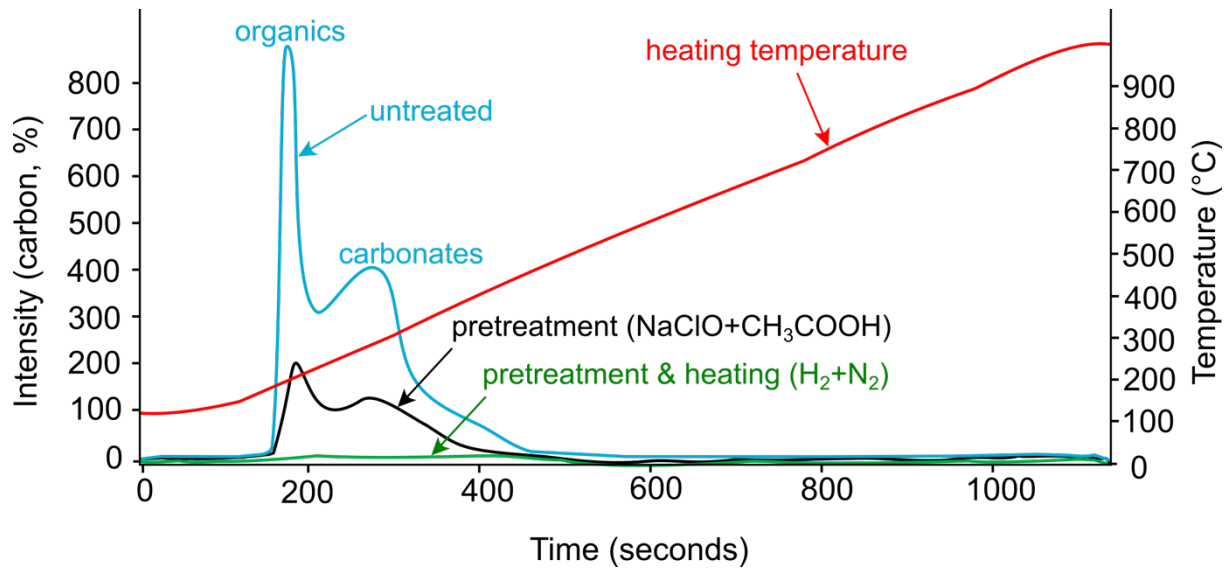
Figure 1: Plot of the CO_2 intensity of the African elephant tooth enamel powder AG-Lox (Gehler et al., 2012) combusted in the LECO carbon analyzer. AG-Lox tooth enamel: untreated (light blue curve), treated with NaClO and CH_3COOH (black curve), treated with NaClO and CH_3COOH, and then heated in the furnace flushed with $H_2 + N_2$ (green curve). The red curve outlines the heating profile.

After the chemical and successive thermal treatment carbon was efficiently removed from the bioapatite (Figure 1).

2.4   Oxygen isotope analyses

2.4.1   Laser fluorination

The triple isotope analyses were conducted by means of laser fluorination (LF) in combination with multi collector isotope ratio gas source mass spectrometry (IRMS) (Sharp, 1990). Details of this specific setup are provided in Pack et al. (2016). Approximately 2.5 mg preheated tooth enamel was loaded into a polished Ni metal sample holder with 14 pits, along with the AG-Lox and San Carlos Olivine reference materials. After installing the sample holder into the sample chamber and evacuating it for at least 12 hours, the tooth enamel was pre-melted with up to 5.5% laser power (SYNRAD 50 W CO_2 laser). After evacuation and heating of the sample chamber to 50 °C overnight, each sample was reacted in purified BrF_5 gas by means of heating with the CO_2 laser following the protocol described in Pack et al. (2016). The $\delta^{17}O$ and $\delta^{18}O$ values are reported relative to VSMOW2.

The accuracy and reproducibility of the O_2 extraction and cleaning protocols were verified by repeated analysis of San Carlos Olivine grains along with the bioapatite. The $\delta^{18}O$ of all samples were normalized to San Carlos Olivine with $\delta^{18}O = 5.3‰$ and $\Delta'^{17}O_{0.528} = -52$ ppm ($n = 59$; $\Delta'^{17}O$ of San Carlos olivine is average from Pack et al., 2016; Sharp et al., 2016; Wostbrock, 2020). To determine the external reproducibility, replicate analyses ($n = 72$) of the internal reference material AG-Lox were performed routinely. The data on apatite originating from the laser fluorination line are presented as $\delta^{17}O_{AP}$, $\delta^{18}O_{AP}$, and $\Delta'^{17}O_{AP}$, i.e., with the subscript "AP" for apatite, and are listed in Table 2. The average for AG-Lox is $\delta^{18}O_{AP} = 19.6‰$ and $\Delta'^{17}O_{AP} = -109$ ppm with an external reproducibility (1σ SD) in $\Delta'^{17}O_{AP}$ to 8 ppm.

Table 2: Triple oxygen isotope data ($\delta^{17}O_{AP}$, $\delta^{18}O_{AP}$, $\Delta'^{17}O_{AP}$) of inhouse standard AG-Lox (African elephant tooth enamel) from laser fluorination. These data were used to determine accuracy and the external reproducibility in $\delta^{18}O$ and $\Delta'^{17}O$. The external reproducibility in $\Delta'^{17}O$ is 8 ppm.

ID	$\delta^{18}O_{AP}$ (‰)	$\delta^{17}O_{AP}$ (‰)	$\Delta'^{17}O_{AP}$ (ppm)	ID	$\delta^{18}O_{AP}$ (‰)	$\delta^{17}O_{AP}$ (‰)	$\Delta'^{17}O_{AP}$ (ppm)
Slope			0.528	Slope			0.528
7315	18.863	9.804	-111	7580	19.062	9.917	-102
7314	18.806	9.781	-104	7573	19.619	10.208	-102
7312	18.770	9.764	-102	7678	19.067	9.912	-109
7310	18.746	9.751	-102	7673	18.918	9.827	-116
7309	18.680	9.713	-106	7698	18.987	9.862	-118
7333	18.711	9.715	-120	7688	18.352	9.524	-123
7331	18.734	9.734	-113	7719	19.698	10.240	-111
7335	18.880	9.808	-116	7750	20.211	10.506	-114
7327	19.452	10.115	-108	7736	19.789	10.289	-110
7328	19.625	10.203	-110	7731	18.901	9.817	-118
7323	18.368	9.535	-121	7815	20.161	10.480	-114
7354	19.872	10.331	-112	7810	19.824	10.308	-110
7376	20.354	10.589	-105	7917	19.697	10.241	-110
7397	20.081	10.434	-118	7912	19.539	10.154	-114
7392	20.029	10.406	-119	7941	18.505	9.603	-124
7422	19.489	10.144	-98	7934	19.599	10.189	-111
7421	19.474	10.133	-102	7963	19.927	10.374	-97
7418	19.441	10.123	-94	7958	19.992	10.397	-108
7416	19.243	10.005	-108	7987	19.961	10.383	-107
7413	19.038	9.890	-115	7983	19.687	10.228	-118
7411	19.015	9.871	-122	8011	20.858	10.853	-105
7458	19.305	10.057	-89	8005	20.247	10.535	-104
7452	19.311	10.061	-88	8028	20.527	10.678	-107
7448	19.070	9.915	-107	8024	20.237	10.527	-106
7469	19.263	10.039	-85	8113	20.374	10.596	-109
7465	17.944	9.333	-101	8109	19.847	10.315	-114
7490	20.234	10.529	-102	8133	20.492	10.666	-101
7485	19.915	10.353	-112	8129	19.555	10.157	-120
7481	19.615	10.198	-110	8153	20.761	10.799	-108
7512	20.370	10.602	-101	8144	19.670	10.219	-118
7507	20.319	10.566	-110	8192	19.573	10.169	-117
7536	20.379	10.600	-108	8489	19.162	9.959	-111
7531	19.971	10.380	-115	8481	19.409	10.087	-113
7526	19.236	10.000	-109	8507	19.954	10.376	-109
7557	20.516	10.687	-92	8522	20.218	10.514	-109
7549	19.179	9.971	-108	8517	19.104	9.922	-119
				average	19.55	10.17	-109
				1σ SD	0.63	0.33	8
				1σ SEM	0.07	0.04	1

2.4.2 Measurement of $\delta^{18}O$ of bioapatite phosphate oxygen by thermal combustion elemental analyzer (TC/EA)

The phosphate fraction of the chemically pretreated tooth enamel was precipitated as silver phosphate (Ag_3PO_4) to obtain an independent $\delta^{18}O$ value. This precipitation was performed according to the protocol of Dettman et al. (2001), and the modification by Tütken et al. (2006). Firstly, 2 mg of pretreated tooth enamel powder was transferred into a 2 mL

Eppendorf® tube (Eppendorf AG, Hamburg, Germany), placed on a vibrating table and digested in 0.8 mL hydrogen fluoride (HF, 2 M) for 12 h. The samples were centrifuged and the remaining supernatant solution that contains the dissolved phosphate was separated from calcium fluoride precipitates (CaF_2). The HF solution was transferred into a new tube and neutralized with ammonia solution (NH_4OH, 25%) using bromothymol blue as pH indicator. The Ag_3PO_4 precipitation was completed by adding 0.8 mL of silver nitrate ($AgNO_3$, 2 M). The Ag_3PO_4 crystals were centrifuged and the supernatant solution containing excess $AgNO_3$ was removed. The Ag_3PO_4 precipitate was then rinsed 5 times with Milli-Q water and dried overnight at 70 °C.

The Ag_3PO_4 aliquots of 300 μg were loaded into silver capsules and analyzed by means of high temperature reduction using a Thermo Finnigan TC/EA coupled via a ConFlo IV to a Micromass 100 GC-IRMS (Micromass UK Ltd, Manchester, United Kingdom) or a Delta V Plus at the stable isotope center in the Forest Faculty of University of Göttingen, Germany, according to the method of Vennemann et al. (2002). The $\delta^{18}O$ values from TC/EA are reported with the index "PO4" to distinguish them from $\delta^{18}O$ data from laser fluorination, which are marked by the index "AP".

For NBS120c, we obtained $\delta^{18}O_{PO4} = 21.6‰$ ($n = 25$, Table 3), which is, within uncertainty, indistinguishable from the $\delta^{18}O_{PO4} = 21.7‰$ reported by Lécuyer et al. (1993). This value has also been confirmed by other laboratories (e.g. Chenery et al., 2010). For Ag_3PO_4 from AG-Lox, we obtained an average $\delta^{18}O_{PO4} = 20.5‰$ ($n = 28$, Table 4).

Table 3: Silver phosphate (Ag$_3$PO$_4$) TC/EA oxygen isotope data of NBS120c as measured in different sessions. Given is the 1σ uncertainty.

ID	Session	δ^{18}O$_{PO4}$ (‰)
S1-08		21.28
S1-48		21.03
S1-70		21.09
S1-79		21.81
S1-80	session 1	21.72
S1-81		22.93
S1-82		22.74
S1-83		21.05
average		21.71 ± 0.76
S2-15		21.32
S2-27		22.69
S2-39	session 2	21.55
S2-51		21.91
S2-63		21.03
average		21.70 ± 0.64
S3-15		22.96
S3-27		21.30
S3-39	session 3	21.31
S3-51		21.09
S3-63		20.43
average		21.42 ± 0.93
S4-22		22.24
S4-34		22.54
S4-46		22.45
S4-58		21.59
S4-70	session 4	20.73
S4-82		20.91
S4-94		21.43
average		21.70 ± 0.73

Table 4: Silver phosphate (Ag$_3$PO$_4$) TC/EA oxygen isotope data of in-house standard AG-Lox (African elephant tooth enamel) as measured in different sessions. Given is the 1σ uncertainty.

ID	Session	$\delta^{18}O_{PO4}$ (‰)
S1-07		20.57
S1-62		21.04
S1-64		20.98
S1-69	session 1	20.69
S1-72		20.84
S1-75		21.06
average		20.86 ± 0.20
S2-16		20.76
S2-58	session 2	19.05
average		19.91 ± 0.16
S3-16		21.40
S3-58	session 3	19.44
S3-70		18.63
average		19.82 ± 1.26
S4-23		21.56
S4-31		21.02
S4-35		20.99
S4-42		21.71
S4-44		21.16
S4-47		21.70
S4-54		20.47
S4-56		20.93
S4-59	session 4	20.19
S4-66		19.88
S4-68		19.95
S4-71		19.74
S4-78		19.97
S4-79		19.58
S4-80		20.34
S4-83		21.16
S4-95		19.99
average		20.61 ± 0.63

2.4.3 Combining laser fluorination $\Delta'^{17}O_{AP}$ with $\delta^{18}O_{PO4}$ from TC/EA

The measurements of AG-Lox show that the $\delta^{18}O_{AP}$ from laser fluorination is typically ~1‰ lower than $\delta^{18}O$ of silver phosphate, $\delta^{18}O_{PO4}$, from TC/EA. Our TC/EA measurements of NBS-120c suggest that the $\delta^{18}O_{PO4}$ are accurate and that the laser fluorination is giving by 1‰ systematically too low $\delta^{18}O$ data. The reason for this small discrepancy is not clear. One possibility is that some heavy oxygen was lost during the laser fluorination, possibly in the

form of P-O-F compounds. Typical yields of ~ 90% for the bioapatite analyses may support this hypothesis. If 10% heavy oxygen was lost, the isotope composition of the lost, e.g., P-O-F compounds would be ~ 10‰ heavier than the apatite oxygen. While the TC/EA analyses only determine the composition of the P-bound oxygen, laser fluorination includes a little oxygen from the decarbonation of the carbonate group of the bioapatite. With ~ 5 wt.% carbonate, and 1/3 of the carbonate oxygen remaining from the decarbonation would leave ~ 2 wt.% carbonate-derived oxygen that mixes with ~ 98% of phosphate oxygen. To obtain the 1‰ shift in $\delta^{18}O$, it would require that the lost carbonate oxygen is 50‰ heavier than the remaining apatite oxygen. Although not being verified, such large fractionation is not regarded as probable.

As TC/EA of Ag_3PO_4 selectively reports on the phosphate oxygen, we use the TC/EA $\delta^{18}O$ data and combine them with the $\Delta'^{17}O$ from the laser fluorination. We assume that the observed 1‰ fractionation associated with laser fluorination is a mass-dependent process. In course of this study, we have not determined the associated θ with the 1‰ instrumental fractionation during laser fluorination. We adopt a $\theta = 0.528$, which is close to the values of a wide range of mass-dependent processes (Pack and Herwartz, 2014). Choosing a different θ here would change the results only by a few ppm and would not have any effect on the main outcome of our study. This implies that the numerical values for $\Delta'^{17}O$ did not change when TC/EA and laser fluorination data are being combined.

3   Results

3.1   Marine vertebrates

The sharks, dolphins and whales' oxygen isotope data are listed in Table 5 and illustrated in Figure 2. For sharks, the $\delta^{18}O_{PO4}$ ranges from 19.3 to 24.3‰ and the $\Delta'^{17}O$ ranges from -141 to -90 ppm. For dolphins and whales, the $\delta^{18}O_{PO4}$ ranges from 15.2 to 18.6‰ and the $\Delta'^{17}O$ ranges from -142 to -117 ppm (Figure 2).

Table 5: List of oxygen isotope data (individual measurements and means) of tooth enamel(oid) of marine vertebrates. The $\delta^{18}O_{AP}$ and $\Delta'^{17}O_{AP}$ values were obtained by laser fluorination and $\delta^{18}O_{PO4}$ by using a temperature conversion elemental analyzer (TC/EA). The uncertainty in $\Delta'^{17}O$ is 0.008‰ (1σ SD). The ID refers to the internal measurement identification number.

ID	$\delta^{18}O_{AP}$ (‰)	$\Delta'^{17}O_{AP}$ (ppm)	$\delta^{18}O_{PO4}$ (‰)
Slope		0.528	
Blacktip shark			
7389	18.183	-112	
7484	18.146	-108	
7483	19.571	-110	
7556	18.503	-78	
average	18.601	-102	20.4
Sand tiger shark			
7390	19.874	-127	
7488	18.830	-129	
average	19.352	-128	21.0
Sandbar shark			
7367	18.208	-124	
7482	19.900	-113	
7528	19.498	-98	
average	19.202	-112	20.9
Sand tiger shark			
7353	19.248	-99	
7347	18.443	-119	
7537	19.865	-88	
average	19.185	-102	21.6
Great white shark			
7399	19.586	-79	
7395	19.083	-94	
7489	19.348	-97	
7504	19.039	-120	
average	19.264	-97	21.8
Greenland shark			
7378	22.085	-136	
7529	21.779	-129	
7570	21.214	-159	
average	21.693	-141	24.3
Gulper shark			
7510	22.277	-107	
7451	21.669	-126	
average	21.973	-117	24.2
Porbeagle			
7355	20.614	-95	
7348	19.263	-98	
7473	22.594	-100	
7538	20.338	-98	
average	20.703	-97	22.2

ID	$\delta^{18}O_{AP}$ (‰)	$\Delta'^{17}O_{AP}$ (ppm)	$\delta^{18}O_{PO4}$ (‰)
Slope		0.528	
Leafscale gulper shark			
7398	18.289	-78	
7492	18.568	-94	
7552	18.919	-112	
average	18.592	-95	19.3
Shortfin mako shark			
7505	18.541	-109	
7555	19.481	-68	
7449	20.491	-94	
average	19.504	-90	20.2
Sandbar shark			
7506	21.108	-100	
7559	21.489	-80	
7450	21.050	-105	
average	21.216	-95	23.6
Oceanic dolphin			
7352	15.048	-112	
7346	15.621	-155	
7468	18.496	-115	
7534	14.473	-124	
average	15.910	-126	17.3
Oceanic dolphin			
7373	13.451	-128	
7467	18.655	-92	
7530	13.781	-131	
average	15.296	-117	17.6
Harbour porpoise			
7369	15.582	-140	
7514	14.558	-154	
7551	15.825	-121	
average	15.321	-138	16.4
Beluga whale			
7372	12.416	-129	
7466	15.834	-121	
7558	11.452	-157	
7571	13.619	-160	
average	13.330	-142	15.2
Sperm whale			
7377	16.918	-146	
7535	17.460	-125	
average	17.189	-135	18.6

Figure 2: Plot of $\Delta'^{17}O_{AP}$ vs. $\delta^{18}O_{PO4}$ of tooth enamel of modern sharks (light blue symbols) and marine mammals (orange symbols): Light blue circle: Blacktip shark; light blue triangle-down: Sand tiger shark; light blue triangle-up: Sandbar shark; light blue triangle-right: Great white shark; light blue triangle-left: Greenland shark; light blue square: Gulper shark; light blue plus: Porbeagle; light blue diamond: Leafscale gulper shark; light blue thin-diamond: Shortfin mako shark; orange squares: Delphinidae; orange diamond: *Phocoena phocoena*, left-pointing triangle: *Delphinapterus leucas*; right-pointing triangle: *Physeter macrocephalus*.

4   Discussion

For sharks, $\Delta'^{17}O_{PO4}$ data plot on or slightly below the theoretical prediction from the seawater-apatite equilibrium (Hayles et al., 2018; Figure 2). If the body water would be compositionally identical to ambient seawater, as assumed by Longinelli and Nuti (1973), Kolodny et al. (1983) and Pucéat et al. (2010) for bony fish, bioapatite is expected to plot on that equilibrium curve. Instead, our data suggest that even for sharks, traces of anomalous metabolic oxygen are preserved in the isotope composition of their tooth enameloid. This implies that shark tooth enameloid is, strictly speaking, unsuitable to determine $\alpha^{18/16}_{\text{apatite−water}}$ and $\theta_{\text{apatite-water}}$. The observation of the upper limit of the shark $\delta^{18}O$-$\Delta'^{17}O$ data coinciding with the theoretical equilibrium curve is taken as support for the validity of the calculations

by Hayles et al. (2018) for the inorganic triple oxygen isotope fractionation between seawater and bioapatite.

Chang and Blake (2015) experimentally demonstrated that there is a 0.5–0.7‰ O-isotope fractionation between dissolved PO_4 and biogenic apatite. If $\alpha^{18/16}_{\text{apatite}-\text{water}}$ from Pucéat et al. (2010) or Chang and Blake (2015) were combined with $\theta_{\text{apatite-water}}$ from Hayles et al. (2018), our data would still plot below the equilibrium line. Negative departures from this relation are explained by contribution of an isotopically anomalous component from respired dissolved O_2. Because this study is dealing with triple oxygen isotope fractionation between apatite and water, for the sake of consistency, we prefer to take the theoretical oxygen isotope fractionation between apatite and water of Hayles et al. (2018) for both $\alpha^{18/16}_{\text{apatite}-\text{water}}$ and $\alpha^{17/16}_{\text{apatite}-\text{water}}$.

The $\Delta'^{17}O$ of bioapatite of dolphins and whales is significantly lower than suggested by oxygen isotope equilibrium fractionation with seawater. This is related to the significant portion of metabolic oxygen in their body water. The negative deviation of the $\Delta'^{17}O$ of bioapatite of dolphins and whales from the seawater equilibrium curve (Hayles et al., 2018) further demonstrates that $\theta_{\text{apatite-water}}$ should not be derived from marine mammal and explains the much lower $\theta_{\text{apatite-water}}$ of Pack et al. (2013).

Our data show that traces of anomalous metabolic oxygen can not only be observed in terrestrial vertebrates (Levin et al., 2006; Podlesak et al., 2008; Pack et al., 2013; Passey et al., 2014; Blumenthal et al., 2017; Whiteman et al., 2019; Passey and Levin, 2021), but also in marine sharks, dolphins and whales. Whereas the signal in shark teeth is relatively small, a strong metabolic signal is observed in the studied marine mammals with both groups filling separate fields in the $\Delta'^{17}O$ vs. $\delta^{18}O$ space (Figure 2).

This first observation of metabolic oxygen in tooth enamel is in line with suggestions that sharks, but especially the studied cetaceans drink very little and largely survive on water in food and metabolic water. Rash and Lillywhite (2019) reviewed the drinking behavior of marine vertebrates and emphasize that relatively little is known, mainly due to logistic difficulties. Our data show that triple oxygen isotopes of bioapatite can help to better understand the physiology of marine mammal.

4.1 Mass balance model

4.1.1 Basic equations

In order to quantitatively understand the experimental data, we developed oxygen mass balance models for the studied sharks and marine mammals (dolphins, whales). The fluxes of these mass balance models (F_i^{in} and F_j^{out}) are reported in mol O day^{-1}. Both models are illustrated in Figure 3 with the related parameters being listed in Table 6.
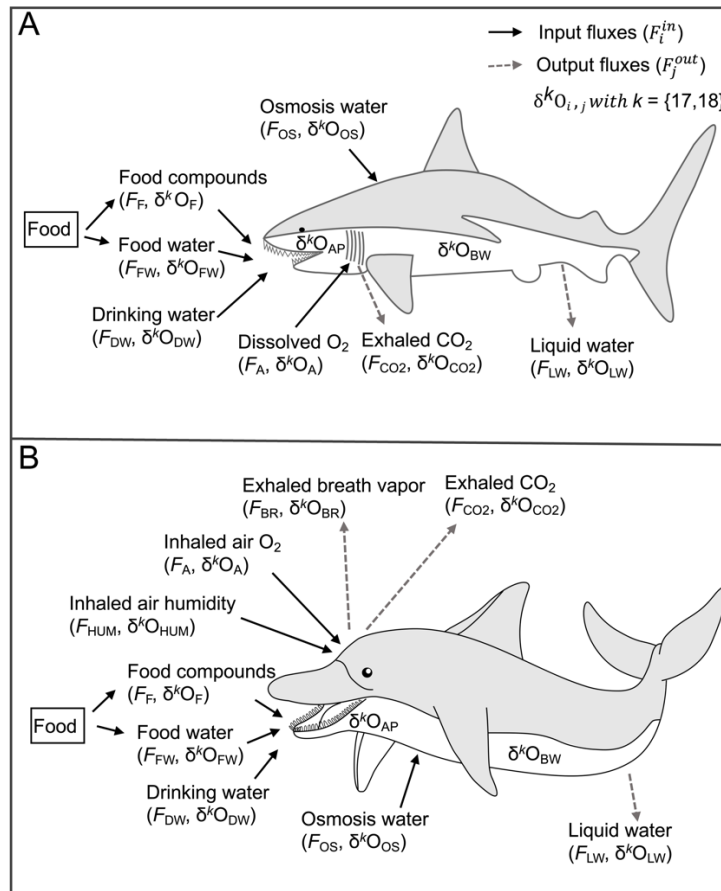
Figure 3: Illustration of the mass balance models for A) sharks and B) dolphins and whales. F_{OS}: Osmosis water, F_F: Oxygen in dry food, F_{FW}: Food water, F_{DW}: Drinking water, F_A: Inhaled air O_2 or dissolved O_2, F_{HUM}: Inhaled vapor from air humidity, F_{CO2}: Exhaled CO_2, F_{LW}: Liquid water, F_{BR}: Exhaled breath vapor.

The principal oxygen influxes (F_i^{in}) in both mass balance models are respired (lungs or gills) anomalous molecular oxygen (F_A), drinking water (F_{DW}), water from osmosis (F_{OS}), water from food (F_{FW}), and oxygen-bearing inorganic food compounds (F_F). Common outfluxes (F_j^{out}) are exhaled CO_2 (F_{CO2}), liquid water in urine, feces and sweat (F_{LW}).

For marine mammals, the additional in- and outfluxes of the inhaled air humidity (F_{HUM}) and exhaled breath vapor (F_{BR}) are considered.

Table 6: List of model parameters used in the mass balance model and Monte Carlo error calculation.

Parameter	Description	Value	References
λ_{RL}	slope of reference line	0.528	
Rq	Respiratory quotient	sharks (0.85 ± 0.1), sea mammals (0.75 ± 0.1)	Irving et al. (1941); Ridgway and Patton (1971)
$\delta^{18}O_{DW}$	$^{18}O/^{16}O$ of seawater	$0.4 \pm 0.7‰$	Luz and Barkan (2010)
$\Delta'^{17}O_{DW}$	$^{17}O/^{16}O$ of seawater	$-0.004 \pm 0.005‰$	Luz and Barkan (2010)
$\delta^{18}O_{Air}$	$^{18}O/^{16}O$ of air	$23.9 \pm 0.3‰$	average from Pack (2021)
$\Delta'^{17}O_{Air}$	Isotope anomaly of air	-432 ± 15 ppm	average from Pack (2021)
$\delta^{18}O_A$	respired air O_2 ($^{18}O/^{16}O$) for sea mammals	$22.8 \pm 2‰$.	Epstein and Zeiri (1988)
$\Delta'^{17}O_A$	respired air O_2 ($\Delta'^{17}O_A$) for sea mammals	$-0.421 \pm 0.019‰$	Epstein and Zeiri (1988)
θ_{A-Air}	fractionnation exponent between respired and air O_2	0.5179 ± 0.0006	Luz and Barkan (2005)
$\delta^{18}O_F$	$^{18}O/^{16}O$ of oxygen in food	$19.2 \pm 1.3‰$	Chesson et al. (2011)
$\delta^{17}O_F$	$^{17}O/^{16}O$ of oxygen in food	$10.1 \pm 0.7‰$	Chesson et al. (2011)
$\delta^{18}O_{HUM}$	$^{18}O/^{16}O$ of inhaled air humidity	$-15.5 \pm 2.7‰$	Uemura et al. (2010)
$\delta^{17}O_{HUM}$	$^{17}O/^{16}O$ of inhaled air humidity	$-8.2 \pm 1.5‰$	Uemura et al. (2010)
α_{CO2-BW}	fractionation factor between CO_2 and body water	ranges from temperature for sharks (0 - 37 °C), sea mammals (1.0396 ± 0.0001)	Brenninkmeijer et al. (1983); Bradley (2017); Beck et al. (2005); Guo and Zhou (2019)
θ_{CO2-BW}	fractionation exponent for the CO_2 - water equilibrium	sea mammals (0.5246 at 37 °C)	Cao and Liu (2011); Guo and Zhou (2019)
α_{LW-BW}	fractionation factor between liquid water and body water	1	Bryant and Froelich (1995)
α_{BR-BW}	fractionation factor between breath vapor and body water	0.9916 ± 0.002	Horita and Wesolowski (1994); Pack et al. (2013)
θ_{BR-BW}	fractionation exponent between water and vapor	0.529 ± 0.001	Barkan and Luz (2005)
$\alpha_{apatite-water}$	fractionation factor between apatite - water	ranges from temperature (0 - 37 °C)	Hayles et al. (2018)

The body water oxygen isotopic compositions $\delta^{18}O_{BW}$ and $\delta^{17}O_{BW}$ are calculated according to Eq. 9, 10, and 11.

$$\sum F_i^{in} + \sum F_j^{out} = 0 \qquad \text{Eq. 9}$$

$$\frac{\sum \left(F_i^{in} \times \delta^{17}O_i^{in}\right) + \sum \left(F_j^{out} \times \delta^{17}O_j^{out}\right)}{\sum F_i^{in}} = 0 \qquad \text{Eq. 10}$$

$$\frac{\sum \left(F_i^{in} \times \delta^{18}O_i^{in}\right) + \sum \left(F_j^{out} \times \delta^{18}O_j^{out}\right)}{\sum F_i^{in}} = 0 \qquad \text{Eq. 11}$$

From Eq. 9, 10, and 11 we could calculate $\delta^{18}O_{LW}$ and $\delta^{17}O_{LW}$. F_{LW} is not fractionated relative to body water (Lifson et al., 1966; Schoeller et al., 1986; Wong et al., 1988; Bryant and Froelich, 1995). Hence, $\delta^{18}O_{LW} = \delta^{18}O_{BW}$ and $\delta^{17}O_{LW} = \delta^{17}O_{BW}$. The $\Delta'^{17}O_{BW}$ is calculated from $\delta^{17}O$ and $\delta^{18}O$ (see Methods, Eq. 5).

Specific $\delta^{17}O$ and $\delta^{18}O$ are assigned to the individual in- and outfluxes. For F_i^{out}, oxygen isotope fractionation between outflux and body water ($\delta^{17}O_{BW}$, $\delta^{18}O_{BW}$) is considered. The

$\delta^{18}O$ of the outflux is given by the fractionation factor α with $\delta^{18}O_j = \alpha_{j\text{-BW}} \times (\delta^{18}O_{BW} + 1000)$ $- 1000$ and $\delta^{17}O_j = \alpha_{j\text{-BW}}{}^\theta \times (\delta^{17}O_{BW} + 1000) - 1000$.

4.1.2 Fluxes (F_i^{in}, F_j^{out})

4.1.2.1 Inhaled oxygen (F_A)

The flux of inhaled molecular O_2 (F_A) is closely related to the metabolic rate, which is the energy consumption of the respective animal. Generally, the metabolic rate scales approximately with body mass M_b proportional to $0.27M_b^{0.86}$ (Sims, 2000). In the case of sharks, absorption of dissolved molecular O_2 from the ambient seawater is achieved by their gills while marine mammals inhale molecular O_2 from air with their lungs.

For the blacktip shark (1.03 kg $\leq M_b \leq$ 1.47 kg), F_A ranges from 0.43 to 0.98 mol O day^{-1} (Lear et al., 2017). For the other sharks, F_A are listed in Table 7.

Table 7: List of in- and outfluxes (mol O day^{-1}) for the marine vertebrate oxygen mass balance model (model parameter details given in Table 6).

Name	Body mass (kg)	F_A	F_{OS}	Daily ration (DR) (%)	F_{FW}	F_F	F_{DW}	F_{HUM}	F_{CO2}	F_{BR}	F_{LW}
Blacktip shark	1.03…1.47[a]	0.43…0.98[a]	0.01…0.07	1…5[b]	0.34…3.67	0.04…0.43	0	–	–1.06…–0.23	–	–4.10…–0.59
Sand tiger shark	90…150[b]	7…12[c]	0.1…0.4	0.27[d]	8…20	1…2	0	–	–13…–5	–	–22…–11
Sandbar shark	1.90[e]	0.23…0.91[f]	0.01…0.03	0.93…1.32[e]	0.59…1.25	0.08…0.15	0	–	–0.17…–1.00	–	–1.34…–0.73
Great white shark	428 ± 61[g]	23…73[h]	1…10	1.5…1.8[g]	137…504	14…65	0	–	–81…–15	–	–571…–160
Greenland shark	33…126[i]	0.3…3.8[i]	0.1…1.3	0.1…1[b]	1…63	1…7	0	–	–4…–0.2	–	–71…–2
Gulper shark	4…6[b]	0.48…0.78[c]	0.01…0.30	1…5[b]	1…15	0.15…1.75	0	–	–0.86…–0.31	–	–17…–1
Porbeagle	10…150[j]	1…17[c]	1…7	1…5[b]	3…375	1…44	0	–	–19…–1	–	–424…–5
Leafscale gulper shark	3.7…8.5[k]	0.4…1.1[c]	0.1…0.4	1…5[b]	1…21	0.2…2.5	0	–	–1.2…–0.3	–	–24…–1.5
Shortfin mako shark	4.4…9.5[l]	1…8[l]	0.2…0.5	4.4…4.9[m]	16…23	2.0…2.7	0	–	–8…–1	–	–26…–18
Oceanic dolphin	90[n]	67…340[o]	1…5	2.8…5.0[n]	84…225	11…26	0…60	2…10	–357…–44	–37…–7	–271…–113
Harbour porpoise	32…50[p]	36…130[q]	1…4	3…8[r]	32…200	4…23	0…22	1…4	–103…–41	–14…–4	–267…–29
Beluga whale	1400[s]	336…476[t]	6…17	1.2[s]	560…839	72…98	0…95	10…14	–357…–252	–37…–52	–1130…–694
Sperm whale	35000…57000	8400…19380[t]	233…2280	2…4[u]	23316…113918	2988…13309	0…12920	252…581	–14535…–6300	–2132…–924	–145721…–27965

a: Lear et al. (2017), b: Estimated, c: Sims (2000), d: Schmid et al. (1990), e: Medved et al. (1988), f: Dowd et al. (2006), g: Semmens et al. (2013), h: Watanabe et al. (2019), i: Ste-Marie et al. (2020), j: Aasen (1961), k: Kjerstad et al. (2003), l: Sepulveda et al. (2007), m: Wood et al. (2009), n: Meynier et al. (2008), o: Williams et al. (1993; 2001), p: Santos et al. (2005), q: Rojano-Donãte et al. (2018), r: Yasui and Gaskin (1986); Santos et al. (2005), s: Kastelein et al. (1994), t: Telfer et al. (1970); Rosen and Trites (2013), u: Clarke. (1977); Kawakami (1980); Kjeld (2003)

For the dolphins, the oxygen consumption ($M_b = 90$ kg; Meynier et al., 2008) is $67 \leq F_A \leq 340$ mol O day^{-1} (Williams et al., 1993, 2001). For other marine mammals, F_A are listed in Table 7.

4.1.2.2 Drinking water (F_{DW})

The flux of drinking water (F_{DW}) in form of salty seawater is close to zero for both sharks and marine mammals (Fetcher and Fetcher, 1942; Ortiz, 2001; Kjeld, 2003; Rash and Lillywhite, 2019). Studies suggested that sharks do not drink any seawater (Fetcher and Fetcher, 1942; Ortiz, 2001; Kjeld, 2003; Rash and Lillywhite, 2019). However, accidental ingestion of some seawater can not be excluded.

Hui (1981) and Telfer et al. (1970) demonstrated that, common dolphins ingest 39 mol O day^{-1} with $M_b = 59$ kg (Hui, 1981), which is ~22% of the total water influxes. Hui (1981) demonstrated that metabolic water is sufficient to maintain the water balance without drinking, i.e., that dolphins and pilot whales, along with some desert animals such as kangaroo rats, are among the most water-efficient mammals. Therefore, the quantification of seawater drinking in dolphins (Telfer et al., 1970; Hui, 1981) poses the question as to why they drink. Data of Rash and Lillywhite (2019) suggest that most marine mammals do not drink seawater. For marine mammals in this study, we assume that F_{DW} ranges from zero up to 20% of the total water fluxes.

4.1.1.3 Osmosis water (F_{OS})

Sharks absorb water by osmosis (F_{OS}), mainly through the gill tissues into the isotonic to hypertonic body water (Carrier et al., 2012). We estimated osmosis values for sharks up to 2% of the total water influxes based on Kjeld (2003).

For F_{OS} of marine mammals, Kjeld (2003) estimated the contribution of ingested seawater through osmosis to 1–2% of the total water influxes for large baleen whales. Based on Kjeld (2003), we adopt this estimation of osmosis values up to 2% of the total water influxes for marine mammals.

4.1.1.4 Water from food (F_{FW}) and oxygen-bearing inorganic food compounds (F_F)

The average daily food consumption is referred to as daily ration (DR) and defined by C/F/W with C being the daily energy consumption in J day^{-1}, F being the energy content of the ingested food (J kg^{-1} wet weight), and W being body mass of the specimen in kg. The

average daily food consumption (F_{food}) of marine vertebrates is calculated from DR according to Eq. 12. Following Murray and Burt (1983), fish flesh is mainly composed of water (f_{water}), which accounts for 60–90 wt.% of fresh white fish fillet. The amount of protein in fish muscle ($f_{protein}$) is usually between 15 and 20 wt.% and the fat (f_{fat}) amounts approximately 1–13 wt.%. Carbohydrates ($f_{carbohydrate}$) contribute with less than 1 wt.%. The oxygen in other food constituents (e.g., vitamins) is negligible (Murray and Burt, 1983) and therefore not considered in the mass balance model. According to the respective mole fractions, the relative contributions of the main oxygen sources are 36 mol% proteins (CH_3CHNH_2COOH), 12 mol% fat ($CH_3(CH_2)_{14}COOH$), and 53 mol% carbohydrate ($C_6H_{12}O_6$).

The amount of water in ingested food (F_{FW}) is calculated from F_{food} and f_{water} according to Eq. 13. The amount of oxygen-bearing in organic food compounds (F_F) is calculated from F_{food}, the aforementioned oxygen sources, and their respective oxygen mole fractions according to Eq. 14.

$$F_{food} = Mb \times DR \qquad \text{Eq. 12}$$

$$F_{FW} = F_{food} \times f_{water} \times 89\% \qquad \text{Eq. 13}$$

$$F_F = F_{food} \left(f_{protein} \times 36\% + f_{fat} \times 12\% + f_{carbohydrate} \times 53\% \right) \qquad \text{Eq. 14}$$

For the blacktip shark, the daily ration is estimated from 1 to 5%. The water in ingested food is $0.34 \leq F_{FW} \leq 3.67$ mol O day^{-1} and oxygen-bearing in organic food compounds is $0.04 \leq F_F \leq 0.43$ mol O day^{-1}.

For oceanic dolphin, the daily ration is $2.8\% \leq DR \leq 5.0\%$ (Meynier et al., 2008). The water in ingested food (F_{FW}) is $84 \leq F_{FW} \leq 225$ mol O day^{-1} and oxygen-bearing in organic food compounds (F_F) is $11 \leq F_F \leq 26$ mol O day^{-1}.

The DR, F_{FW} and F_F of all marine vertebrates are listed in Table 7.

4.1.1.5   Inhaled vapor from air humidity (F_{HUM}) for marine mammals

For marine mammals, the flux F_{HUM} (Eq. 16) is the inhaled air humidity from the atmosphere, which depends on the total volume of inhaled air V_{air} (Eq. 15) per day, temperature, and humidity (R_h). V_{air} can be estimated on basis of F_A. The factor X is the efficiency of the

oxygen utilization fraction in the lungs of marine mammal with X = 0.9 ± 0.1 (see section 4.2.4.2). The total flux of air (V_{air}) through the lung is:

$$V_{air} = 0.5 \, F_A \, 22.4 \text{ L mol}^{-1} \times X^{-1} \times 0.21^{-1} \qquad \text{Eq. 15}$$

The factor 0.21^{-1} relates to the atmospheric O_2 mixing ratio. The saturation vapor content (V_C) is given by $V_C = 5.018 + 0.32321 \, t + 8.1847 \times 10^{-3} \, t^2 + 3.1243 \times 10^{-4} \, t^3$ g m^{-3} (40 °C $\geq t \geq 0$ °C) (Nave, 2000). We take $R_h = 0.7$ as average humidity and t = 16 °C as average temperature (Matt, 2000). The resultant flux F_{HUM} of inhaled vapor from humidity into the lungs is:

$$F_{HUM} = R_h \times V_C \, /1000 \text{ g L}^{-1} \times V_{air} \, / \, (18.02 \text{ g mol}^{-1})$$

$$= 0.03 \, F_A \qquad \text{Eq. 16}$$

4.1.1.8 Exhaled CO_2 (F_{CO2})

The flux F_{CO2} is related to F_A and the respiratory quotient (Rq), whereas Rq is the molar ratio of respired O_2 to exhaled CO_2 (Eq. 17).

$$F_{CO2} = -Rq \times F_A \qquad \text{Eq. 17}$$

The Rq of sharks is 0.85 ± 0.2 and 0.75 ± 0.2 (Irving et al., 1941; Ridgway and Patton, 1971) for marine mammals.

4.1.1.7 Exhaled breath vapor (F_{BR}) for marine mammals

For the marine mammals, the flux F_{BR} is the vapor in exhaled breath and thus directly related to the volume V_{air} (Eq. 15) of inhaled air per day. The exhaled breath is water-saturated at 37 °C and contains 44.0 g m^{-3} water ($R_h = 1$, t = 37 °C, Matt, 2000).

$$F_{BR} = F_{HUM} - 44.0 \, /1000 \text{ g L}^{-1} \times V_{air} \, / \, (18.02 \text{ g mol}^{-1})$$

$$= -0.11 \, F_A \qquad \text{Eq. 18}$$

4.1.1.8 Liquid water (F_{LW})

The liquid water outflux (F_{LW}) in excrements and urine (Lifson and McClintock, 1966; Schoeller et al., 1986; Wong et al., 1988) of sharks is calculated on basis of mass-

conservation to $F_{LW} = -F_A - F_{DW} - F_{OS} - F_{FW} - F_F - F_{CO2}$. F_{LW} of marine mammals is defined by $F_{LW} = -F_A - F_{DW} - F_{OS} - F_{FW} - F_F - F_{HUM} - F_{CO2} - F_{BR}$.

The resulting oxygen mass balance model is exemplified in Figure 4 for an oceanic dolphin. The four main fluxes for marine mammals are: F_A, F_{FW}, F_{LW}, and F_{CO2}.
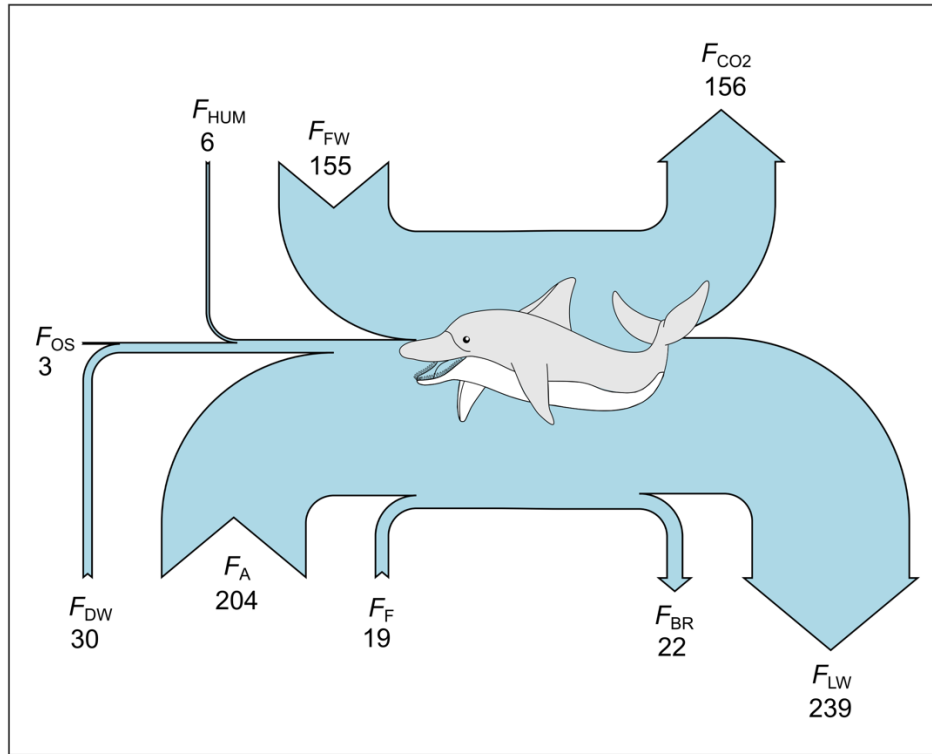
Figure 4: Illustration of the average input and output fluxes for a 90 kg dolphin in a steady state. All values are on average and reported in mol O day^{-1}. F_{FW}: Food water, F_{HUM}: Inhaled air humidity, F_{OS}: Osmosis water, F_{DW}: Drinking water, F_A: Inhaled air O_2, F_F: Food compounds, F_{LW}: Liquid water, F_{BR}: Exhaled breath vapor, F_{CO2}: Exhaled CO_2.

4.1.3 Isotope compositions

4.1.3.1 Inhaled oxygen

Sharks inhale dissolved O_2. The $\delta^{18}O$ of dissolved O_2 in seawater ranges from 22 to 42‰ (Yeung et al., 2020). The corresponding $\Delta'^{17}O$ of dissolved O_2 in seawater varies between −0.531 and −0.260‰ (Yeung et al., 2020). For the mass balance, we used the following ($\delta^{18}O$, $\Delta'^{17}O$)-pairs to confine the isotope composition of dissolved O_2: (23.43‰, -0.309‰), (24.26‰, -0.414‰), and (42.22‰, -0.531‰) (see red-points and red dashed area in Figure 5).

Sharks' gills absorb approximately X = 53.4 ± 4.2% of the dissolved O_2 (Piiper and Schumann, 1967; Wegner et al., 2012). We use the relationship between X and isotope fractionation ($\delta^{18}O$) during respiration from Epstein and Zeiri (1988) to approximate the isotope composition of absorbed O_2. For $\delta^{17}O$, we use the respiratory $\theta = 0.5179 \pm 0.0006$ of Luz and Barkan (2005). The range of isotope compositions for F_A for sharks is outlined in Figure 4 (gray shaded area).

Marine mammals breathe air O_2. The composition of modern air O_2 is $\delta^{18}O = 23.9 \pm 0.3‰$ and $\Delta'^{17}O = -0.432 \pm 0.015‰$ (Pack, 2021). The $\delta^{18}O$ of F_A is lower than ambient O_2 due to preferential diffusive intake of isotopically light O_2 (Epstein and Zeiri, 1988). Because of morphological and physiological adaptation to their environment, marine mammals have a high oxygen efficiency of $X = 0.9$ (Walker, 2007; Wartzok, 2009). According to the relationship between X and isotope composition of exhaled air from Epstein and Zeiri (1988), $\delta^{18}O_A$ is approximated to $22.8 \pm 0.1‰$. The fractionation in $\delta^{17}O$ is calculated using the respiratory $\theta = 0.5179 \pm 0.0006$ (Luz and Barkan, 2005). The composition for F_A for marine mammals hence is assumed as $\delta^{18}O_A = 22.8 \pm 0.1‰$ and $\Delta'^{17}O_A = -0.421 \pm 0.019‰$.

4.1.3.2 Drinking, osmosis, and food water

The $\delta^{17}O$ and $\delta^{18}O$ of drinking water (F_{DW}) for all marine vertebrates is assumed to be seawater with $\delta^{18}O = 0.4 \pm 0.7‰$ and $\Delta'^{17}O = -0.004 \pm 0.005‰$ (Luz and Barkan, 2010). The same values are also applied to water from both, osmosis F_{OS} and ingested (marine) food F_{FW}. Hence $\delta^{18}O_{OS} = \delta^{18}O_{FW} = 0.4 \pm 0.7‰$ and $\Delta'^{17}O_{OS} = \Delta'^{17}O_{FW} = -0.004 \pm 0.005‰$.

4.1.3.3 Oxygen-bearing inorganic food compounds

The $\delta^{18}O_F$ of dry fish meat is adopted from Chesson et al. (2011) with an average value of $\delta^{18}O_F = 19.2 \pm 1.3‰$. $\delta^{18}O_F$ typically shows a limited variation in absolute values due to being buffered by the $\delta^{18}O$ of ambient seawater during growth. The θ for the fractionation between water and oxygen in organic food compounds is not known and assumed to be 0.526 ± 0.002. This gives a $\delta'^{17}O_F = 1000 \times \ln(\frac{19.2 \pm 1.3‰}{1000} + 1) \times 0.526 \pm 0.002 = 10.0 \pm 0.7‰$ and $\delta^{17}O_F = 10.1 \pm 0.7‰$.

4.1.3.4 Inhaled air humidity

Uemura et al. (2010) presented isotope compositions of atmospheric water vapor at seawater level for the South Indian and the Southern Oceans. We took the average value $\delta^{18}O_{HUM} =$

$-15.5 \pm 2.7‰$, $\delta^{17}O_{HUM} = -8.2 \pm 1.5‰$ and $\Delta'^{17}O_{HUM} = 0.014 \pm 0.011‰$ from Uemura et al. (2010) as the inhaled air water vapor oxygen composition.

4.1.3.4 Exhaled CO_2

For sharks, the metabolic CO_2 dissolves in blood in the form of CO_2, H_2CO_3, HCO_3^-, and CO_3^{2-}. The distribution of carbon between the species is a function of t and pH and has been calculated using the tool provided by Bradley (2017). In the range $7 \leq pH \leq 8$ and $0\,°C \leq t \leq 30\,°C$, HCO_3^- is the dominant species. For sharks, the metabolic CO_2 hence is released in form of HCO_3^-. The isotope fractionation between HCO_3^- and water is given by Beck et al. (2005) as

$$1000 \ln \alpha_{HCO_3^--H_2O} = 2.59\,\frac{10^6}{T^2} + 1.89 \pm 0.04 \qquad \text{Eq. 19}$$

where $\alpha_{HCO_3^--H_2O}$ is the fractionation factor and T being the temperature in kelvin. The HCO_3^- to H_2O fractionation varies between 36.6‰ at 0 °C and 30.1‰ at 30 °C. For the sharks, we use the estimate of the ambient temperature here. For the fractionation in $^{17/16}O$, we use the temperature-dependence of triple isotope exponent by Guo and Zhou (2019) with

$$\theta_{HCO_3^--H_2O} = 0.5249 + 1.504 \times 10^{-5} \times t - 7.857 \times 10^{-8} \times t^2 \qquad \text{Eq. 20}$$

and t being the temperature in °C. At 20 °C, $\theta_{HCO_3^--H_2O}$ is ~ 0.5252.

For marine mammals, exhaled gaseous CO_2 is in equilibrium with body water at 37 ± 1 °C (Lifson and McClintock, 1966; Schoeller et al., 1986; Wong et al., 1988). The $\delta^{18}O$ fractionation between respired CO_2 and body water is adopted from Brenninkmeijer et al. (1983) with fractionation factor $\alpha_{CO2-BW} = 1.0396 \pm 0.0001$ at 37 °C, which gives $\delta^{18}O_{CO2} = 1.0396 \pm 0.0001 \times (\delta^{18}O_{BW} + 1000) - 1000$ with uncertainty 0.05‰. The associated theoretical θ_{CO2-BW} of 0.5246 is derived from Cao and Liu (2011) and Guo and Zhou (2019). The resulting $\delta^{17}O_{CO2}$ is defined as $\delta^{17}O_{CO2} = (1.0396 \pm 0.0001)^{0.5246} \times (\delta^{17}O_{BW} + 1000) - 1000$.

4.1.3.6 Exhaled breath vapor for marine mammals

For marine mammals, F_{BR} vapor is in equilibrium with body water at 37 °C with fractionation factor $\alpha_{BR-BW} = 0.9916$ (Horita and Wesolowski, 1994) with estimated uncertainty ± 0.002 (Pack et al., 2013), which gives $\delta^{18}O_{BR} = 0.9916 \pm 0.002 \times (\delta^{18}O_{BW} +$

1000) – 1000. The combination with the associated $\theta_{\text{BR-BW}}$ of 0.529 ± 0.001 (Barkan and Luz, 2005), gives $\delta^{17}O_{\text{BR}} = (0.9916 \pm 0.002)^{0.529 \pm 0.001} \times (\delta^{17}O_{\text{BW}} + 1000) - 1000$.

4.1.3.7 Liquid water

F_{LW} is not fractionated relative to body water (Lifson et al., 1966; Schoeller et al., 1986; Wong et al., 1988; Bryant and Froelich, 1995) which leads to $\delta^{18}O_{\text{LW}} = \delta^{18}O_{\text{BW}}$ and $\delta^{17}O_{\text{LW}} = \delta^{17}O_{\text{BW}}$.

4.1.1.8 Fractionation between tooth bioapatite and body water

Bioapatite (AP) is assumed to mineralize in isotope equilibrium with body water (BW). The temperature dependent fractionation factors for the apatite-water fractionation ($\alpha^{17/16}_{\text{apatite}-\text{water}}$, $\alpha^{18/16}_{\text{apatite}-\text{water}}$) are adopted from (Hayles et al., 2018).

$$\delta^{17}O_{\text{AP}} = \alpha^{17/16}_{\text{apatite}-\text{water}}\,(T) \times (\delta^{17}O_{\text{BW}} + 1000) - 1000 \qquad \text{Eq. 21}$$

$$\delta^{18}O_{\text{AP}} = \alpha^{18/16}_{\text{apatite}-\text{water}}\,(T) \times (\delta^{18}O_{\text{BW}} + 1000) - 1000 \qquad \text{Eq. 22}$$

The fluxes and isotope compositions are listed in Table 6 and 7. The model uncertainties are calculated by error propagation performing Monte Carlo simulation of the individual parameters with normal or continuous uniform distribution in the given range (Tables 6 and 7). The results are illustrated in Figures 5 and 6.
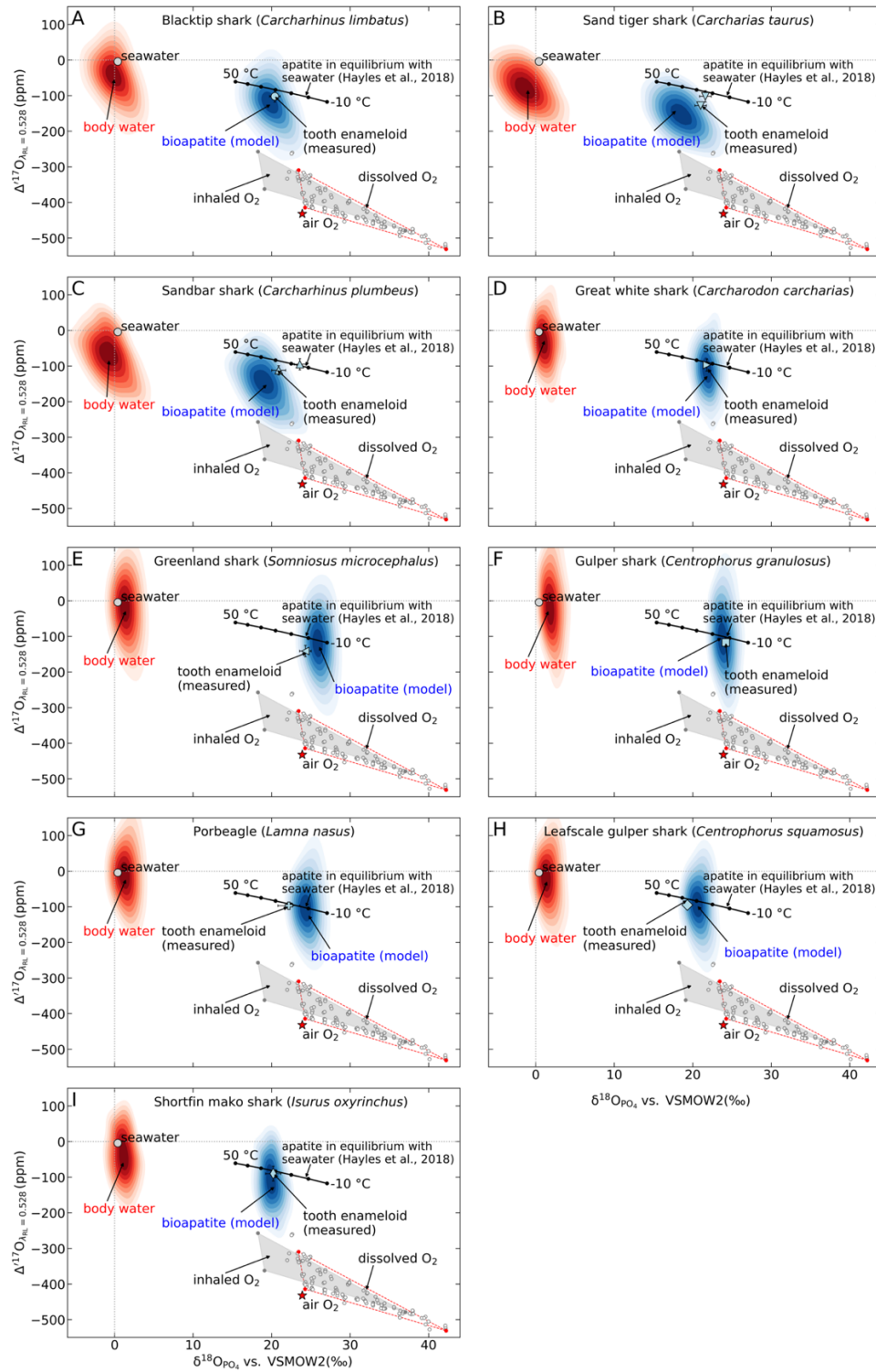
Figure 5: Comparison of $\delta^{18}O_{PO4}$ vs. $\Delta'^{17}O$ calculated with the mass balance model and data measured from shark tooth enameloid. Measured shark bioapatite data are displayed as light-blue circles. The shaded areas outline the result of the mass balance calculations (red: body water; blue: bioapatite). The $\delta^{18}O$ of dissolved O_2 (confined by the triangle marked by the red dots) and ingested dissolved O_2 (gray shaded triangle) are outlined. The apatite-seawater curve of Hayles et al. (2018) is shown for comparison. The red star is the modern air O_2. A: Blacktip shark. B: Sand tiger shark. C: Sandbar shark. D: Great white shark. E: Greenland shark. F: Gulper shark. G: Porbeagle. H: Leafscale gupler shark. I: Shortfin mako shark.
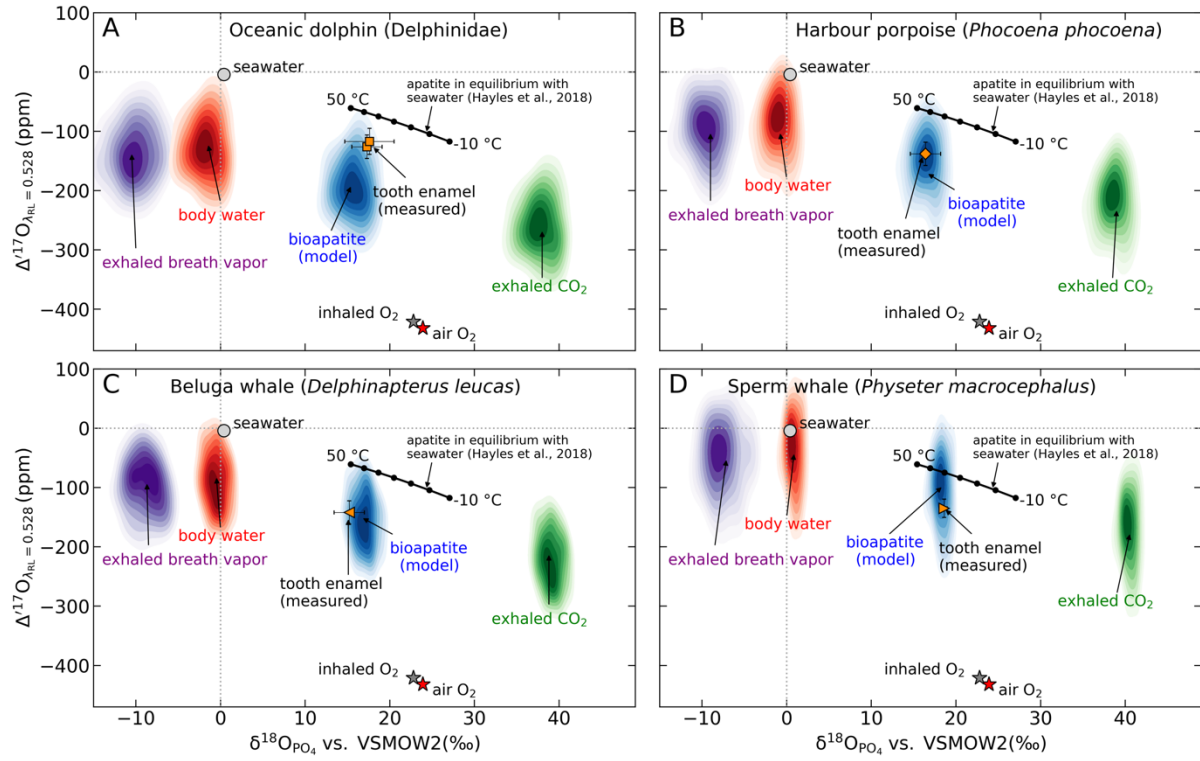
Figure 6: Comparison of $\delta^{18}O_{PO4}$ vs. $\Delta'^{17}O$ calculated with the mass balance model (shaded areas) and measured data from marine mammal tooth enamel (orange-filled symbols). The red star is the modern air O_2. The grey star is the inhaled air O_2 for marine mammals. The red diffuse area is the body water from the model and the blue diffuse area is the tooth enamel composition from the model. The green diffuse area is the exhaled CO_2, and the purple diffuse area is the breath water vapor. A: Oceanic dolphins. B: Harbour porpoise. C: Beluga whale. D: Sperm whale. The apatite-seawater equilibrium curve of Hayles et al. (2018) is shown for comparison.

4.2   Comparison between model and observation

For sharks, a generally good agreement between mass balance model and measured tooth enameloid data is observed (Figure 5). The measured data show a sizable fraction of anomalous metabolic oxygen, which, however cannot be quantitatively resolved by the mass balance because of the large uncertainty of physiological parameters. Instead, the oxygen isotope data may be used to better constrain the physiology of sharks. The lowest $\Delta'^{17}O$ is observed for the Greenland shark that lives in cold waters and is known for its longevity of several hundreds of years and its low degree of physical activity (Nielsen et al., 2016; Augustine et al., 2017; Ste-Marie et al., 2020). Because of the likely low metabolic rates of Greenland sharks, the observed low $\Delta'^{17}O$ indicates that water turnover rate of this shark is likely the lowest among the studied sharks.

Our mass balance model suggests that the body water of sharks has a $\delta^{18}O$ may be slightly higher than ambient seawater, but lower in $\Delta'^{17}O$. This demonstrates that the additional

dimension introduced by ^{17}O brings in can reveal important information about oxygen reservoirs used by the animals for their metabolism. Also, the δ^{18}O of marine vertebrate apatite and ambient water may be used with caution for the determination of $\alpha_{\text{apatite-water}}$ (Longinelli and Nuti, 1973; Kolodny et al., 1983; Pucéat et al., 2010) as the body and environmental water may differ in their oxygen isotope composition.

A good agreement between model and measured bioapatite is also observed for harbor porpoise (Figure 6B) and beluga whale (Figure 6C). The model data and observed data agree within uncertainty. All data clearly fall below the apatite-seawater equilibrium line and indicate a considerable portion of isotopically anomalous metabolic oxygen in the body waters of these marine mammals. The higher specific metabolic rates of mammals compared to fish is reflected in the difference in Δ'^{17}O between our sharks and marine mammals from the same environment. For oceanic dolphins, a higher Δ'^{17}O is observed than suggested by the mass balance model (Figure 6A), which indicates that the ratios between metabolic and water turnover rate are higher than anticipated for the mass balance (Table 7). For sperm whale, a lower Δ'^{17}O is observed than suggested by the mass balance model (Figure 6D), which could indicate that the metabolic rates are underestimated for the mass balance (Table 7). The data for marine mammals show that not only land-living mammals (Levin et al., 2006; Podlesak et al., 2008; Pack et al., 2013; Passey et al., 2014; Blumenthal et al., 2017; Whiteman et al., 2019; Passey and Levin, 2021), but also marine mammals may be used as suitable proxies for the Δ'^{17}O of atmospheric O_2. The high water-efficiency of marine mammals make them in this regard comparable to desert animals, like kangaroo rats, with a high relative portion of metabolic oxygen in their body water.

The δ^{18}O of marine mammal body water is very similar to seawater. However, the strong deviation in ^{17}O demonstrates that marine mammal body water has an origin with a considerable contribution of metabolic water and that the identity in δ^{18}O is rather coincidental and should be used with caution for determination of $\alpha_{\text{apatite-water}}$. Unless one also samples the body water of marine mammals, their bioapatite triple oxygen isotope composition is even less suitable for $\theta_{\text{apatite-water}}$ determination (Pack et al., 2013).

4.3 Triple oxygen isotopes of shark and marine mammal bioapatite as paleo-p_{CO2} (*GPP*) proxy?

Pack et al. (2013) had suggested that the triple O isotope composition of bioapatite of terrestrial mammals may be used as paleo-CO_2 proxy (see Gehler et al. 2016, for a first

application). Using the mass balance, we estimate how sensitive $\Delta'^{17}O$ of bioapatite of sharks and marine mammal reacts to changes in atmospheric O_2 $\Delta'^{17}O$ (Figure 7).
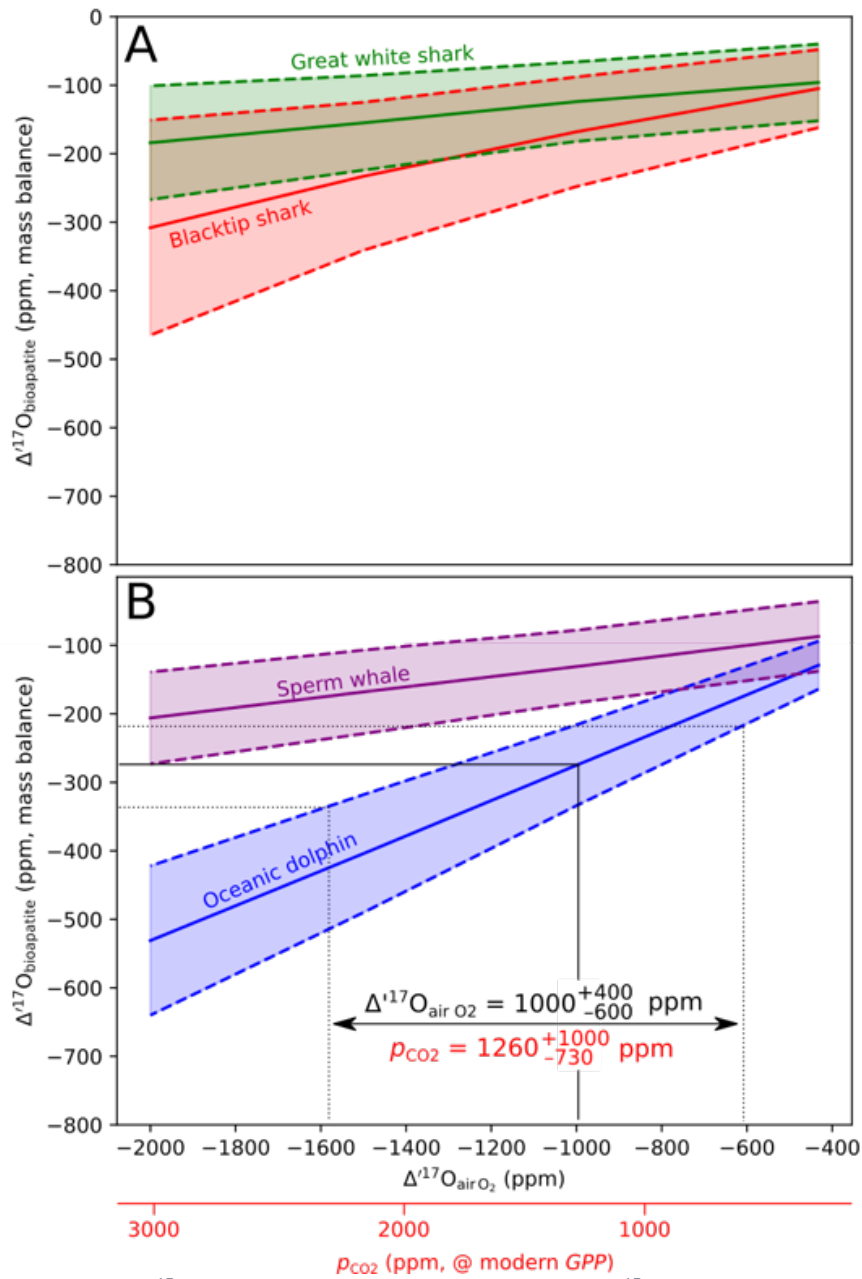
Figure 7: Sensitivity plot of $\Delta'^{17}O$ of bioapatite (from mass balance) vs. $\Delta'^{17}O$ of inhaled air (black axis) and p_{CO2} (@ modern *GPP*, red axis; data from Bao et al., 2008) for (A) Great white shark and blacktip shark and (B) for a sperm whale and oceanic dolphin.

The sensitivity test reveals that shark tooth enamel, at this stage of analytical resolution and understanding of the shark physiology and habits, cannot be used as meaningful proxy for atmospheric $\Delta'^{17}O$ (–2000 ppm ≤ $\Delta'^{17}O$ ≤ –400 ppm) because of its low sensitivity to changes in air O_2 $\Delta'^{17}O$ (Figure 7A). For marine mammal a similar low sensitivity is suggested for the large sperm whale, whereas oceanic dolphin bioapatite may allow reconstruction of air O_2

$\Delta'^{17}O$ (Figure 7B). The model suggests that, at $\Delta'^{17}O_{air\ O2} = -1000$ ppm, a prediction could be done with an uncertainty of +400 and –600 ppm (Figure 7). Converting this into an atmospheric CO_2 mixing ratio (assuming modern GPP), would give values of $p_{CO2} = 1250$ +1000/–730 ppm (Bao et al., 2008). This brief test on the sensitivity illustrates that bioapatite of a small marine mammal could well be used as proxy for past of air O_2 $\Delta'^{17}O$, but that the resolution is limited to high *pCO₂* periods of Earth history. Also, more data on modern species are necessary to better constrain the variability within communities.

5   Conclusions

In summary, we have developed a robust protocol for high-precision triple oxygen isotope analyses of bioapatite. Data for sharks indicate traces of anomalous metabolic oxygen in their tooth enameloid. For marine mammals, a strong negative $\Delta'^{17}O$ anomaly is observed in their enamel and interpreted as being derived from metabolic oxygen. Marine mammal bioapatite triple oxygen isotope data suggest a high water use efficiency for these vertebrates (i.e. the ratio of metabolic oxygen to oxygen from other sources is high). With respect to their water use efficiency, marine mammals could well be grouped together with terrestrial desert mammals. The triple oxygen isotope composition of marine vertebrate bioapatite is a valuable new proxy for animal physiology opening new research avenues. Our data along with a mass balance model demonstrate that fossilized enamel of dolphin-sized marine mammals and other similar metabolically active marine vertebrates may well be used as new paleo-CO_2 (*GPP*) proxy.

6   Acknowledgements

7   References

Aasen O. (1961) Some observations on the biology of the porbeagle shark (*Lamna nasus*). *ICES C. Near North. Seas Comm.* **109**, 7.

Augustine S., Lika K. and Kooijman S. A. L. M. (2017) Comment on the ecophysiology of the Greenland shark, *Somniosus microcephalus*. *Polar Biol*. **40**, 2429–2433.

Bao H., Lyons J. R. and Zhou C. (2008) Triple oxygen isotope evidence for elevated CO_2 levels after a Neoproterozoic glaciation. *Nature* **453**, 504–506.

Barkan E. and Luz B. (2005) High precision measurements of $^{17}O/^{16}O$ and $^{18}O/^{16}O$ ratios in H_2O. Rapid Commun. *Mass Spectrom*. **19**, 3737–3742.

Beck W. C., Grossman, E. L. and Morse, J. W. (2005) Experimental studies of oxygen isotope fractionation in the carbonic acid system at 15°, 25°, and 40°C, *Geochim. Cosmochim. Acta* **69**, 3493–3503.

Bender M. L., Sowers T., Barnola J. M. and Chappellaz J. (1994) Changes in the O_2/N_2 ratio of the atmosphere during. *Geophys. Res. Lett*. **21**, 189–192.

Beverly E. J., Levin N. E., Passey B. H., Aron P. G., Yarian D. A., Page M. and Pelletier E. M. (2021) Triple oxygen and clumped isotopes in modern soil carbonate along an aridity gradient in the Serengeti, Tanzania. *Orphanet J. Rare Dis*. **21**, 1–9.

Blumenthal S. A., Levin N. E., Brown F. H., Brugal J. P., Chritz K. L., Harris J. M., Jehle G. E., Cerling T. E. and O'Connell J. (2017) Aridity and hominin environments. *Proc. Natl. Acad. Sci. U. S. A*. **114**, 7331–7336.

Bradley A. (2017): CO_2 equilibria calculator for Excel. figshare. Software. https://doi.org/10.6084/m9.figshare.5593420.v1 .

Brenninkmeijer C. A. M., Kraft P. and Mook W. G. (1983) Oxygen isotope fractionation between CO_2 and H_2O. *Chem. Geol*. **41**, 181–190.

Bryant D. J. and Froelich P. N. (1995) A model of oxygen isotope fractionation in body water of large mammals. *Geochim. Cosmochim. Acta* **59**, 4523–4537.

Cao X. and Liu Y. (2011) Equilibrium mass-dependent fractionation relationships for triple oxygen isotopes. *Geochim. Cosmochim. Acta* **75**, 7435–7445.

Carrier J. C., Musick A. John, Heithaus Michael R. (2012) Biology of sharks and their relatives second edition. CRC Press Taylor & Francis Group. *Journal of chemical information and modeling* **53**, p239.

Chang S.J. and Blake R.E. (2015) Precise calibration of equilibrium oxygen isotope fractionations between dissolved phosphate and water from 3 to 37 °C. *Geochim.*

Cosmochim. Acta **150**, 314–329.

Chesson L. A., Valenzuela L. O., Bowen G. J., Cerling T. E. and Ehleringer J. R. (2011) Consistent predictable patterns in the hydrogen and oxygen stable isotope ratios of animal proteins consumed by modern humans in the USA. *Rapid Commun. Mass Spectrom*. **25**, 3713–3722.

Chenery C., Müldner G., Evans J., Eckardt H. and Lewis M. (2010) Strontium and stable isotope evidence for diet and mobility in Roman Gloucester, UK. *J. Archaeol. Sci*. **37**, 150–163.

Clarke M. R. (1977) Beaks, nets and numbers. In The Biology of Cephalopods. Nixon, M. and J. B. Messenger (Eds). *London; Academic Press*, 89–126.

Dettman D. L., Kohn M. J., Quade J., Ryerson F. J., Ojha T. P. and Hamidullah S. (2001) Seasonal stable isotope evidence for a strong Asian monsoon throughout the past 10.7 m.y. *Geology* **29**, 31–34.

Dowd W. W., Brill R. W., Bushnell P. G. and Musick J. A. (2006) Standard and routine metabolic rates of juvenile sandbar sharks (*Carcharhinus plumbeus*), including the effects of body mass and acute temperature change. *Fish. Bull.* **104**, 323–331.

Epstein S. and Zeiri L. (1988) Oxygen and carbon isotopic compositions of gases respired by humans. *Proc. Natl. Acad. Sci. U. S. A*. **85**, 1727–1731.

Fetcher E. S. and Fetcher G. W. (1942) Experiments on the osmotic regulation of dolphins. *J. Cell. Comp*, 181–191.

Gehler A., Tütken T. and Pack A. (2012) Oxygen and Carbon Isotope Variations in a Modern Rodent Community - Implications for Palaeoenvironmental Reconstructions. *PLoS ONE* **7**, 16–27.

Gehler A., Gingerich P. D. and Pack A. (2016) Temperature and atmospheric CO_2 concentration estimates through the PETM using triple oxygen isotope analysis of mammalian bioapatite. *Proc. Natl. Acad. Sci. U. S. A*. **113**, 7739–7744.

Guo W. and Zhou C. (2019) Triple oxygen isotope fractionation in the DIC-H_2O-CO_2 system: A numerical framework and its implications. *Geochim. Cosmochim. Acta* **246**, 541–564.

Hayles J., Gao C., Cao X., Liu Y. and Bao H. (2018) Theoretical calibration of the triple oxygen isotope thermometer. *Geochim. Cosmochim. Acta* **235**, 237–245.

Horita J. and Wesolowski D. J. (1994) Liquid-vapor fractionation of oxygen and hydrogen isotopes of water from the freezing to the critical temperature. *Geochim. Cosmochim. Acta* **58**, 1–13.

Hui C. A. (1981) Seawater consumption and water flux in the common dolphin *Delphinus delphis*. *Physiol. Zool*. **54**, 430–440.

Hulston J. R. and Thode H. G. (1965) Variations in the S^{33} S^{34} and S^{36} Contents of Meteorites and Their Relation to Chemical and Nuclear Effects. *J. Geophys. Res*. **70**, 3475–3484.

Irving L., Scholander P. F. and Grinnell S. W. (1941) The respiration of the porpoise, *Tursiops truncatus. J. Cell. Comp. Physiol.* **17**, 145–168.

Kastelein R. A., Ford J., Berghout E., Wiepkema P. R. and van Boxsel M. (1994) Food consumption, growth and reproduction of belugas (*Delphinapterus leucas*) in human care. *Aquat. Mamm*. **20**, 81–97.

Kawakami T. (1980) A review of sperm whale food. *Sci. Reports Whales Res. Inst*. **32**, 199–218.

Kjeld M. (2003) Salt and water balance of modern baleen whales: Rate of urine production and food intake. *Can. J. Zool*. **81**, 606–616.

Kleiber M. (1947) Body size and metabolic rate. *Physiol. Rev*. **27**, 511–541.

Kolodny Y., Luz B. and Navon O. (1983) Oxygen isotope variations in phosphate of biogenic apatites, I. Fish bone apatite-rechecking the rules of the game. *Earth Planet. Sci. Lett*. **64**, 398–404.

Lear K. O., Whitney N. M., Brewster L. R., Morris J. J., Hueter R. E. and Gleiss A. C. (2017) Correlations of metabolic rate and body acceleration in three species of coastal sharks under contrasting temperature regimes. *J. Exp. Biol*. **220**, 397–407.

Lee-Thorp J. A., Sponheimer M. and Luyt J. (2007) Tracking changing environments using stable carbon isotopes in fossil tooth enamel: an example from the South African hominin sites. *J. Hum. Evol*. **53**, 595–601.

Levin N. E., Cerling T. E., Passey B. H., Harris J. M. and Ehleringer J. R. (2006) A stable isotope aridity index for terrestrial environments. *Proc. Natl. Acad. Sci. U. S. A.* **103**, 11201–11205.

Lécuyer C., Grandjean P., O'Neil J. R., Cappetta H. and Martineau F. (1993) Thermal excursions in the ocean at the Cretaceous-Tertiary boundary (northern Morocco): $\delta^{18}O$ record of phosphatic fish debris. *Palaeogeogr. Palaeoclimatol. Palaeoecol.* **105**, 235–243.

Lifson N. and McClintock R. (1966) Theory of use of the turnover rates of body water for measuring energy and material balance. *J. Theor. Biol*. **12**, 46–74.

Longinelli A. and Nuti S. (1973) Revised phosphate-water isotopic temperature scale. *Earth Planet. Sci. Lett.* **19**, 373–376.

Löffler N., Fiebig J., Mulch A., Tütken T., Schmidt B. C., Bajnai D., Conrad A. C., Wacker U. and Böttcher M. E. (2019) Refining the temperature dependence of the oxygen and clumped isotopic compositions of structurally bound carbonate in apatite. *Geochim. Cosmochim. Acta* **253**, 19–38.

Luz B., Barkan E., Bender M. L., Thiemens M. H. and Boering K. A. (1999) Triple-isotope composition of atmospheric oxygen as a tracer of biosphere productivity. *Nature* **400**, 547–550.

Luz B. and Barkan E. (2005) The isotopic ratios $^{17}O/^{16}O$ and $^{18}O/^{16}O$ in molecular oxygen and their significance in biogeochemistry. *Geochim. Cosmochim. Acta* **69**, 1099–1110.

Luz B. and Barkan E. (2010) Variations of $^{17}O/^{16}O$ and $^{18}O/^{16}O$ in meteoric waters. *Geochim. Cosmochim. Acta* **74**, 6276–6286.

Murray J. and Burt, J. R. (1983). The composition of fish printed in seed bond by her majesty stationary office (HMSO) Press. Edinburgh.

Matt Menne (2000) Global long-term mean land and sea surface temperatures. National Climatic Data Center.

Medved R. J., Stillwell C. E. and Casey J. G. (1988) The rate of food consumption of young Sandbar sharks (*Carcharhinus plumbeus*) in Chincoteague Bay, Virginia. Copeia 1988, 956–965.

Meynier L., Pusineri C., Spitz J., Santos M. B., Pierce G. J. and Ridoux V. (2008) Intraspecific dietary variation in the short-beaked common dolphin *Delphinus delphis* in the Bay of Biscay: Importance of fat fish. *Mar. Ecol. Prog. Ser.* **354**, 277–287.

Nave R. (2000) HyperPhysics Thermodynamics. http://hyperphysics.phy-astr.gsu.edu/hbase/Kinetic/relhum.html.

Nielsen J., Hedeholm R. B., Heinemeier J., Bushnell P. G., Christiansen J. S., Olsen J., Ramsey C. B., Brill R. W., Simon M., Steffensen K. F. and Steffensen J. F. (2016) Eye lens radiocarbon reveals centuries of longevity in the Greenland shark (*Somniosus microcephalus*). *Science* **353**, 702–704.

Ortiz R. M. (2001) Osmoregulation in marine mammals. *J. Exp. Biol.* **204**, 1831–1844.

Pack A., Gehler A. and Süssenberger A. (2013) Exploring the usability of isotopically anomalous oxygen in bones and teeth as paleo-CO_2-barometer. *Geochim. Cosmochim. Acta* **102**, 306–317.

Pack A., Tanaka R., Hering M., Sengupta S., Peters S. and Nakamura E. (2016) The oxygen isotope composition of San Carlos olivine on the VSMOW2-SLAP2 scale. *Rapid Commun. Mass Spectrom.* **30**, 1495–1504.

Pack A., 2021. Isotopic traces of atmospheric O_2 in rocks, minerals, and melts. *Rev. Mineral. Geochemistry* **86**, 217–240.

Passey B. H., Hu H., Ji H., Montanari S., Li S., Henkes G. A. and Levin N. E. (2014) Triple oxygen isotopes in biogenic and sedimentary carbonates. *Geochim. Cosmochim. Acta* **141**, 1–25.

Passey B. H. and Levin N. E. (2021) Triple oxygen isotopes in carbonates, biological apatites, and continental paleoclimate reconstruction. *Rev. Mineral. Geochemistry* **86**, 429–462.

Piiper J., Schumann D. (1967) Efficiency of O_2 exchange in the gills of the dogfish, *Scyliorhinus stellaris*. *Respir. Physiol.* **2**, 135–148.

Podlesak D. W., Torregrossa A. M., Ehleringer J. R., Dearing M. D., Passey B. H. and Cerling T. E. (2008) Turnover of oxygen and hydrogen isotopes in the body water, CO_2, hair, and enamel of a small mammal. *Geochim. Cosmochim. Acta* **72**, 19–35.

Pucéat E., Joachimski M.M., Bouilloux A., Monna F., Bonin A., Motreuil S., Morinière P., Hénard S., Mourin J., Dera G. and Quesne D. (2010) Revised phosphate-water fractionation equation reassessing paleotemperatures derived from biogenic apatite. *Earth and planetary Science Letters* **298**, 135–142.

Rash R. and Lillywhite H. B. (2019) Drinking behaviors and water balance in marine vertebrates. *Mar. Biol.* **166**, 1–21.

Ridgway S. H. and Patton G. S. (1971) Dolphin thyroid: Some anatomical and physiological findings. *Z. Vgl. Physiol.* **71**, 129–141.

Rosen D. A. S. and Trites A. W. (2013) Short note resting metabolic rate of a mature male beluga whale (*Delphinapterus leucas*). *Aquat. Mamm.* **39**, 85–88.

Rojano-Donãte L., McDonald B. I., Wisniewska D. M., Johnson M., Teilmann J., Wahlberg M., Højer-Kristensen J. and Madsen P. T. (2018) High field metabolic rates of wild harbour porpoises. *J. Exp. Biol.* **221,** 1–12.

Santos M. B., Pierce G. J., Ieno E. N., Addink M., Smeenk C., Kinze C. C. and Sacau M. (2005) Harbour porpoise (*Phocoena phocoena*) feeding ecology in the eastern North Sea. ICES C. *Mar. Mamm. Monit. Tech. Abundance Estim. Interact. with Fish*. **15**, 1–25.

Sepulveda C. A., Graham J. B. and Bernal D. (2007) Aerobic metabolic rates of swimming juvenile mako sharks, *Isurus oxyrinchus*. *Mar. Biol.* **152**, 1087–1094.

Schoeller D. A., Leitch C. A. and Brown C. (1986) Doubly labeled water method: In vivo oxygen and hydrogen isotope fractionation. Am. J. Physiol. - Regul. Integr. *Comp. Physiol.* **251**, 1137–1143.

Schmid T. H., F. L. Murru, and F. McDonald. 1990. Feeding habits and growth rates of bull (*Carcharhinus leucas* (Valenciennes)), sandbar (*Carcharhinus plumbeus* (Nardo)), sand tiger (*Eugomphodus taurus* (Rafinesque)) and nurse (*Ginglymostoma cirratum* (Bonnaterre)) sharks maintained in captivity. *J. Aquaricult. Aquat. Sci*. **5**, 100–105.

Semmens J. M., Payne N. L., Huveneers C., Sims D. W. and Bruce B. D. (2013) Feeding requirements of white sharks may be higher than originally thought. *Sci. Rep.* **3**, 10–13.

Sharp Z. D. (1990) A laser-based microanalytical method for the in situ determination of oxygen isotope ratios of silicates and oxides. *Geochim. Cosmochim. Acta* **54**, 1353–1357.

Sharp Z. D., Gibbons J. A., Maltsev O., Atudorei V., Pack A., Sengupta S., Shock E. L. and Knauth L. P. (2016) A calibration of the triple oxygen isotope fractionation in the SiO_2-H_2O system and applications to natural samples. *Geochim. Cosmochim. Acta* **186**, 105–119.

Sims D. W. (2000) Can threshold foraging responses of basking sharks be used to estimate their metabolic rate? *Mar. Ecol. Prog. Ser*. **200**, 289–296.

Ste-Marie E., Watanabe Y. Y., Semmens J. M., Marcoux M. and Hussey N. E. (2020) A first look at the metabolic rate of Greenland sharks (*Somniosus microcephalus*) in the Canadian Arctic. *Sci. Rep.* **10**, 1–8.

Surma J., Assonov S. and Staubwasser M. (2021) Triple Oxygen Isotope Systematics in the Hydrologic Cycle. *Rev. Mineral. Geochemistry* **86**, 401–428.

Thiemens M. H. (2006) History and applications of mass-independent isotope effects. *Ann. Rev. Earth Planet. Sci*. **34**, 217–262.

Tütken T., Vennemann T. W., Janz H. and Heizmann E. P. J. (2006) Palaeoenvironment and palaeoclimate of the Middle Miocene lake in the Steinheim basin, SW Germany: A reconstruction from C, O, and Sr isotopes of fossil remains. *Palaeogeogr. Palaeoclimatol. Palaeoecol*. **241**, 457–491.

Telfer N., Cornell, L. H. and Prescott, J. H. (1970) Do dolphins drink water? *J. Zool.* **222**, 29–42 J Am Vet Med Assoc. 1970 Sep 1;157(5):555-8.

Uemura R., Barkan E., Abe O. and Luz B. (2010) Triple isotope composition of oxygen in atmospheric water vapor. *Geophys. Res. Lett*. **37**, 1–4.

Vennemann T. W., Fricke H. C., Blake R. E., O'Neil J. R. and Colman A. (2002) Oxygen isotope analysis of phosphates: A comparison of techniques for analysis of Ag_3PO_4. *Chem. Geol*. **185**, 321–336.

Wartzok D. (2009). Breathing. In W. F. Perrin, B. Würsig & J. G. M. Thewissen (Eds.),

Encyclopedia of marine mammals (2nd ed., pp. 152-156). San Diego, CA: Academic Press.

Watanabe Y. Y., Payne N. L., Semmens J. M., Fox A. and Huveneers C. (2019) Swimming strategies and energetics of endothermic white sharks during foraging. *J. Exp. Biol*. **222** (4): jeb185603.

Walker S. M. (2007) Dolphins. Lerner Publications, Minneapolis.

Wegner N. C., Lai N. C., Bull K. B. and Graham J. B. (2012) Oxygen utilization and the branchial pressure gradient during ram ventilation of the shortfin mako, *Isurus oxyrinchus*: Is lamnid shark-tuna convergence constrained by elasmobranch gill morphology? *J. Exp. Biol*. **215**, 22–28.

Whiteman J. P., Sharp Z. D., Gerson A. R. and Newsome S. D. (2019) Relating $\Delta^{17}O$ values of animal body water to exogenous water inputs and metabolism. *BioScience* **69**, 658–668.

Williams T. M., Friedl W. A. and Haun J. E. (1993) The physiology of bottlenose dolphins (*Tursiops truncatus*): heart rate, metabolic rate and plasma lactate concentration during exercise. *J. Exp. Biol*. **179**, 31–46.

Williams T. M., Haun J., Davis R. W., Fuiman L. A. and Kohin S. (2001) A killer appetite: Metabolic consequences of carnivory in marine mammals. *Comp. Biochem. Physiol. - A Mol. Integr. Physiol*. **129**, 785–796.

Wood A. D., Wetherbee B. M., Juanes F., Kohler N. E. and Wilga C. (2009) Recalculated diet and daily ration of the shortfin mako (*Isurus oxyrinchus*), with a focus on quantifying predation on bluefish (*Pomatomus saltatrix*) in the northwest Atlantic Ocean. *Fish. Bull.* **107**, 76–88.

Wong W. W., Cochran W. J., Klish W. J., O'Brian Smith E., Lee L. S. and Klein P. D. (1988) In vivo isotope-fractionation factors and the measurement of deuterium- and oxygen-18-dilution spaces from plasma, urine, saliva, respiratory water vapor, and carbon dioxide. *Am. J. Clin. Nutr*. **47**, 1–6.

Wostbrock J. A. G., Cano, E. J. and Sharp, Z. D. (2020) An internally consistent triple oxygen isotope calibration of standards for silicates, carbonates and air relative to VSMOW2 and SLAP2. *Chem. Geol.* **533**, 119432.

Yasui W. Y. and Gaskin D. E. (1986) Energy budget of a small cetacean, the harbour porpoise, *Phocoena phocoena* (L.). *Ophelia* **25**, 183–197.

Yeung L. 2020. Dataset: dissolved O_2. Biological & Chemical Oceanography Data Management Office. https://www.bco-dmo.org/dataset/753594.

Young E. D., Galy A. and Nagahara H. (2002) Kinetic and equilibrium mass-dependent isotope fractionation laws in nature and their geochemical and cosmochemical significance. *Geochim. Cosmochim. Acta* **66**, 1095–1104.

Young E. D., Yeung L. Y. and Kohl I. E. (2014) On the $\delta^{17}O$ budget of atmospheric O_2. *Geochim. Cosmochim. Acta* **135**, 102–125.

Chapter 3 Triple oxygen isotopes of modern terrestrial mammalian tooth enamel –new implications for paleoenvironmental and physiological research

Dingsu Feng, Thomas Tütken, Niklas Löffler, Gert Tröster, Gisa Heinemann, Fabian Zahnow, Jacub Surma & Andreas Pack, 2022. This work will be submitted to *Earth and Planetary Science Letters*.

Abstract

Triple oxygen isotope ($\Delta'^{17}O$) analysis has recently be shown to be a powerful tool for identifying metabolic oxygen signatures in marine mammalian tooth enamel. Here, it is investigated if this principle is also applicable to terrestrial mammals with varying body sizes (0.008 to 6,000 kg) and energy consumptions (4 to 1.25×10^6 kJ×day^{-1}). Therefore, 128 individuals are investigated for their bioapatite $\Delta'^{17}O$ which are then combined with taxon specific oxygen mass balance models for resolving principal dependencies and relationships. It can be shown, that $\Delta'^{17}O$ not only correlates with body mass, but also initial oxygen anomalies of inhaled air O_2, which can be related to atmospheric pCO_2. This documents the potential of tooth enamel $\Delta'^{17}O$ analysis for paleoclimate reconstruction, especially for small mammals ($M_b < 1$ kg).

1   Introduction

Triple oxygen isotope analysis ($\Delta'^{17}O$) of marine vertebrate tooth enamel(oid) has previously been shown to result in $\Delta'^{17}O$ values that can be related to results from detailed oxygen mass balance models (Feng et al., 2022). This enables the quantification of biasing metabolic effects and oxygen isotope anomalies of different reservoirs such as inhaled air O_2 (Feng et al., 2022; their mammal data). Expanding this concept to terrestrial mammals could potentially enable the reconstruction of both metabolic rates of extinct vertebrates and atmospheric $\Delta'^{17}O$. Because the latter depends on the bulk composition of the atmosphere (Bender et al., 1994; Luz et al., 1999), it should be feasible to reconstruct atmospheric CO_2 concentrations from measured terrestrial mammalian tooth enamel $\Delta'^{17}O$ if the gross primary production (*GPP*), taxon specific oxygen mass balances, and associated oxygen isotope fractionation are considered.

Arrhenius (1896) first discussed that variations in atmospheric CO_2 concentrations can be related to climate variability. A close correlation between atmospheric CO_2 partial pressure

(pCO$_2$) and temperature is well-established for the past ~ 800 ka from ice core data (Foster et al., 2017; Lüthi et al., 2008; Petit et al., 1999). For older ages, temperatures can be derived from carbonate δ^{18}O (Urey et al., 1951; Veizer et al., 2000) and atmospheric CO$_2$ levels are estimated from mass balance models (Berner, 2006a, 2006b) or geological proxies (Breecker et al., 2010; Kürschner et al., 2008; Pagani et al., 2005; Pearson et al., 2009; Roth-Nebelsick, 2005; Royer et al., 2001) whereas these proxies are associated with unavoidable analytical uncertainties and individual limitations. This highlights the importance of developing additional pCO$_2$ proxies to further increase the precision of reconstructed pCO$_2$, *e.g.* by a multiproxy approach.

Yung et al. (1991), who was confirmed by Blunier et al. (2002), proposed that Δ'^{17}O of air O$_2$ varies with atmospheric CO$_2$ concentrations. Higher than modern CO$_2$ concentrations result in lower Δ'^{17}O values of O$_2$ and *vice versa*. Apart from atmospheric CO$_2$ concentration, Δ'^{17}O of atmospheric O$_2$ also depends on the gross primary production (*GPP*; Luz et al., 1999; Young et al., 2014). High *GPP* lead to a smaller anomaly of air O$_2$, whereas low *GPP* amplifies the Δ'^{17}O "anomaly" of air O$_2$. Air O$_2$ Δ'^{17}O therefore reflects both atmospheric CO$_2$ concentration and *GPP* at a given time. Based on sulphate Δ'^{17}O, Bao et al. (2008) reconstructed a high pCO$_2$ level of ~ 12,000 ppm during the Early Cambrian (750 Ma) and suggested that the sulphate Δ'^{17}O record can be used to evaluate extreme levels of atmospheric CO$_2$ or O$_2$ throughout Earth's history. Natural sulfate can originate from oxidative weathering (Bao et al., 2008) and carries an Δ'^{17}O signal that represents air O$_2$ during sulfate formation. In turn, Δ'^{17}O tracks air O$_2$ and – besides *GPP* – reflects pCO$_2$. Passey et al. (2014) and Passey and Levin (2021) demonstrated that inhaled anomalous O$_2$ is also reflected in egg shell calcite Δ'^{17}O. Beverly et al. (2020) proposed that Δ'^{17}O of structural carbonate in bioapatite can not only be used to derive physiological data, but also as an environmental proxy as Δ'^{17}O is interlinked with the respective isotopes in the water cycle (see review by Surma et al., 2021). Pack et al. (2013) suggested that bioapatite of terrestrial mammals can be used to approximate the Δ'^{17}O of ambient air and hence pCO$_2$. Atmospheric O$_2$ is consumed by mammals for metabolic oxidation of carbohydrate, fat, and protein. Resulting oxidation products preserve the O$_2$ isotopic signature and either directly contribute to (metabolic H$_2$O) or equilibrate with (CO$_2$) the specimen's body water; a principle that also applies to non-mammalian vertebrates. Bioapatite precipitates in isotopic equilibrium with its parental body water at a given body temperature and consequently inherits information on the air O$_2$ Δ'^{17}O which allows for pCO$_2$ reconstruction on terrestrial mammalian tooth enamel.

In contrast to terrestrial sulfate, the amount of oxygen from inhaled air O_2 can be estimated using an oxygen mass balance model (Bryant and Froelich, 1995; Pack et al., 2013; Feng et al., 2022). However, the oxygen mass balance model has large intrinsic uncertainties, for example due to taxon-specific physiological variations. From the fossil record, many mammals are extinct. The interpretation of the measured $\Delta'^{17}O$ from fossil bioapatite therefore requires detailed triple oxygen isotope mass balance models of modern analogues that cover a wide range of body masses and metabolic rates. Here, we present data sets of 128 modern terrestrial mammals with a body mass range from 2 g to 6,000 kg from five different continents along with detailed taxon-specific oxygen mass balance models. The paired experimental and modeled data can be used to verify their conformity, which is mandatory for future interpretation of fossil data.

2   Materials and Methods

2.1   Definitions

The oxygen isotope data are reported in the conventional $\delta^{17}O$ (Eq. 1) and $\delta^{18}O$ (Eq. 2) notation as:

$$\delta^{17}O_{\text{VSMOW2}}^{\text{sample}} = 1000 \times \left(\frac{(^{17}O/^{16}O)_{\text{sample}}}{(^{17}O/^{16}O)_{\text{VSMOW2}}} - 1 \right) \qquad \text{Eq. 3}$$

$$\delta^{18}O_{\text{VSMOW2}}^{\text{sample}} = 1000 \times \left(\frac{(^{18}O/^{16}O)_{\text{sample}}}{(^{18}O/^{16}O)_{\text{VSMOW2}}} - 1 \right) \qquad \text{Eq. 4}$$

The $\delta'^{17}O$ (Eq. 3) and $\delta'^{18}O$ (Eq. 4) notation were introduced as the linearized version of the δ-notation (Hulston and Thode, 1965; Young et al., 2002):

$$\delta'^{17}O_{\text{VSMOW2}}^{\text{sample}} = 1000 \times \ln \left(\frac{\delta^{17}O_{\text{VSMOW2}}^{\text{sample}}}{1000} + 1 \right) \qquad \text{Eq. 5}$$

$$\delta'^{18}O_{\text{VSMOW2}}^{\text{sample}} = 1000 \times \ln \left(\frac{\delta^{18}O_{\text{VSMOW2}}^{\text{sample}}}{1000} + 1 \right) \qquad \text{Eq. 6}$$

We define triple oxygen isotope deviations from a given reference line ($\lambda_{RL} = 0.528$) in form of the $\Delta'^{17}O$ value (Eq. 5).

$$\Delta'^{17}O_{0.528} = \delta'^{17}O_{\text{VSMOW2}}^{\text{sample}} - 0.528 \times \delta'^{18}O_{\text{VSMOW2}}^{\text{sample}} \qquad \text{Eq. 7}$$

The triple oxygen isotope fractionation between phases (A, B) is described by the fractionation factor α_{A-B} and the triple oxygen isotope fractionation exponent θ_{A-B} (Young et al., 2002) as:

$$\alpha_{A-B}^{17/16} = \left(\alpha_{A-B}^{18/16}\right)^{\theta_{A-B}} \qquad \text{Eq. 8}$$

Each equilibrium fractionation process has an individual θ value. The fractionation factors $\alpha_{A-B}^{17/16}$ and $\alpha_{A-B}^{18/16}$ are the ratios of the $^{17}O/^{16}O$ and $^{18}O/^{16}O$, respectively, of coexisting phases A and B presented as:

$$\alpha_{A-B}^{17/16} = \frac{\delta^{17/16}O_A + 1000}{\delta^{17/16}O_B + 1000} \qquad \text{Eq. 9}$$

$$\alpha_{A-B}^{18/16} = \frac{\delta^{18/16}O_A + 1000}{\delta^{18/16}O_B + 1000} \qquad \text{Eq. 10}$$

2.2 Terrestrial mammals

In this study, $\Delta'^{17}O$ of tooth enamel and bulk teeth of 128 individual specimens of modern terrestrial herbivorous, omnivorous and carnivorous mammals with body masses ranging from ~ 2 g to ~ 6000 kg were analyzed. More specifically, these taxa comprise 18 antelopes of *Artiodactyla*, 1 *Hippopotamus amphibius* and 1 *Loxodonta africana* (AG-Lox; Gehler et al. 2012) from Africa, 12 *Diprotodontia* and 1 *Sarcophilus* from Australia, 1 *Didelphis* and 1 *Didelphis virginiana* from North America, 1 *Procyon cancrivorus* from South America. These varying taxa are complemented by samples from Europe (Germany), including 29 *Capreolus capreolus*, 10 *Sus scrofa*, 3 *Meles meles*, 6 *Vulpes vulpes*, 5 *Talpa europaea* and another 41 different species. A detailed overview of the individual taxa and the related physical characteristic are presented in Appendix S1. All individual specimens were captured from their natural habitats and reflect different environments whereas most samples were collected by the Biodiversity Museum of Göttingen (Germany).

2.3 Bioapatite sample preparation

Following Feng et al. (2022), we separated tooth enamel from tooth dentine using a micro drill equipped with a dental diamond tip. For rodents, sample powder was prepared from bulk teeth due to the quantities needed per analysis. For removing organic matter, the tooth enamel powder was treated with 2% NaClO for 45 minutes and 0.1% CH_3COOH for 15minutes, then rinsed with distilled water 5 times for each step and dried overnight at 70 °C (Lee-Thorp et

al., 2007). The same pretreatment was applied to the reference materials Florida phosphate rock standard (NBS 120c, Lécuyer et al., 1993) and AG-Lox (Gehler et al. 2012).

2.4   Oxygen isotope analyses

2.4.1   Carbon and Oxygen isotope analyses of the bioapatite carbonate group

After chemical pretreatment, 1.2 to 1.4 mg powder was reacted with > 103% H_3PO_4 at 70 °C for 15 minutes in an automated Thermo Scientific™ KIEL IV Carbonate Device (Thermo Fisher Scientific, Bremen, Germany). The carbon ($\delta^{13}C$) and oxygen isotopic composition ($\delta^{18}O_{CO3}$) of the liberated CO_2 were then analyzed on a Thermo Finnigan Delta Plus gas source mass spectrometer in dual inlet mode at the stable isotope laboratory of the Geoscience Center at the University of Göttingen, Germany. Further details on these analytical systems are provided in Gehler et al. (2012) and Sisma-Ventura et al. (2019).

Sample $\delta^{13}C$ and $\delta^{18}O_{CO3}$ were normalized to the internal Solnhofen carbonate standard measured during the same sessions with $\delta^{13}C$ = -0.185 ± 0.08‰ and $\delta^{18}O_{CO3}$ = 25 ± 0.05‰ (n = 30). For chemically untreated NBS 120c, we obtained $\delta^{13}C$ = -6.34 ± 0.05‰ and $\delta^{18}O_{CO3}$ = 29.95 ± 0.12‰ (n = 26). For chemically pretreated NBS 120c, we obtained $\delta^{13}C$ = -6.46 ± 0.18‰ and $\delta^{18}O_{CO3}$ = 29.96 ± 0.13‰ (n = 6). Analysis of chemically untreated AG-Lox resulted in $\delta^{13}C$ = -12.04 ± 0.09‰ and $\delta^{18}O_{CO3}$ = 30.02 ± 0.11‰ (n = 27). Chemically pretreated AG-Lox was measured with $\delta^{13}C$ = -12.16 ± 0.08‰ and $\delta^{18}O_{CO3}$ = 30.11 ± 0.17‰ (n = 11). These AG-Lox mean values compare well with previously reported values of $\delta^{13}C$ = -11.78 ± 0.12‰ and $\delta^{18}O_{CO3}$ = 30.30 ± 0.17‰ (Wacker et al., 2016) (n = 23).

2.4.2   Laser fluorination triple oxygen isotope analyses

In order to remove organic material, carbonate, and OH groups, samples were heated to 1000 °C for 30 mins in a horizontal furnace in a constant H_2-N_2 gas stream (50 ml/min; 10% H_2, 90% N_2). Lindars et al. (2001) demonstrated that these compounds decompose between 850 and 1000 °C while the phosphate group remains unaffected. To avoid exchange with the atmosphere, samples were cooled down below 100 °C while being continuously flushed with the H_2-N_2 gas mixture and, in a following step, quickly transferred and stored in a desiccator (Feng et al., 2022).

The $\Delta'^{17}O$ analyses were conducted by means of laser fluorination (LF) in combination with multi collector gas source mass spectrometry (Sharp, 1990) whereas details are explained in

Pack et al. (2013, 2016). Approximately 2.5 mg of preheated tooth enamel was placed into a polished Ni metal sample holder with 14 pits, along with the AG-Lox and San Carlos Olivine (Pack et al., 2016) standards. After loading the sample holder into the sample chamber and evacuating it for at least 12 hours, tooth enamel was pre-melted with up to 5.5% laser power (SYNRAD 50 W CO_2 laser). After evacuation and heating of the sample chamber to 70 °C overnight, each sample was reacted with purified BrF_5 gas by means of heating with a SYNRAD 50 W CO_2 laser. The extracted O_2 was cryogenically purified by a molecular sieve (5 Å mesh) held at -196 °C (liquid nitrogen) and a gas chromatograph column set to 50 °C. The cleaned sample gas was released at 65 °C from a second molecular sieve placed in front of a Thermo Fisher ™ MAT 253 gas source isotope ratio mass spectrometer (IRMS) into the sample bellow of the IRMS.

The accuracy and reproducibility of the O_2 extraction and cleaning protocols were verified by repeated analysis San Carlos Olivine grains. The oxygen isotopic compositions of all samples are normalized to the composition of San Carlos Olivine with $\delta^{18}O = 5.34$‰ (i.e., the average for San Carlos Olivine throughout the course of this study; n = 59) and $\Delta'^{17}O_{0.528} = -52$ ppm (Pack et al., 2016; Sharp et al., 2016; Wostbrock et al, 2020). To better assess the measurement accuracy for bioapatite, we also performed replicate analyses of AG-Lox as internal reference material. Data from LF line are presented in the form of $\delta^{17}O_{AP}$, $\delta^{18}O_{AP}$ and $\Delta'^{17}O_{AP}$.

2.4.3 Measurement of $\delta^{18}O$ of bioapatite phosphate oxygen by thermal combustion elemental analysis

Because oxygen isotopic fractionation during the heating of samples to 1,000 °C cannot be fully excluded, the phosphate fraction of the chemically pretreated tooth enamel was additionally precipitated to silver phosphate (Ag_3PO_4).

To assure the robustness of sample preheating prior to triple oxygen isotope analysis, we independently determined the $\delta^{18}O$ of the bioapatite phosphate fraction by means of thermal combustion elemental analysis (TC/EA). The phosphate group of chemically pretreated tooth enamel samples (see section 2.3) was separated and reprecipitated as Ag_3PO_4 according to the protocol of Dettman et al. (2001) (modified by Tütken et al. (2006)).

Firstly, 2 mg of pretreated tooth enamel powder was transferred into a 2 ml Eppendorf® tube (Eppendorf AG, Hamburg, Germany), placed on a vibrating table, and digested in 0.8 ml

hydrofluoric acid (HF, 2 M) for 12 h. The samples were centrifuged, and the remaining supernatant HF solution was separated from calcium fluoride precipitates (CaF_2). The HF solution was transferred into a new tube and was neutralized with ammonia solution (NH_4OH, 25%) by addition bromothymol blue (BTB) for pH indication. Subsequent addition of 0.8 ml silver nitrate ($AgNO_3$, 2 M) led to precipitation of Ag_3PO_4 crystals that were centrifuged to remove the supernatant solution containing excess $AgNO_3$. The Ag_3PO_4 precipitate was then rinsed five times with Milli-Q water and dried overnight at 70 °C.

Ag_3PO_4 aliquots of 300 μg were placed into silver capsules and analyzed by means of a TC/EA coupled via a ConFlo III (Thermo Finnigan) to a Micromass 100 GC-IRMS (Micromass UK Ltd, Manchester, United Kingdom) at the stable isotope center at the Faculty of Forest Sciences and Forest Ecology, University of Göttingen, Germany, according to the method of Vennemann et al. (2002). For untreated NBS 120c, we obtained $\delta^{18}O_{PO4}$ = 21.6 (n = 25, Feng et al., 2022). This value is indistinguishable from the initially reported $\delta^{18}O_{PO4}$ of 21.7‰ (Lécuyer et al., 1993) which has been confirmed in varying laboratories (Chenery et al., 2010). For AG-Lox, we obtained $\delta^{18}O_{PO4}$ = 20.5‰ (n = 28, Feng et al., 2022). Data from TC/EA are presented in the form of $\delta^{18}O_{PO4}$.

2.4.4   Combining laser fluorination $\Delta'^{17}O_{AP}$ with $\delta^{18}O_{PO4}$ from TC/EA

For the oxygen isotope composition of the phosphate fraction in bioapatite, we took the $\delta^{18}O_{PO4}$ from TC/EA analyses measured on silver phosphate and $\Delta'^{17}O_{AP}$ from the BrF_5 laser fluorination measured on bioapatite. This excludes the risk of biasing contributions to the measured $\delta^{18}O_{PO4}$ which could potentially originate from traces of structural carbonate and water in preheated and pre-fluorinated samples.

3   Results

3.1   Reference material AG-Lox

The AG-Lox $\delta^{18}O_{AP}$ and $\Delta'^{17}O_{AP}$ values from LF are shown in figure 1. Black circles are from Feng et al. (2022), black squares are from this study (Table 1). The overall mean $\delta^{18}O_{AP}$ and $\Delta'^{17}O_{AP}$ (Figure 1, black asterisk) derived from LF analyses are $\delta^{18}O_{AP}$ = 19.5 ± 0.6‰ and $\Delta'^{17}O_{AP}$ = −109 ± 8 ppm (n = 82). The former value is statistically indistinguishable from the respective TC/EA derived $\delta^{18}O_{PO4}$ value of 20.5‰ (Feng et al., 2022). The uncertainties of the difference values are ±0.6‰ for $\delta^{18}O_{AP}$ and ± 8 ppm for $\Delta'^{17}O_{AP}$. We use these external errors as uncertainties of bioapatite LF analyses. On average, the $\delta^{18}O_{AP}$ value from LF is

~1‰ lower than the $\delta^{18}O_{PO4}$ from TC/EA. However, it is noteworthy that a potential oxygen fractionation during LF would not affect $\Delta'^{17}O_{AP}$ significantly if one assumes that a given oxygen fractionation is (close to) identical for both ^{17}O and ^{18}O (i.e. Eq. 5). The analytical intervals of AG-Lox (Feng et al., 2022) and sample analysis (this study) are identical.

Table 1: Triple oxygen isotope data of AG-Lox from Laser fluorination.

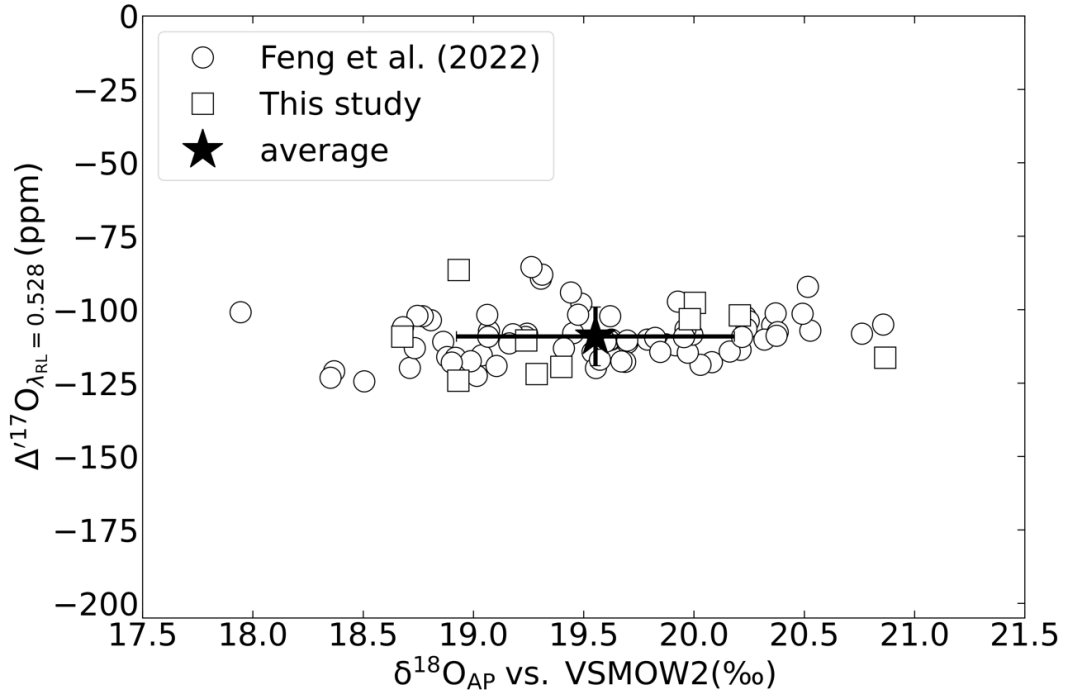| ID	$\delta^{18}O_{AP}$ (‰)	$\delta^{17}O_{AP}$ (‰)	$\Delta'^{17}O_{AP}$ (ppm)
Slope			0.528
8591	18.933	9.865	-87
8610	18.677	9.708	-109
8628	20.004	10.414	-98
8620	19.239	10.001	-110
8836	19.980	10.396	-103
8876	18.931	9.826	-124
8898	19.286	10.014	-122
8896	20.208	10.516	-102
8929	19.399	10.075	-119
8947	20.867	10.846	-116

Figure 1: The $\delta^{18}O_{AP}$ and $\Delta'^{17}O_{AP}$ data of the AG-Lox from laser fluorination. The black circles are from Feng et al. (2022). The black squares are from this study. The black asterisk is the overall average. The error bars (black lines) indicate 1σ standard deviations.

3.2 Terrestrial mammals

The land-living mammals' oxygen isotope data are listed in Appendix S1.

3.2.1 Carbon and oxygen isotope composition from carbonate

Figure 3 shows $\delta^{13}C$ and $\delta^{18}O_{CO3}$ of the carbonate group of all samples. The African antelope data plots in two groups: *i*) $\delta^{13}C$ = -0.90 to 2.64‰ and $\delta^{18}O_{CO3}$ = 30.45 to 34.49‰ (Figure 2, dark orange octagons) and *ii*) $\delta^{13}C$ = -14.77 to -9.6 ‰ and $\delta^{18}O_{CO3}$ = 27.64 to 36.85 ‰ (Figure 2, dark orange diamonds). For the Australian *Diprotodontia* and *Sarcophilus* (Figure 2, narrow green diamonds), $\delta^{13}C$ ranges from -18.41 to -6.32‰ and $\delta^{18}O_{CO3}$ ranges from 24.67 to 30.92‰. For the North American *Didelphis* and *Didelphis virginiana* (Figure 2, purple triangle left), $\delta^{13}C$ are -12.29‰ and -12.54‰ and $\delta^{18}O_{CO3}$ are 27.31‰ and 24.70‰ respectively. The South American *Procyon cancrivorus* (Figure 2, light blue triangle right) plots at $\delta^{13}C$ = -12.52‰ and $\delta^{18}O_{CO3}$ = 26.20‰. For the mammals from Germany/Central Europe, the $\delta^{13}C$ and $\delta^{18}O_{CO3}$ ranges from -17.98 to -9.64‰ and 21.13 to 27.95‰, respectively.

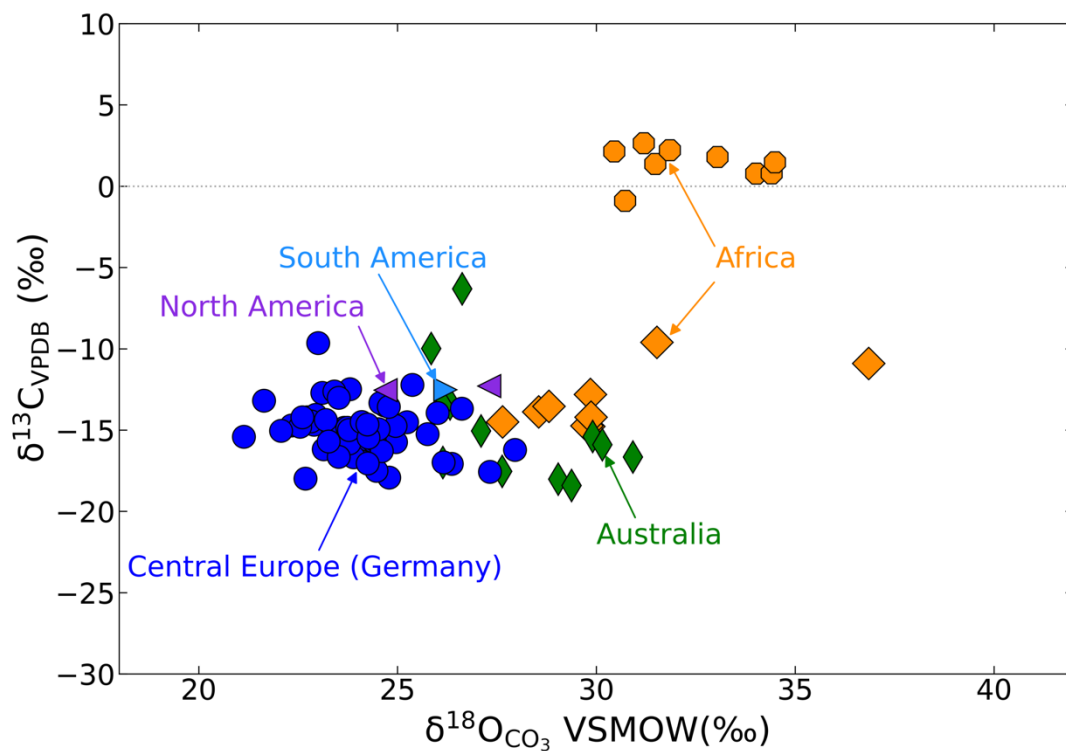Figure 2: The bioapatite $\delta^{18}O_{CO3}$ and $\delta^{13}C$ as measured by a KIEL IV Carbonate Device. Dark orange octagons and diamonds: African mammals, narrow green diamond: Australian mammals, purple triangles pointing left: North American mammals, light blue triangle

pointing right: South American mammal, and blue points: Central European mammals (Germany).

3.2.2   Triple oxygen isotope composition from phosphate

Figure 3 shows the $\delta^{18}O_{PO4}$ and $\Delta'^{17}O_{AP}$ sample data. For African mammals (Figure 3, dark orange octagons and diamonds), $\delta^{18}O_{PO4}$ ranges from 17.9 to 28.0‰ and $\Delta'^{17}O_{AP}$ ranges from -223 to -109 ppm. For Australian *Diprotodontia* and *Sarcophilus* (Figure 3, green thin-diamonds), $\delta^{18}O_{PO4}$ ranges from 15.5 to 20.7‰ and $\Delta'^{17}O_{AP}$ ranges from -191 to -117 ppm. For North American *Didelphis* and *Didelphis virginiana* (Figure 3, purple triangle left), the $\delta^{18}O_{PO4}$ is 17.9‰ and 15.2‰ and the $\Delta'^{17}O_{AP}$ is -130 ppm and -113 ppm respectively. For South American *Procyon cancrivorus* (Figure 3, light blue triangle right), the $\delta^{18}O_{PO4}$ equals to 15.6‰ and the $\Delta'^{17}O_{AP}$ equals to -137 ppm. For the Central European/German mammals, $\delta^{18}O_{PO4}$ ranges from 6.8 to 18.8‰ and $\Delta'^{17}O_{AP}$ ranges from -250 to -85 ppm.
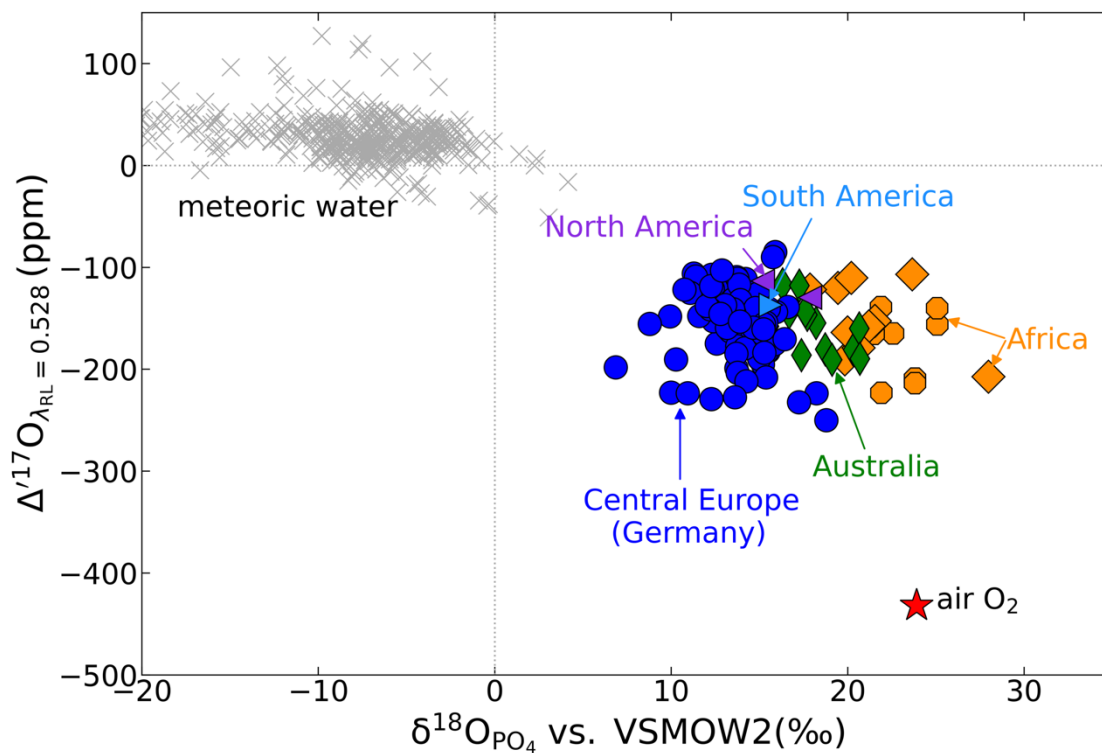
Figure 3: Overview on the bioapatite $\delta^{18}O_{PO4}$ and $\Delta'^{17}O_{AP}$ data. Dark orange octagons and diamonds: African mammals, yellow diamonds: AG-Lox, green narrow-diamonds: Australian mammals, purple triangles pointing left: North American mammals, light blue triangles pointing right: South American mammal, blue points: Central European/German mammals, blue crosses: meteoric water, and red asterisk: modern air (Pack, 2021).

Figure 4 shows the $\delta^{18}O_{PO4}$ and $\Delta'^{17}O_{AP}$ data of the same species. For Australian *Macropodidae* (Figure 4 A), the $\delta^{18}O_{PO4}$ range from 17.3 to 18.2‰ and the $\Delta'^{17}O_{AP}$ range from -155 to -118 ppm. For *Capreolus capreolus* from Central Europe (Germany), the $\delta^{18}O_{PO4}$ ranges from 11.4 to 16.6‰ and the $\Delta'^{17}O_{AP}$ ranges from -183 to -85 ppm (Figure 4 B). For *Sus scrofa* (Figure 4 C), the $\delta^{18}O_{PO4}$ ranges from 12.6 to 15.1‰ and the $\Delta'^{17}O_{AP}$ ranges from -175 to -117 ppm. For *Meles meles* (Figure 4 D), the $\delta^{18}O_{PO4}$ ranges from 13.3 to 15.4‰ and the $\Delta'^{17}O_{AP}$ ranges from -163 to -132 ppm. For *Vulpes vulpes* (Figure 4 E), the $\delta^{18}O_{PO4}$ ranges from 13.4 to 15.2‰ and the $\Delta'^{17}O_{AP}$ ranges from -177 to -144 ppm. For *Talpa europaea* (Figure 4 F), the $\delta^{18}O_{PO4}$ ranges from 11.1 to 14.6‰ and the $\Delta'^{17}O_{AP}$ ranges from -159 to -125 ppm.
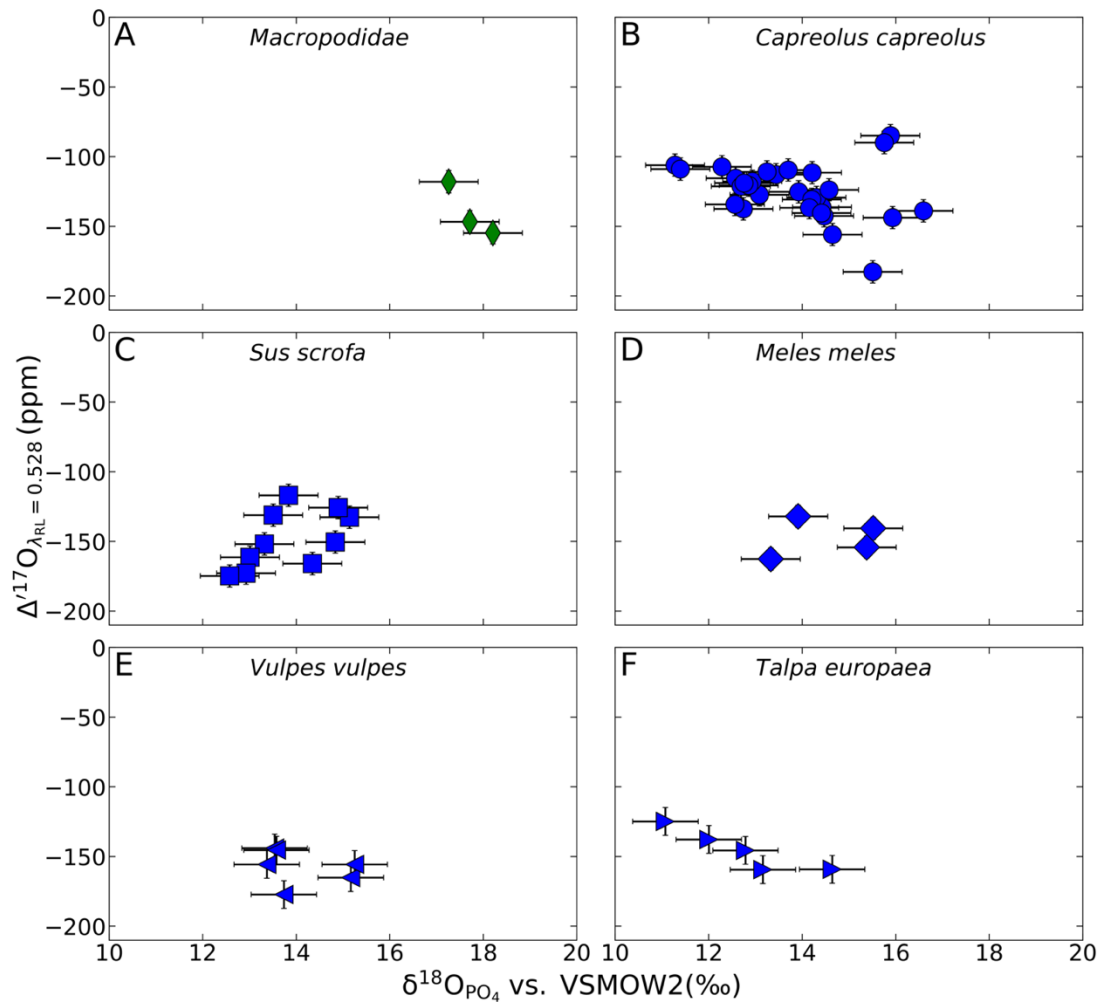

Figure 4: The bioapatite $\delta^{18}O_{PO4}$ and $\Delta'^{17}O_{AP}$ data of different mammalian taxa. A: *Macropodidae* from Australia. B: *Capreolus capreolus*. C: *Sus scrofa*. D: *Meles meles*. E: *Vulpes vulpes*. F: *Talpa europaea*. B, C, D, E and F are all from central Europe/Germany.

4 Oxygen mass balance model for terrestrial mammals

4.1 Basic equations

Based on the approach of Bryant and Froelich (1995), Pack et al. (2013) developed an oxygen mass balance model for $\Delta'^{17}O$ of terrestrial mammalian bioapatite to demonstrate the quantitative relation between $\Delta'^{17}O$ of inhaled air O_2, body mass M_b, and $\Delta'^{17}O$ in tooth enamel. On the basis of the models developed by Bryant and Froelich (1995), Kohn (1996), and Pack et al. (2013), Feng et al. (2022) presented a refined oxygen mass balance model for marine vertebrates which, herein, is adapted to terrestrial mammals (*e.g.* Figure 5 and 6) as described in the following.

In steady state, the isotope composition of a specimen's body water (BW) is given by:

$$\sum \frac{\delta^k O_i^{in} \times F_i^{in}}{\sum F_i^{in}} + \sum \frac{\delta^k O_j^{out} \times F_j^{out}}{\sum F_j^{out}} = 0 \qquad \text{Eq. 9}$$

k represents isotopes with the masses 17 and 18, with $\sum F_i^{in} + \sum F_j^{out} = 0$ with oxygen influxes (F_i^{in}) > 0 and outfluxes (F_j^{out}) < 0. The respective $\Delta'^{17}O_{BW}$ is then calculated from $\delta^{17}O_{BW}$ and $\delta^{18}O_{BW}$ (Eq. 5).

Specific $\delta^{17}O$ and $\delta^{18}O$ are assigned to the individual in and outfluxes. For F_i^{out}, oxygen isotope fractionation between outflux and body water ($\delta^{17}O_{BW}$, $\delta^{18}O_{BW}$) is considered. The $\delta^{18}O$ of the outflux is given by the fractionation factor $^k\alpha$ with $\delta^{18}O_j = {^{18}\alpha_{j\text{-BW}}} \times (\delta^{18}O_{BW} + 1000) - 1000$ and $\delta^{17}O_j = {^{17}\alpha_{j\text{-BW}}}^{\theta j\text{-BW}} \times (\delta^{17}O_{BW} + 1000) - 1000$.

For land-living mammals, the principal F_i^{in} are inhaled air O_2 (F_A), drinking water (F_{DW}), atmospheric vapor (F_{AV}), water from food (F_{FW}), and oxygen bound in organic food compounds (F_F). General F_j^{out} are water vapor through exhaled breath (F_{BR}), exhaled CO_2 (F_{CO2}), transcutaneous water vapor (F_{TR}), and liquid water in urine, feces, and sweat (F_{LW}). All fluxes are given in mol O day^{-1} and body masses (M_b) are given in kg. For illustration of the mass balance model calculation, we refer to a roe deer (*Capreolus capreolus*) from Germany with $10 \leq M_b \leq 15.5$ kg (König et al., 2020) (Figure 5).
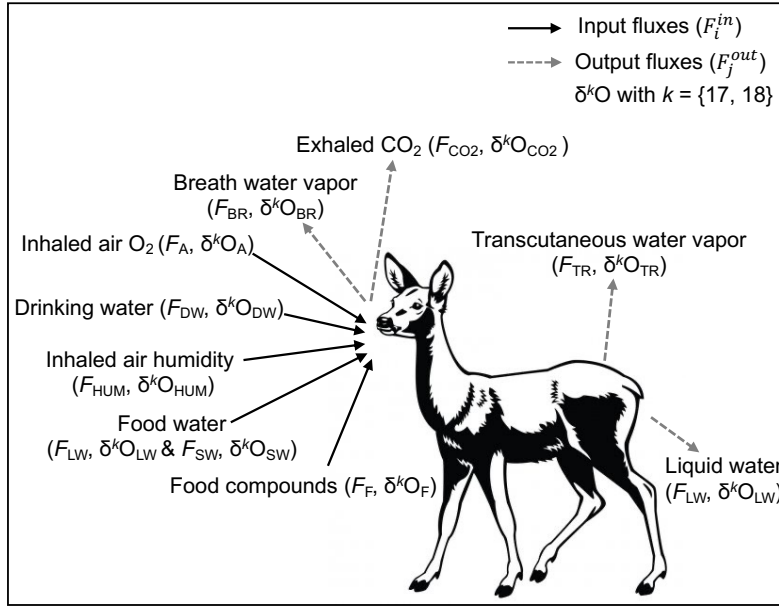
Figure 5: Illustration of the parameters considered in the mass balance model.

4.2   Fluxes

4.2.1   Influxes

4.2.1.1   Inhaled oxygen (F_A)

The energy consumption E of roe deer varies between 5,000 to 17,000 kJ day^{-1} (König et al., 2020; Wallach et al., 2007; Onderscheka, 1999). O_2 is required as an oxidant for metabolic energy production, hence, the amount of required O_2 from air (F_A) is directly linked to energy consumption (E):

$$F_A = 2\, E\, k_{oc}$$
<div align="right">Eq. 10</div>

where k_{oc} being the oxygen conversion factor of 2.16×10^{-3} mole kJ^{-1} (Kohn, 1996), resulting in $22 \leq F_A \leq 73$ mol O day^{-1}.

4.2.1.2   Drinking water (F_{DW})

The flux of drinking water has been calculated from experimental data for Mediterranean roe deer habitats and ranges from 1.6 to 2.0 L day^{-1} (Wallach et al., 2007). However, seasonal data, along with information on precipitation and temperature, indicate, that the F_{DW} must be

lower for the Central European roe deer presented in this study (*ca.* 0.83 ± 0.13 L day^{-1} in spring), which equals 46 ± 7 mol O day^{-1}.

4.2.1.3 Inhaled air humidity (F_{HUM})

Inhaled F_{HUM} consists of atmospheric water vapor and its calculation requires knowledge of the total volume of consumed air V_{air} per day, as well as ambient relative humidity (*RH*). The value of V_{air} can be approximated from F_A. For lungs, the oxygen utilization fraction X is *ca.* 0.2 (Epstein and Zeiri, 1988). Hence, V_{air} through the lung can be defined by Eq. 11 as follows:

$$V_{air} = 0.5 \, F_A \, 22.4 \text{ L mol}^{-1} \times \text{X}^{-1} \times 0.21^{-1} \qquad \text{Eq. 11}$$

The factor of 0.21 is the O_2 mixing ratio in air. The saturation vapor content (V_C) is given by $V_C = 5.018 + 0.32321 \, t + 8.1847 \times 10^{-3} \, t^2 + 3.1243 \times 10^{-4} \, t^3$ g m^{-3} (40 °C $\geq t \geq$ 0 °C) (Nave, 2000). The resultant flux F_{HUM} of inhaled vapor from humidity into the lungs is:

$$F_{HUM} = RH \times V_C \, / 1000 \text{ g L}^{-1} \times V_{air} \, / \, (18.02 \text{ g mol}^{-1}) \qquad \text{Eq. 12}$$

The modern relative humidity (*RH*) in Germany equals 0.72 ± 0.10 (Deutscher Wetterdienst, Germany) at $t = 8$ °C (Umwelt Bundesamt, Germany; mean annual temperature). The resulting F_{HUM} into the lungs is $2 \leq F_{HUM} \leq 7$ mol O day^{-1}.

4.2.1.4 Water from food (F_{FW})

The fluxes F_{FW} (food water) and F_F (oxygen in, e.g. ingested carbohydrates and other food nutrition) are both obtained from food. Here, we need to consider the digestibility (d_{digest}, dimensionless, varies between 0 and 1) and energy extraction efficiency (e_{eff}, dimensionless). d_{digest} is the fraction of nutrients used from ingested food and e_{eff} is the ratio of ingested energy E to the total energy E_{food} (given in kJ $\times$ kg^{-1} of dry mass) included in the food. In the case of a herbivore diet, the digestibility is $d_{digest} = 0.7 \pm 0.2$ and the energy extraction efficiency is $e_{eff} = 0.9 \pm 0.1$ (Kohn, 1996). The oxygen in food can be divided into moisture (80% wt.) and oxygen bound in organic molecules (20% wt.). The flux F_{FW} of moisture (water) from food is calculated:

$$F_{FW} = E \, E_{food}^{-1} \, d_{digest}^{-1} \, e_{eff}^{-1} \, 0.8 \times 1000 \, / \, 18.02 \qquad \text{Eq. 13}$$

For the roe deer, the flux of water from food is $13 \leq F_{FW} \leq 266$ mol O day^{-1} with $17{,}000 \leq E_{food} \leq 21{,}000$ kJ kg^{-1} for plants (McKendry, 2002). Food water consists of leaf water (F_{LW}) and stem water (F_{SW}). We assumed that f varies between 0% and 100% with leaf water F_{LW} = f $\times$ F_{FW} and stem water F_{SW} = (1-f) $\times$ F_{FW}.

4.2.1.5 Oxygen-bearing organic food compounds (F_F)

The flux F_F refers to oxygen that was organically bound oxygen in food hence, knowledge of the food's composition is required to estimate F_F. For herbivores, the protein in dry food is usually around 15wt.%, fat amounts for about 5wt.%, and carbohydrates contribute with 80wt.% (Cheung, 2015). According to the respective mole fractions, oxygen comprises 36 mol% in protein (CH_3CHNH_2COOH), 12 mol% in fat ($CH_3(CH_2)_{14}COOH$), and 53 mol% in carbohydrate ($C_6H_{12}O_6$):

$$F_F = E\, E_{food}^{-1} \times (0.15 \times 0.36 + 0.05 \times 0.12 + 0.8 \times 0.53) \times 1000/15.999 \qquad \text{Eq. 14}$$

For the roe deer, F_F is $7 \leq F_F \leq 30$ mol O day^{-1}.

4.2.2 Outfluxes

4.2.2.1 Exhaled breath vapor (F_{BR})

The flux F_{BR} is the vapor in exhaled breath and proportional to the volume V_{air} of inhaled air. The exhaled breath is vapor-saturated ($RH = 100\%$) at 37°C and contains 44.0 g m^{-3}.

$$F_{BR} = F_{HUM} - 44.0/(1000 \text{ g L}^{-1}) \times V_{air} / (18.02 \text{ g/mol}) \qquad \text{Eq. 15}$$

For the roe deer, the outflux of breath vapor is $-12 \geq F_{BR} \geq -42$ mol O day^{-1}.

4.2.2.2 Exhaled CO_2 (F_{CO2})

The outflux F_{CO2} is related to the F_A and the respiratory quotient R_q (exhaled CO_2 / O_2 ratio). For the roe deer's diet, R_q is taken as 0.9 in the net oxidation of carbohydrate, fat, and protein (Bryant and Froelich, 1995):

$$F_{CO2} = -R_q\, F_A \qquad \text{Eq. 16}$$

For the roe deer, the flux F_{CO2} is $-19 \geq F_{CO2} \geq -66$ mol O day^{-1}.

4.2.2.3 Transcutaneous water vapor (F_{TR})

The transcutaneous water flux F_{TR} is taken from Kohn (1996) according to Eq. 17:

$$F_{TR} = -1.44 \text{ mol O day}^{-1} \, M_b^{2/3} \qquad \text{Eq. 17}$$

For the roe deer, the flux F_{TR} is approximately $-14 \geq F_{CO2} \geq -9$ mol O day^{-1}.

4.2.2.4 Liquid water (F_{LW})

The flux of liquid water in urine and excrements (F_{LW}; Lifson and McClintock, 1966; Schoeller et al., 1986; Wong et al., 1988) is calculated from the sum of all other water fluxes to fulfil the steady state requirement (Eq. 18) as illustrated in the fluxes flow model (Figure 6).

$$F_{LW} = -(F_A + F_{DW} + F_{HUM} + F_{FW} + F_F) - F_{CO2} - F_{BR} - F_{TR} \qquad \text{Eq. 18}$$

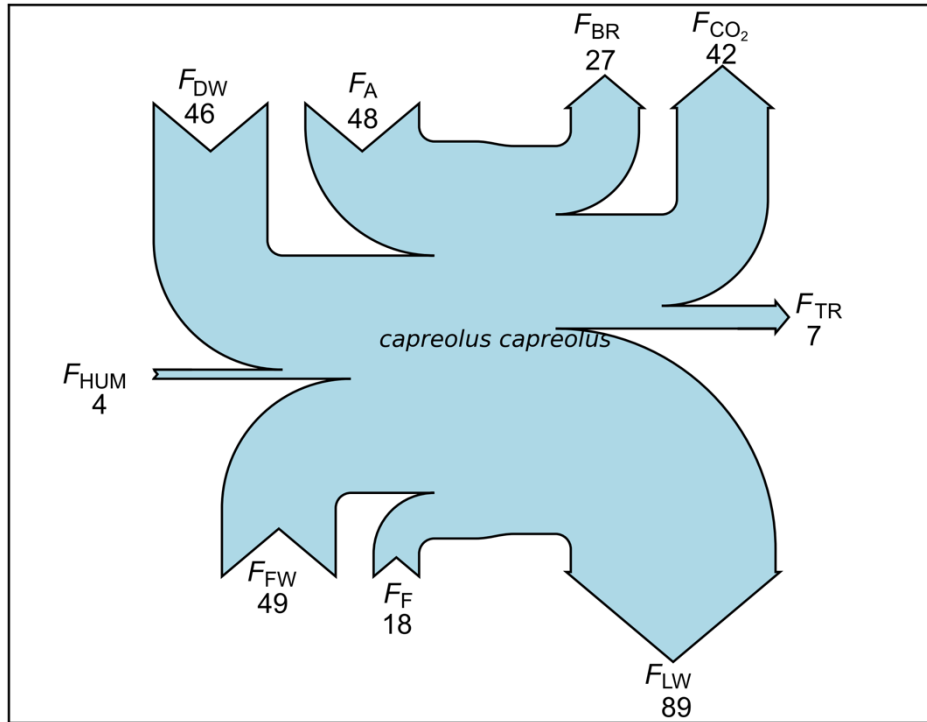For the roe deer, F_{LW} is calculated to be $-37 \geq F_{LW} \geq -314$ mol O day^{-1}.

Figure 6: The input and output fluxes for a roe deer (*Capreolus capreolus*) in a steady state. All values are reported with average values in mol O day^{-1}. Predominant influxes are in equal shares F_A, F_{DW}, and F_{FW}, which are mostly balanced by F_{LW} and F_{CO2}.

4.3 Isotopic compositions

The calculation of body water $\delta^{18}O$ and $\Delta'^{17}O$ requires accurate constraints on the isotopic composition of the respective fluxes (Eq. 9). For the influxes, these values are obtained from the literature. The isotopic compositions of outfluxes are then calculated from the body water (BW) and the associated fractionation factors (α) and fractionation exponents (θ) between BW and outflux. All oxygen fractionation processes between respective fluxes and BW occur at a body temperature of 37 ±1 °C.

4.3.1 Influxes isotope composition

4.3.1.1 Inhaled oxygen

The isotope composition of F_A ($\delta^{18}O_A$, $\Delta'^{17}O_A$) depends on the oxygen isotopic composition of air O_2 and taxon specific respiratory fractionation. The mean composition of modern air O_2 is $\delta^{18}O_{air} = 23.9 \pm 0.3‰$ and $\Delta'^{17}O_{air} = -432 \pm 15$ ppm (Pack, 2021). For terrestrial mammals, the isotopic composition of respired O_2 ($\delta^{18}O_A$) is below the ambient $\delta^{18}O_{air}$ due to preferential diffusive uptake of isotopically depleted O_2 (Epstein and Zeiri, 1988). Diffusive fractionation of inhaled O_2 is approximately $\Delta\delta^{18}O_{A\text{-}air} = -8.9 \pm 2‰$ (Kohn, 1996; Pack et al., 2013). The resulting $\delta^{18}O_A = \delta^{18}O_{air} + \Delta\delta^{18}O_{A\text{-}air} = 15 \pm 2‰$. In order to calculate the respective $\Delta'^{17}O_A$, $\theta_{A\text{-}air}$ of 0.5179 ± 0.0006 was used (Luz and Barkan, 2005) as a universal value for mammals. We therefore obtain $\Delta'^{17}O_A = \Delta'^{17}O_{air} + (\theta_{A\text{-}Air} - 0.528) \times \Delta\delta^{18}O_{A\text{-}air} = -0.342 \pm 0.026$ ‰.

4.3.1.2 Drinking water

The drinking water (F_{DW}) composition is considered to represent local meteoric water ($\delta^{18}O_{DW}$, $\Delta'^{17}O_{DW}$) which varies with locality, climate, and environment (Dansgaard, 1964; Gat 1996, Gat et al. 2001). For roe deer from Germany, we took $\delta^{18}O_{DW} = -8 \pm 2‰$ (Bowen and Revenaugh, 2003; Bowen, 2018) and $\Delta'^{17}O_{DW} = 0.022 \pm 0.005‰$, a value that can be considered as representative for average Central European precipitation and water bodies (Luz and Barkan, 2010; Affolter et al., 2015; Leuenberger and Ranjan, 2021).

4.3.1.3 Inhaled air humidity

For the atmospheric water vapor composition, we used regional oxygen isotope values of atmospheric water vapor ($\delta^{18}O_{HUM}$, $\Delta'^{17}O_{HUM}$) as for example from Central Europe in case of the roe deer. (Surma et al., 2021); $\delta^{18}O_{HUM} = -18 \pm 5‰$, $\Delta'^{17}O_{HUM} = 0.022 \pm 0.010‰$).

4.3.1.4 Water from food

Kohn (1996) presented that leaf water F_{LW} in food is enriched by 6.5‰ in $\delta^{18}O_{LW}$ relative to local meteoric water. Landais et al. (2006) then measured leaf water in Germany with $\delta^{18}O_{LW}$ = 5.6 ± 4.3‰ and $\Delta'^{17}O_{LW}$ = -0.102 ± 0.048‰ in average. For stem food water F_{SW}, there is no fractionation relative to local meteoric water (Yakir, 1992; Landais et al., 2006). Hence, $\delta^{18}O_{SW} = \delta^{18}O_{DW}$ = -8 ± 2‰ and $\Delta'^{17}O_{SW} = \Delta'^{17}O_{DW}$ = 0.022 ± 0.005‰.

4.3.1.5 Organic food compounds

For herbivores, $\delta^{18}O$ in organic food compounds ($\delta^{18}O_F$) can be approximated from the isotope composition of cellulose, which is 27‰ higher than the $\delta^{18}O_{LW}$ of leaf water (Sternberg, 1989). The leave cellulose and stem cellulose have the same fractionation relative to leaf water (Burk and Stuiver, 1981; Edwards et al., 1985; Yakir, 1992). Pack et al. (2013) estimated an uncertainty of ± 10‰ for $\delta^{18}O$ and an associated equilibrium fractionation $\theta_{F\text{-}LW}$ value 0.5275. We assume an uncertainty 0.0005 for $\theta_{F\text{-}LW}$. This can be summarized as $\delta^{18}O_F = \delta^{18}O_{LW} + (27 \pm 10‰)$ and $\Delta'^{17}O_F = \Delta'^{17}O_{LW} + (\theta_{F\text{-}LW} - 0.528) \times (27 \pm 10‰)$. The respective values of roe deer are $\delta^{18}O_F = (5.6 \pm 4.3‰) + (27 \pm 10‰) = 25.6 \pm 11‰$ and the $\Delta'^{17}O_F = (-0.102 \pm 0.048‰) + (0.5275 \pm 0.0005 - 0.528) \times (27 \pm 10‰) = -0.125 \pm 0.028‰$.

4.3.2 Outfluxes isotope compositions

4.3.2.1 Exhaled breath vapor

The $\delta^{18}O$ of the exhaled water vapor F_{BR} equilibrates with body water with $\Delta\delta^{18}O_{BR\text{–}BW} = -8.44‰$ (Horita and Wesolowski, 1994) with an estimated uncertainty of ± 2‰. Hence, the fractionation factor for vapor-water equilibrium equals $^{18}\alpha_{BR\text{-}BW} = 0.992 \pm 0.002$, which gives $\delta^{18}O_{BR} = 0.992 \pm 0.002 \times (\delta^{18}O_{BW} + 1000) - 1000$. Combining $\delta^{18}O_{BR}$ with the associated $\theta_{BR\text{-}BW}$ of 0.529 ± 0.001 (Barkan and Luz, 2005), gives $\delta^{17}O_{BR} = (0.992 \pm 0.002)^{0.529 \pm 0.001} \times (\delta^{17}O_{BW} + 1000) - 1000$.

4.3.2.2 Exhaled CO₂

The $\delta^{18}O$ fractionation between respired CO_2 and body water is adopted from Brenninkmeijer et al. (1983) with the fractionation factor $^{18}\alpha_{CO2\text{-}BW} = 1.0396 \pm 0.0001$ at 37 °C, which gives $\delta^{18}O_{CO2} = 1.0396 \pm 0.0001 \times (\delta^{18}O_{BW} + 1000) - 1000$. The associated theoretical $\theta_{CO2\text{-}BW}$ of 0.5246 is derived from Guo and Zhou (2019). The resulting $\delta^{17}O_{CO2}$ is defined as $\delta^{17}O_{CO2} = (1.0396 \pm 0.0001)^{0.5246} \times (\delta^{17}O_{BW} + 1000) - 1000$.

4.3.2.3 Transcutaneous water vapor

F_{TR} originates from body water with an offset of $\Delta\delta^{18}O_{TR-BW} = -19‰$ (Bryant and Froelich, 1995) and an estimated uncertainty of $\pm 5‰$ (Pack et al. 2013). Hence, the fractionation factor is $^{18}\alpha_{TR\text{-}BW} = 0.9815 \pm 0.0049$, which gives $\delta^{18}O_{TR} = 0.9815 \pm 0.0049 \times (\delta^{18}O_{BW} + 1000) - 1000$. The associated θ_{TR-BW} of 0.516 ± 0.002 is adopted from Landais et al. (2006) for $Rh = 0.72 \pm 0.05$ for German roe deer. Hence, $\delta^{17}O_{TR} = (0.9815 \pm 0.0049)^{0.516 \pm 0.002} \times (\delta^{17}O_{BW} + 1000) - 1000$.

4.3.2.4 Liquid water

F_{LW} is not fractionated relative to body water (Bryant and Froelich, 1995; Lifson and McClintock, 1966; Schoeller et al., 1986; Wong et al., 1988) which leads to $\delta^{18}O_{LW} = \delta^{18}O_{BW}$ and $\delta^{17}O_{LW} = \delta^{17}O_{BW}$.

4.3.2.5 Fractionation between tooth bioapatite and body water

Bioapatite (AP) is assumed to mineralize in isotope equilibrium with body water (BW). The temperature dependent fractionation factors for the apatite-water fractionation ($^{17}\alpha_{\text{apatite-water}}$, $^{18}\alpha_{\text{apatite-water}}$) are adopted from (Hayles et al., 2018).

$$\delta^k O_{AP} = {}^k\alpha_{\text{apatite-water}}\,(T) \times (\delta^k O_{BW} + 1000) - 1000 \qquad \text{Eq. 19}$$

The results from the oxygen mass balance model for the German/Central European roe deer agree with the experimental tooth enamel values as they both result in identical $\Delta'^{17}O$ and $\delta^{18}O_{PO4}$ data (Figure 7). The model uncertainties are calculated by error propagation by Monte Carlo simulation of the individual parameters with normal or continuous uniform distribution in the given range.
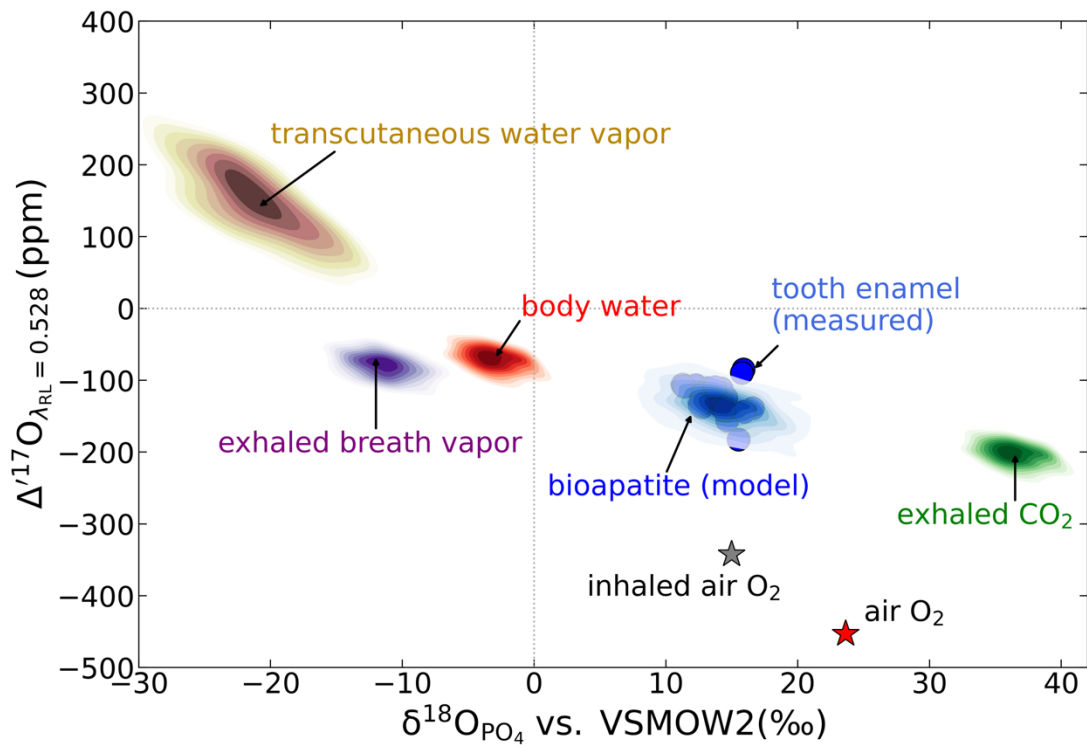
Figure 7: Comparison of $\delta^{18}O_{PO4}$ vs. $\Delta'^{17}O$ calculated with the mass balance model (Chapter 4) and measured data from roe deer (*Capreolus capreolus*) tooth enamel. Red star: modern air O_2, grey star: inhaled air O_2 for terrestrial mammals, blue points: measured tooth enamel data, green diffuse area: exhaled CO_2, purple diffuse area: breath water vapor, brown diffuse area: transcutaneous water vapor, red diffuse area: modelled body water, and blue diffuse area: modelled bioapatite tooth enamel.

4.4 Other terrestrial mammals

The approach for calculating drinking water and leaf water for terrestrial mammals with fragmentary location data is exemplified with *Oryx gazella*. Figure 8 A shows the natural habitat of *Oryx gazella* which is then used to integrate over the local precipitation water $\delta^{18}O$ (Figure 8 B) which ranges from -5.9 to -0.7‰.
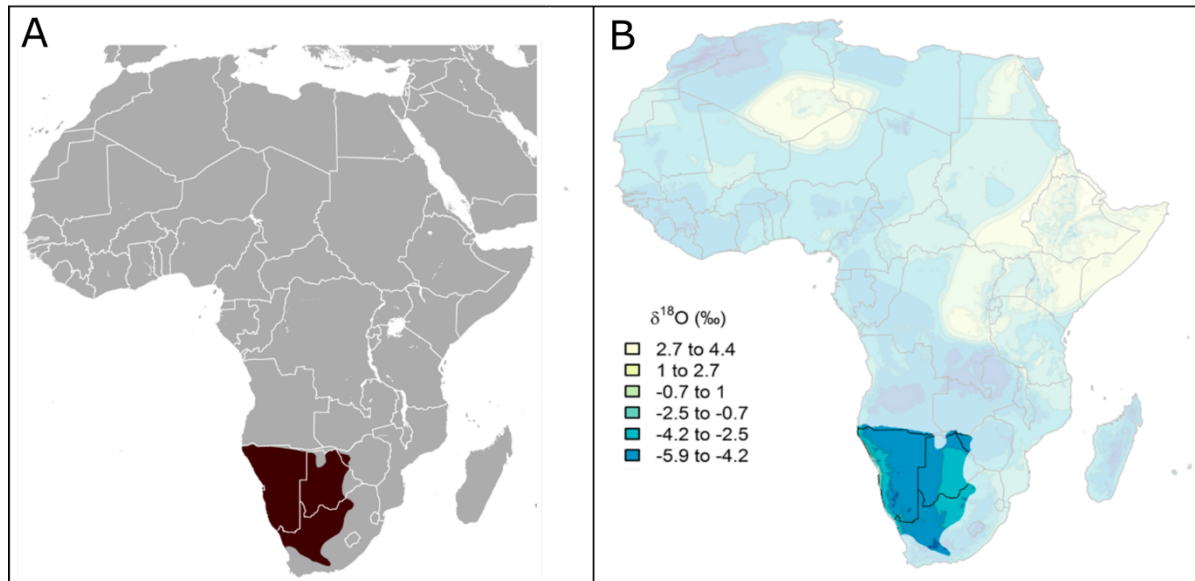
Figure 8. A: Natural habitat of *Oryx gazella* (*IUCN, 2015*). B: The $\delta^{18}O$ of local surface water (Waterisotopes.org).

Water uptake from drinking water is a significant influx of the body water mass balance (references). However, the coverage of available triple oxygen isotope records of rain and surface water is comparably small (Aron et al., 2021; Surma et al., 2021).

In order to approximate an average global $\Delta'^{17}O$ vs. $\delta^{18}O$ relationship for surface waters, we compiled global surface water data from 21 studies (Landais et al., 2006, 2010; Luz and Barkan, 2010; Affolter et al., 2015; Alexandre et al., 2019; Aron et al., 2021; Bergel et al., 2020; Bershaw et al., 2020; Evans et al., 2018; Gázquez et al., 2018; Li et al., 2015, 2017; Lin et al., 2013; Passey and Ji, 2019; Sha et al., 2020; Surma et al., 2015, 2018; Tian et al., 2019, 2018; Uechi and Uemura, 2019; Voigt et al., 2021). Precipitation samples from polar and high alpine areas were excluded from the model by choosing $\delta^{18}O = -15‰$ as the lower threshold value. We also excluded waters with $\delta^{18}O$ higher than 5‰, since those are typically characterized by elevated salinity (e.g. Surma et al., 2018; Voigt et al., 2021).

Triple oxygen isotope data of plants are available from work on leaf and stem water from Europe and field experiments in Israel (Landais et al., 2006), leaf and stem water from Kenya (Li et al., 2017), as well as grass leaf water from controlled growth chamber experiments (Alexandre et al., 2019). Compiled leaf and stem water data are shown in Figure 9 along with meteoric (drinking) water.
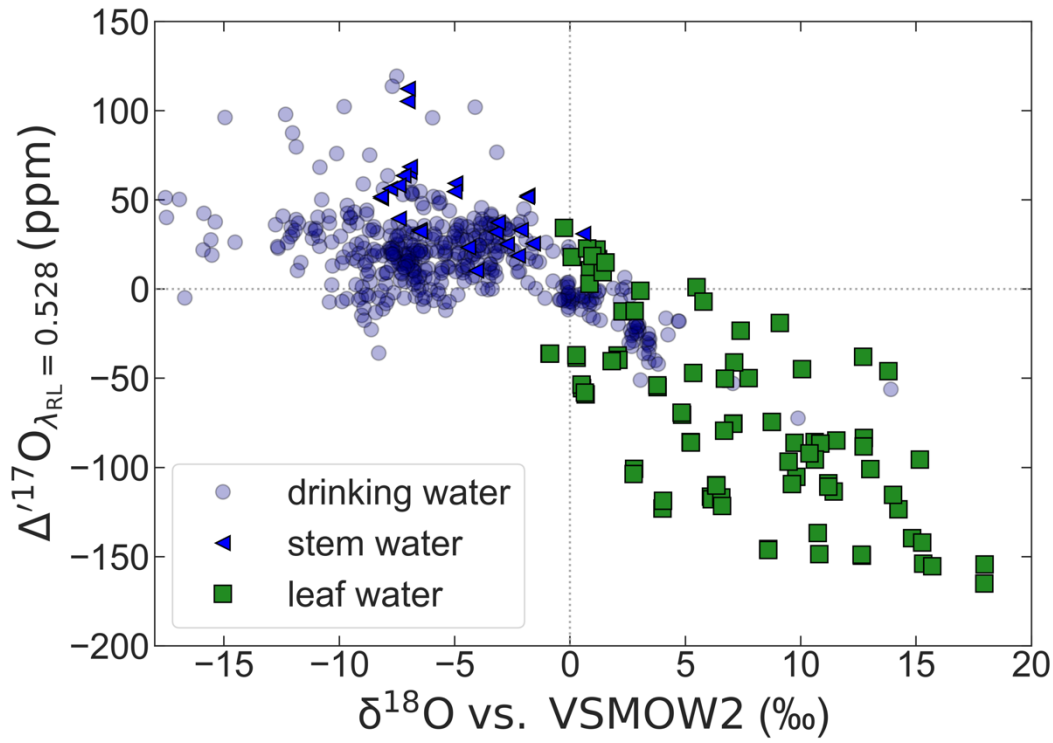
Figure 9: The $\delta^{18}O$ and $\Delta'^{17}O$ of drinking water (light-blue circles), stem water (blue triangles pointing left), and leaf water (green squares) from literatures. The data are derived from Landais et al. (2006), Li et al. (2017), and Alexandre et al. (2019).

The fractionation between leaf water and local meteoric and stem water (Figure 10) is inversely proportional to relative humidity and larger when compared to Kohn (1996). The average fractionation between leaf water and local meteoric water in Germany is $13.6 \pm 4.3‰$ as shown in chapter 4.2. For *Oryx gazella* with $RH = 0.4 \pm 0.05$, the average fractionation between leaf water and drinking water is 17.1‰. Hence the $\delta^{18}O_{LW}$ for *Oryx gazella* ranges from 11.9 to 16.4‰.
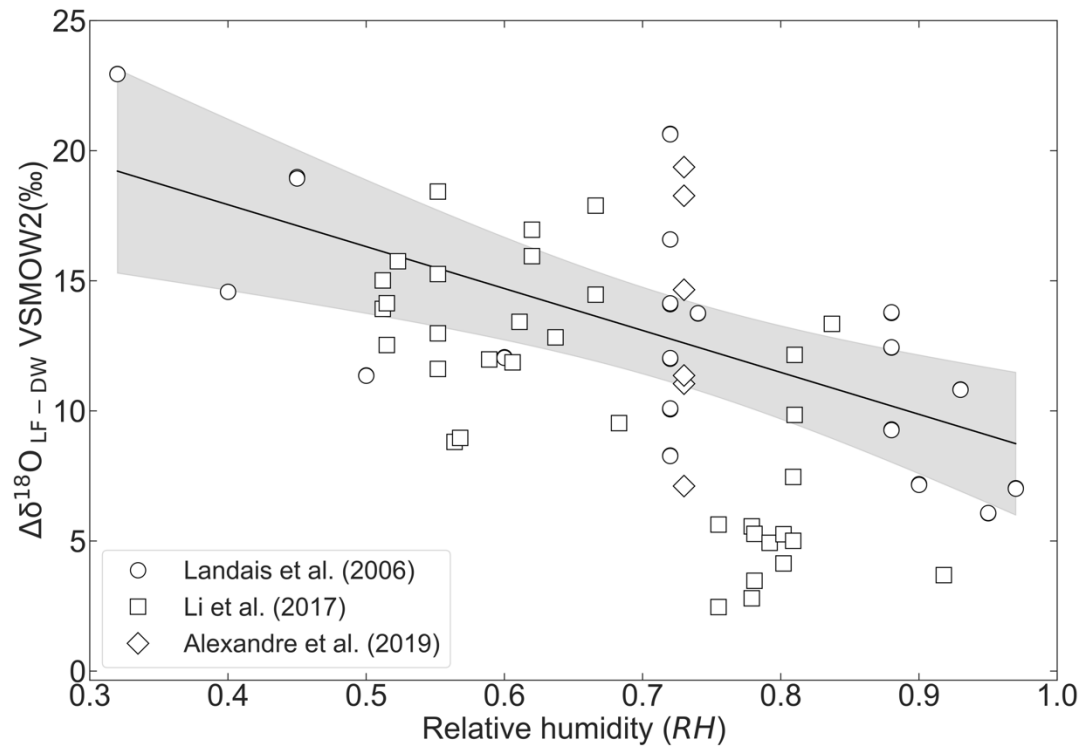
Figure 10: $\delta^{18}O$ fractionation between leaf water and drinking water (stem water). White circles: Data from Landais et al. (2006). White squares: Data from Li et al. (2017). White diamonds: Data from Alexandre et al., 2019.

We take the -5.9 to -0.7‰ of $\delta^{18}O_{DW}$ and the related fractionation (17.1‰) between leaf water and drinking water and integrated these values into the dataset showed in Figure 11. Under consideration of the respective uncertainties, we calculated the $\Delta'^{17}O$ of drinking water and leaf water with 2 ppm $\leq \Delta'^{17}O_{DW} \leq$ 21 ppm and -142 ppm $\leq \Delta'^{17}O_{LW} \leq$ -92 ppm, respectively. $\delta^{18}O$ and $\Delta'^{17}O$ composition of drinking and leaf water of the additional mammals from this study are listed in Appendix S2. All calculations are done in Python.

Figure 11: The $\delta^{18}O$ and $\Delta'^{17}O$ of drinking water and leaf water. Blue points: drinking waters, blue curve: $\delta^{18}O_{DW}$ (-15 to 5‰), $\Delta'^{17}O_{DW}$ (-50 to 40 ppm). Green points: leaf waters, green curve: $\delta^{18}O_{LW}$ (-1 to 18‰), $\Delta'^{17}O_{LW}$ (-155 to 34 ppm).
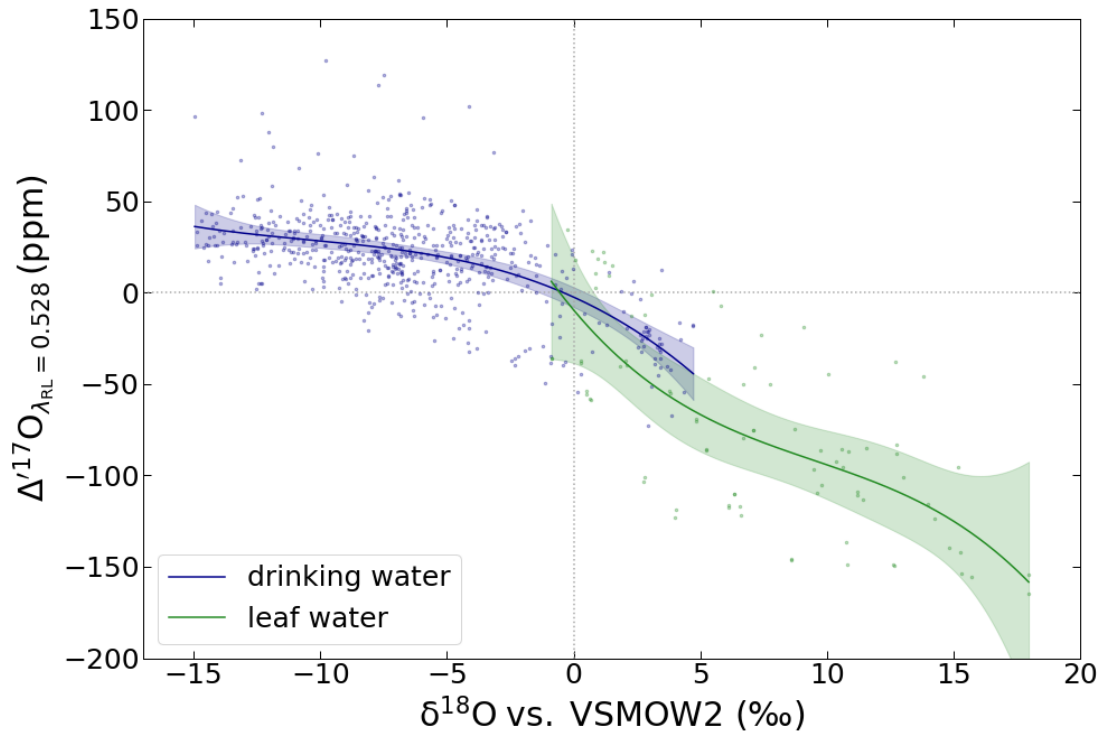
5   Discussion

5.1   Variations in $\delta^{13}C_{CO3}$ and $\delta^{18}O_{CO3}$

Modern and fossil tooth enamel $\delta^{13}C$ and $\delta^{18}O_{CO3}$ are known to reflect environmental conditions (DeNiro and Epstein, 1978; Longinelli, 1984; Lee-Thorp and van der Merwe, 1987; Kohn, 1996; Cerling et al., 1997a; MacFadden et al., 1999; Kohn et al., 2005; Levin et al., 2006), dietary, physiological differences, and niche partitioning (Cerling et al., 1997b; Ehleringer and Cooper, 1988; Kohn et al., 1998; Sharp and Cerling, 1998; Tütken and Vennemann, 2009), whereas $\delta^{13}C$ is strongly controlled by ingested food (DeNiro and Epstein, 1978).

Oryx gazella, *Alcelaphus caama*, *Kobus ellipsiprymnus defassa*, *Alcelaphus lichtensteinii*, *Connochaetes taurinus*, *Philantomba monticola*, *Connochaetes gnou*, *Aepyceros melampus*, and *Ammodorcas clarkei* from Africa (Fig. 3, dark orange diamond) have high $\delta^{13}C$ values (> -1‰) and $\delta^{18}O_{CO3}$ (> 30.45‰). Kohn et al. (2005) demonstrated that high (> -5‰) vs. low (< -9‰) $\delta^{13}C$ values of herbivore tooth enamel indicate local vegetation being dominated by warm-climate grasses vs. trees and shrubs. Levin et al. (2006) demonstrated that tooth enamel

$\delta^{18}O_{CO3}$ increases with environmental aridity. Related modern species are typically C_4 plant grazers living in warm and dry environments (e.g. deserts) and predominantly depend on water from food. The remaining African herbivores from are C_3 browsers and from relatively cold environments.

The herbivores from Australia, North and South America, and Central Europe, are all C_3 consumers. In contrary, carnivore tooth enamel $\delta^{13}C$ mainly reflects the $\delta^{13}C$ of ingested prey (Kohn et al., 2005). Tooth enamel $\delta^{18}O_{CO3}$ is dependent on the isotopic composition of the body fluid and hence local drinking water (*e.g.* rainfall) which can vary according to aridity, temperature, moisture source, and continentality (Beverly et al., 2021; Lehmann et al., 2021; Levin et al., 2006).

5.2 Variations in $\delta^{18}O_{PO4}$ and $\Delta'^{17}O$

The individual tooth enamel $\delta^{18}O_{PO4}$ values (Figure 4) decrease with their associated climate from warm and dry (e.g. Africa) to colder and wetter environments (e.g. Central Europe) with a total range of 21.2‰ (6.8 to 28.0‰), which is also evident from $\delta^{18}O_{CO3}$. The corresponding $\Delta'^{17}O$ range is 165 ppm (-250 to -85 ppm), which implies different mammal physiologies. It has been demonstrated that a lowering of $\Delta'^{17}O$ in the carbonate group is indicative of higher aridity (Passey et al., 2014; Passey and Levin, 2021). However, our $\Delta'^{17}O$ dataset of African Artiodactyla specimens does not confirm this relationship (Figure 3).

The $\delta^{18}O_{AP}$ of Australian as well as North and South American mammals plot between the data of specimens from hot and arid climates (Africa) and humid continental climate (Central Europe), whereas $\Delta'^{17}O$ does not reflect this trend which corroborates the hypothesis that $\Delta'^{17}O$ is predominantly modulated by differences in physiology. The Australian *Macropodidae* $\delta^{18}O_{AP}$ and $\Delta'^{17}O$ vary by 0.9‰ and 37 ppm, respectively (Figure 4 A; n=5). The $\delta^{18}O_{AP}$ and $\Delta'^{17}O$ from Central European mammals show a larger range of 12.0‰ and 165 ppm, respectively (n=92). The range of the ladder reduces if only taxon specific data are considered. *Capreolus capreolus* from the same population in Central Germany range by 5.2‰ for $\delta^{18}O_{AP}$ and 98 ppm for $\Delta'^{17}O$ (n=29). The mechanism for this intra-populational variation is currently not resolvable and might be caused by differences in body weight, nutrition, and behavior which could alter metabolic rates and ingested amounts of water.

The phosphate as well as the carbonate $\delta^{18}O$ fraction of tooth enamel is commonly used for (palaeo)climatic, (palaeo)ecological, and (palaeo)environmental reconstructions (Gehler et

al., 2011; Levin et al., 2006; Pack et al., 2013; Passey et al., 2014; Sharp and Cerling, 1998; Tütken et al., 2006), whereas the phosphate group is less susceptible for diagenetic alteration when compared to the carbonate group (Kohn et al., 1999; Kohn and Cerling, 2002; Kolodny et al., 1983; Shemesh et al., 1983). Well preserved bioapatite generally shows a consistent $\Delta^{18}O_{CO3-PO4}$ offset of 7.5 to 11.4‰ (Chenery et al.,2012; Gehler et al., 2012) which is confirmed by the data of this study which averages to $\Delta^{18}O_{CO3-PO4} = 9.54 \pm 3.02$‰ (n=96).

The mammalian bioapatite $\Delta'^{17}O$ of the phosphate group systematically decreases with body mass M_b (Figure 12). This effect is especially visible for taxa with $M_b < 1$ kg as their high metabolic rates lead to the incorporation of a more negative $\Delta'^{17}O$ anomaly into their tooth enamel when compared to larger taxa with lower metabolic rates (e.g African elephant). For example, the tooth enamel $\Delta'^{17}O$ of the smallest mammals *Suncus etruscus* and *Apodemus sylvaticus* ($M_b < 100$ g) are >140 ppm more negative when compared to *Loxodonta Africana* ($M_b \sim 4000$ kg).
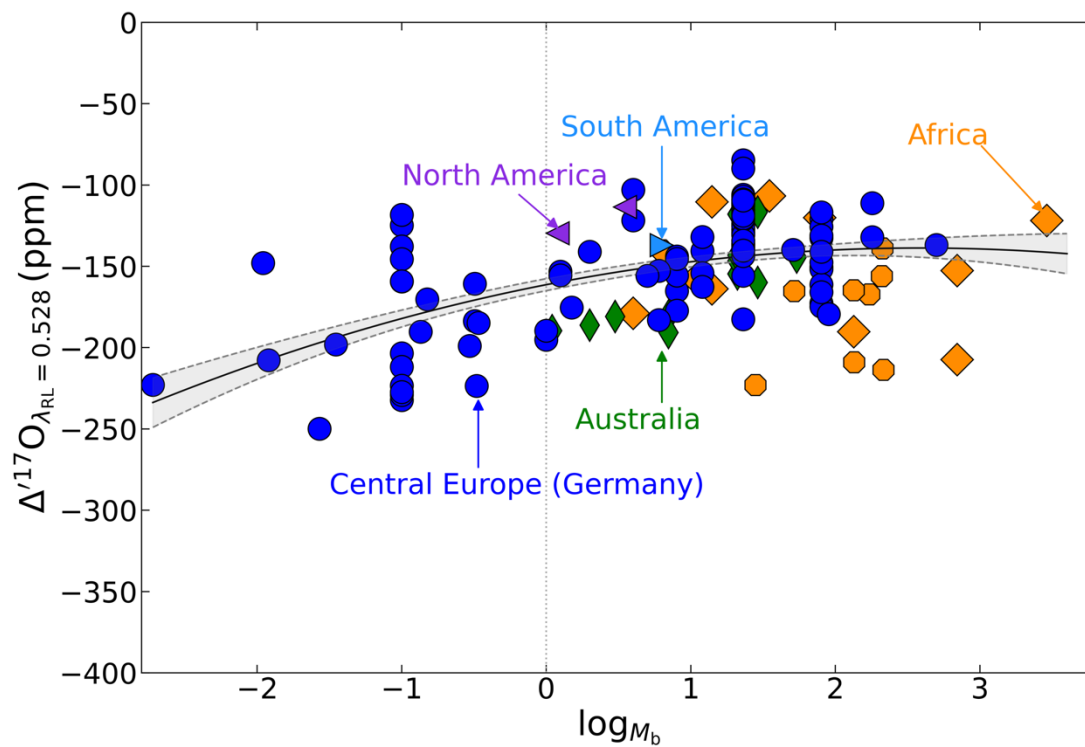

Figure 12: Crossplot of the logarithmic body mass *vs.* bioapatite $\Delta'^{17}O$ of the sampled taxa. Brown squares: African mammals, green diamonds: Australian mammals, blue circles: Central European/German mammals.

5.3 Comparison of modeled and measured $\Delta'^{17}O$

An overview of the data calculated for all mammalian taxa (incl. mass balance model) are provided in the Appendix S2. Data from $\Delta'^{17}O$ analyses and mass balance models are shown in Figure 13 & 14 for $\delta^{18}O$ and $\Delta'^{17}O$ for comparison.

For small mammals ($M_b < 1$ kg) such as *Suncus etruscus* and *Apodemus sylvaticus*, the mass balance models indicate that the air O_2 fractionation in body water can be dominant (up to 50%) because of the high specific metabolic rates of the taxa (Kleiber, 1947; Singer, 2001; Schmidt-Nielsen, 1972; 1984). In this case, bioapatite carries ~ 50% of the $\Delta'^{17}O$ anomaly of air O_2 (-432 ± 15ppm; Barkan and Luz, 2005; Young et al., 2014; Pack et al., 2017; Sharp et al., 2018; Yeung et al., 2018; Wostbrock et al., 2020; Pack, 2021), with $\Delta'^{17}O = \sim -216$ ppm; an assumption that is verified by the measured large $\Delta'^{17}O_{PO4}$ anomalies in this study.

The comparison of measured and modeled tooth enamel $\delta^{18}O$ and $\Delta'^{17}O$ highlights the associated and unavoidable intrinsic uncertainties, which are mainly due to a limited understanding of taxon-specific variations of physiology, behavior, and environment. Because the oxygen compositions for the different fluxes are frequently unknown for the precise habitats and associated oxygen sources, our mass balance models consider more generalized conditions. The outliers of the C_4 grazers from Africa could imply that the amounts of drinking water from literature are overestimated and/or that the $\delta^{18}O$ and $\Delta'^{17}O$ of drinking and leaf water could be fractionated to a larger extend than assumed in our model (Ellsworth et al., 2017).

For the carnivores, we present $\Delta'^{17}O$ without performing a mass balance validation because of lacking information of the oxygen compositions of their precise food sources.
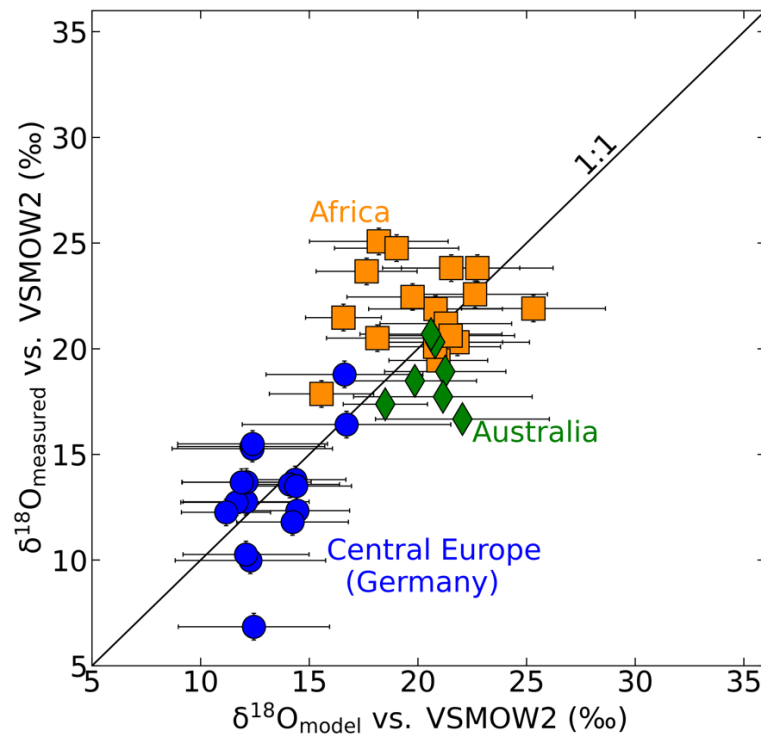
Figure 13: Modelled vs. measured tooth enamel $\delta^{18}O$. Brown squares: African mammals, green diamonds: Australian mammals, blue circles: Central European/German mammals.
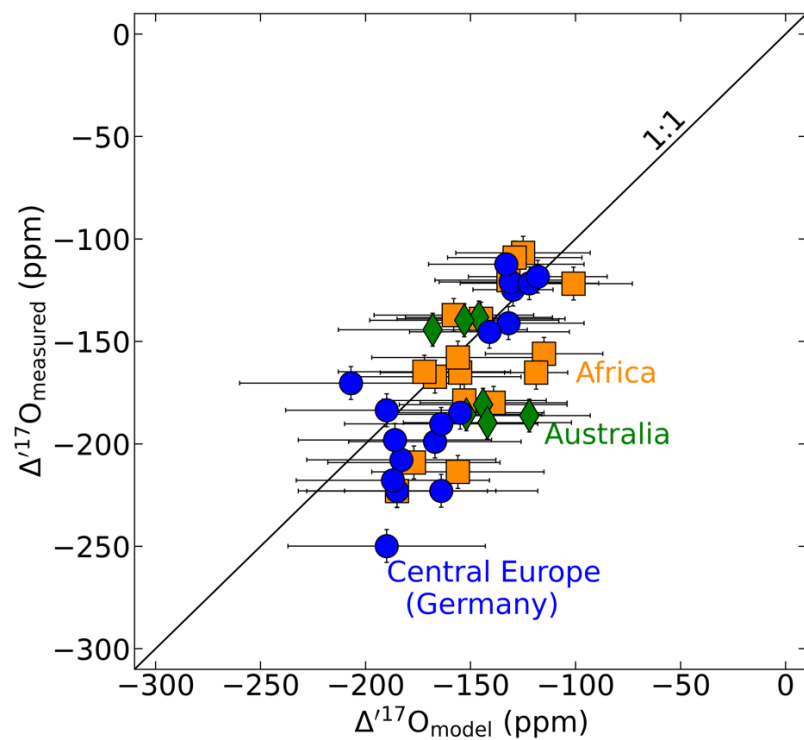

Figure 14: Modelled vs. measured tooth enamel $\Delta'^{17}O$. Brown squares: African mammals, the green diamonds: Australian mammals, blue circles: Central European/German mammals.

Figure 15 illustrates that small mammals are more sensitive to changes in air $\Delta'^{17}O$. Moreover, large mammals from dry environments are not as sensitive as proposed by Passey et al. (2014, 2021). The differences in sensitivity can be explained by the fact that the metabolic rates of small mammals are 50 times higher when compared *Loxodonta africana*. Hence, tooth enamel from small mammals is a welly suited archive for $\Delta'^{17}O$ of past atmospheric molecular O_2.
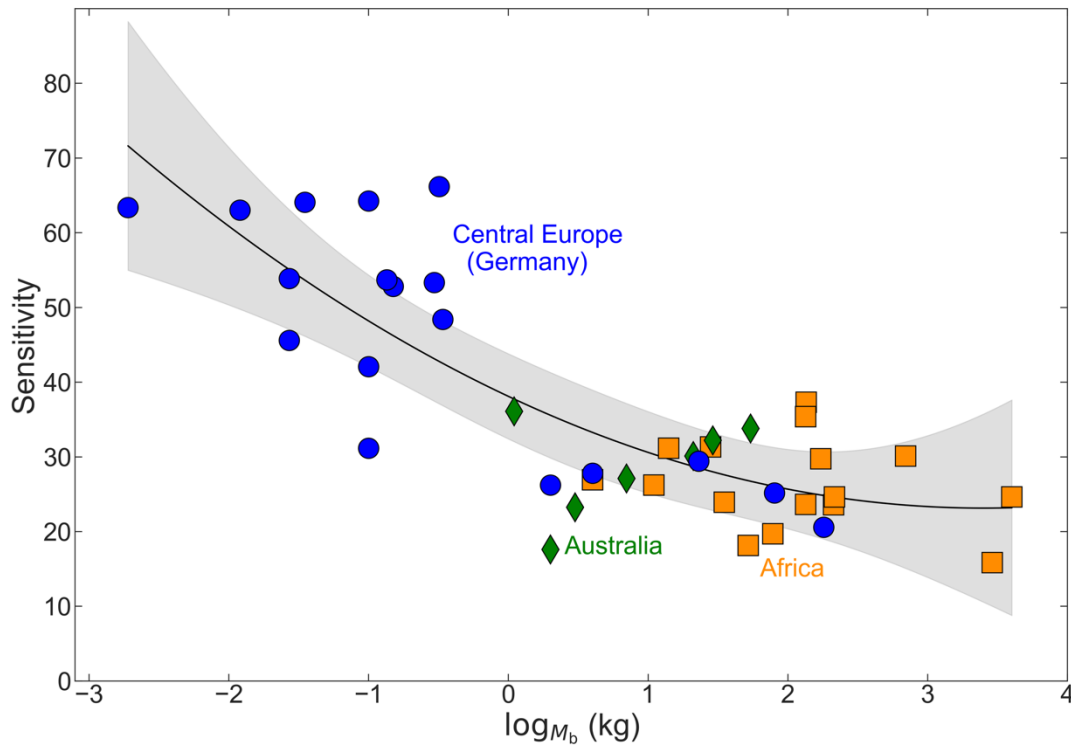
Figure 15: Sensitivity ($\frac{\Delta\Delta'^{17}O_{AP}}{\Delta\Delta'^{17}O_{Air}} \times 100$) of bioapatite $\Delta'^{17}O$ of the sampled taxa from mass balance models when changing air $\Delta'^{17}O$ vs. the logarithmic body mass. Brown squares: African mammals, green diamonds: Australian mammals, blue circles: Central European/German mammals.

5.3 $\Delta'^{17}O$ as a paleo-CO_2 proxy

Pack et al. (2013) suggested that bioapatite $\Delta'^{17}O$ of terrestrial mammals can be used as paleo-CO_2 proxy (see also Gehler et al., 2016). Feng et al. (2022) demonstrated that bioapatite $\Delta'^{17}O$ of marine mammals bear anomalous $\Delta'^{17}O_{air}$ signatures and proposed that bioapatite $\Delta'^{17}O$ of a small marine mammals could be a suitable proxy for past air O_2 $\Delta'^{17}O$ ($\Delta'^{17}O_{air}$) during high pCO_2 periods in Earth history. This is ascribed to the assumptions, that mammals with very small body masses and high metabolic rates are most sensitive for changes in $\Delta'^{17}O_{air}$, and that $\Delta'^{17}O_{air}$ anomalies should be recorded most noticeable in

bioapatite $\Delta'^{17}O$ that forms during high pCO_2 intervals. This theory can be confirmed by running our taxon specific mass balance models (i.e. varying body masses) at varying O_2 $\Delta'^{17}O$ boundary conditions. We thus can show that the sensitivity of bioapatite $\Delta'^{17}O$ from land-living mammals not only increases with decreasing body mass, but also with decreasing $\Delta'^{17}O_{air}$ (Figure 16). Because the average $\Delta'^{17}O_{AP}$ from the *Capreolus capreolus* tooth enamel data is identical with the model $\Delta'^{17}O_{AP}$, which is calculated from the modern $\Delta'^{17}O_{air}$ (Figure 7), the experimentally derived $\Delta'^{17}O_{air}$ also agrees with the modern value. At constant GPP, the experimentally determined pCO_2 is, therefore, equal to the present pCO_2.
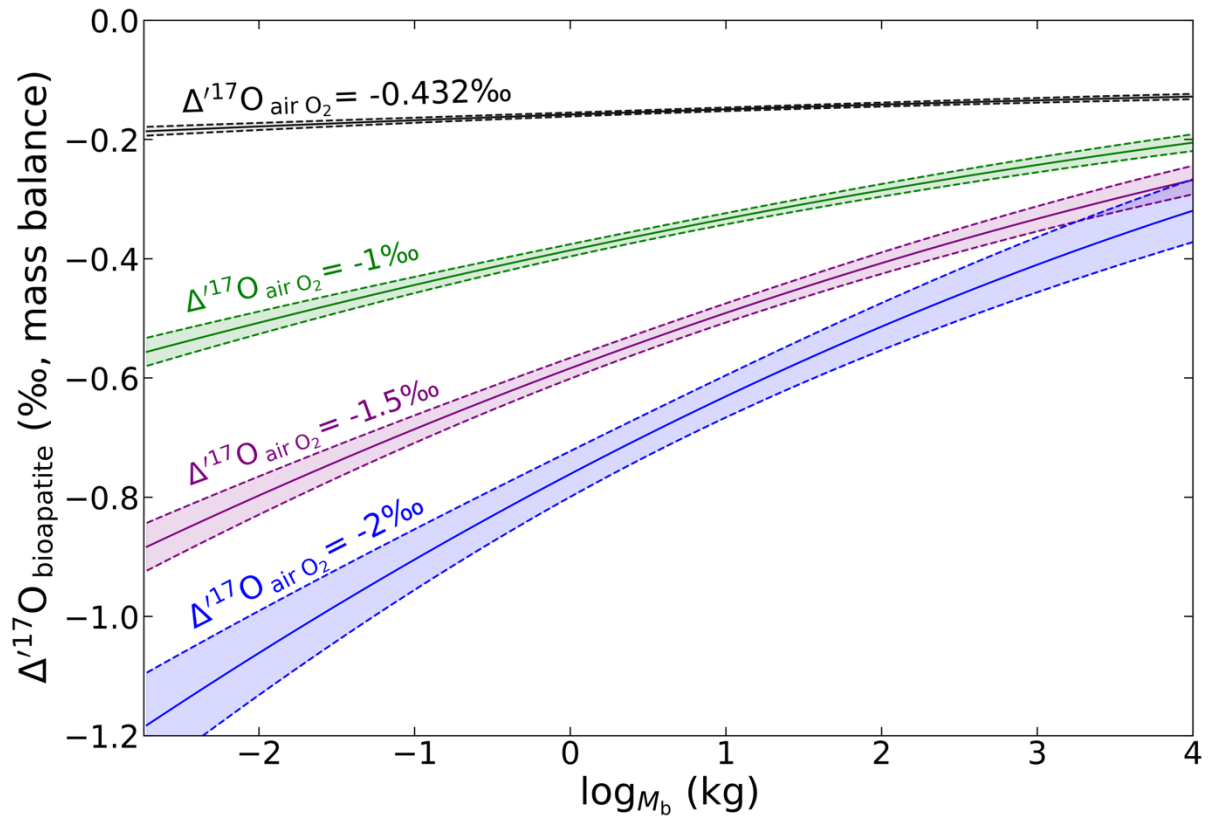
Figure 16: Sensitivity plot of $\Delta'^{17}O$ of bioapatite (from mass balance models) vs. the logarithmic body mass for air O_2 $\Delta'^{17}O$ ($\Delta'^{17}O_{air}$) between -2‰ to -0.432‰.

The sensitivity test reveals that small land-living mammals ($Mb < 1kg$) tend to be more sensitive to changes in $\Delta'^{17}O_{air}$ when compared to large land-living mammals (e.g. *Loxodonta africana*) and that the bioapatite $\Delta'^{17}O$ sensitivity for body masses <100 kg increases with decreasing $\Delta'^{17}O_{air}$. At $\Delta'^{17}O_{air}$ as low as -2‰, maximum bioapatite $\Delta'^{17}O$ anomalies of ~ -700 ppm are expected for the smallest taxa.

The relation of $\Delta'^{17}O$ anomalies measured on tooth enamel from small mammals, and inhaled air $\Delta'^{17}O$ can be used to determine the $\Delta'^{17}O$ of past tropospheric O_2 (e.g. Pack et al., 2013;

their eq. 16). The $\Delta'^{17}O$ of tropospheric O_2 is, in turn, related to pCO_2 and gross primary production (GPP). At a given GPP, $\Delta'^{17}O_{air}$ can be estimated from $\Delta'^{17}O_{AP}$ and thus pCO_2 can be determined from $\Delta'^{17}O$ measured on fossil tooth enamel.

6   Conclusions

- Laser fluorination of chemically and thermally pretreated tooth enamel is shown to be a suitable method for liberating oxygen analyte gas for highly precise IRMS analysis of $\Delta'^{17}O$ ($\pm$ 8 ppm; 1σ, SD, n=82). Under consideration of taxon specific oxygen mass balance models that account for environmental and physiological variations, pronounced negative $\Delta'^{17}O$ anomalies (< -100 ppm) are identified. This is ascribed to the inheritance of isotopically anomalous inhaled air O_2 whose contribution can be best resolved for small terrestrial mammals (M_b < 1 kg).

- Detailed mass balance calculations presented herein support the theory that inhaled anomalous air O_2 is partially transferred into the tooth enamel phosphate group as modeled and measured results are indistinguishable from each other for a large data set of *Capreolus capreolus* (n=29). However, intra-populational $\Delta'^{17}O_{AP}$ variations (< 100 ppm) suggests the presence of varying physiological parameters and different individual behaviors, potentially related to slightly different body masses and sex.

- Sensitivity analyses of $\Delta'^{17}O_{AP}$ reveal that tooth enamel from small fossil mammals (M_b < 1 kg) most precisely records variations in $\Delta'^{17}O_{Air}$. Its sensitivity further increases with decreasing $\Delta'^{17}O_{Air}$. We therefore advocate focusing on both small mammalian bioapatite samples and high pCO_2 environments for verifying the applicability of $\Delta'^{17}O$-based pCO_2 reconstructions using the methods and models presented in this study. Furthermore, combining this approach with sophisticated oxygen mass balance models also bears a strong potential for (paleo)climatic, (paleo)ecological and (paleo)environmental reconstructions.

7 Acknowledgements

8 Appendix

Supplementary data S1 and S2 to this article can be found online at https://data.goettingen-research-online.de/dataset.xhtml?persistentId=doi:10.25625/1IUKIC

9 References

Affolter, S., Häuselmann, A.D., Fleitmann, D., Häuselmann, P., Leuenberger, M., 2015. Triple isotope (δD, δ^{17}O, δ^{18}O) study on precipitation, drip water and speleothem fluid inclusions for a Western Central European cave (NW Switzerland). Quat. Sci. Rev. 127, 73–89.

Alexandre, A., Webb, E., Landais, A., Piel, C., Devidal, S., Sonzogni, C., Couapel, M., Mazur, J.C., Pierre, M., Prié, F., Vallet-Coulomb, C., Outrequin, C., Roy, J., 2019. Effects of leaf length and development stage on the triple oxygen isotope signature of grass leaf water and phytoliths: Insights for a proxy of continental atmospheric humidity. Biogeosciences 16, 4613–4625.

Aron, P.G., Levin, N.E., Beverly, E.J., Huth, T.E., Passey, B.H., Pelletier, E.M., Poulsen, C.J., Winkelstern, I.Z., Yarian, D.A., 2021. Triple oxygen isotopes in the water cycle. Chem. Geol. 565, 1-23.

Arrhenius, S., 1896. On the influence of carbonic acid in the air upon the temperature of the ground. The London, Edinburgh, and Dublin Philosophical Magazine and Journal of Science 41, 237-276.

Bao H., Lyons, J. R., Zhou, C., 2008. Triple oxygen isotope evidence for elevated CO_2 levels after a Neoproterozoic glaciation. Nature 453, 504–506.

Barkan, E., Luz, B., 2005. High precision measurements of ^{17}O/^{16}O and ^{18}O/^{16}O ratios in H_2O. Rapid Commun. Mass Spectrom. 19, 3737–3742.

Bender, M.L., Sowers, T., Barnola, J.M., Chappellaz, J., 1994. Changes in the O_2/N_2 ratio of the atmosphere during. Geophys. Res. Lett. 21, 189–192.

Bergel, S.J., Barkan, E., Stein, M., Affek, H.P., 2020. Carbonate ^{17}O$_{excess}$ as a paleo-hydrology proxy: Triple oxygen isotope fractionation between H_2O and biogenic aragonite, derived from freshwater mollusks. Geochim. Cosmochim. Acta 275, 36–47.

Berner, R.A., 2006a. Inclusion of the weathering of volcanic rocks in the GEOCARBSULF model. Am. J. Sci. 306, 295–302.

Berner, R.A., 2006b. GEOCARBSULF: A combined model for Phanerozoic atmospheric O_2 and CO_2. Geochim. Cosmochim. Acta 70, 5653–5664.

Bershaw, J., Hansen, D.D., Schauer, A.J., 2020. Deuterium excess and ^{17}O-excess variability in meteoric water across the Pacific Northwest, USA. Tellus, Ser. B Chem. Phys. Meteorol. 72, 1–17.

Beverly, E.J., Levin, N.E., Passey, B.H., Aron, P.G., Yarian, D.A., Page, M., Pelletier, E.M.,

2021. Triple oxygen and clumped isotopes in modern soil carbonate along an aridity gradient in the Serengeti, Tanzania. Orphanet J. Rare Dis. 21, 1–9.

Blunier, T., Barnett, B., Bender, M.L., Hendricks, M.B., 2002. Biological oxygen productivity during the last 60,000 years from triple oxygen isotope measurements. Global Biogeochem. Cycles 16, 1–15.

Bowen, G.J., Revenaugh, J., 2003. Interpolating the isotopic composition of modern meteoric precipitation. Water Resour. Res. 39, 1–13.

Bowen, G.J., 2018. The online isotopes in precipitation calculator, version 3.1. Available at: http://www.waterisotopes.org.

Breecker, D.O., Sharp, Z.D., McFadden, L.D., 2010. Atmospheric CO_2 concentrations during ancient greenhouse climates were similar to those predicted for A.D. 2100. Proc. Natl. Acad. Sci. U. S. A. 107, 576–580.

Brenninkmeijer, C.A.M., Kraft, P., Mook, W.G., 1983. Oxygen isotope fractionation between CO_2 and H_2O. Chem. Geol. 41, 181–190.

Bryant, D.J., Froelich, P.N., 1995. A model of oxygen isotope fractionation in body water of large mammals. Geochim. Cosmochim. Acta 59, 4523–4537.

Burk, R.L., Stuiver, M., 1981. Oxygen isotope ratios in trees: Reflect mean annual temperature and humidity. Science (80-.). 212, 1417–1419.

Cerling, T.E., Harris, J.M., MacFadden, B.J., Leakey, M.G., Quade, J., Eisenmann, V., Ehieringer, J.R., 1997a. Global vegetation change through the Miocene/Pliocene boundary. Nature 389, 153–158.

Cerling, T.E., Harris, J.M., Ambrose, S.H., Leakey, M.G., Solounias, N., 1997b. Dietary and environmental reconstruction with stable isotope analyses of herbivore tooth enamel from the Miocene locality of Fort Ternan, Kenya. J. Hum. Evol. 33, 635–650.

Chenery, C., Müldner, G., Evans, J., Eckardt, H., Lewis, M., 2010. Strontium and stable isotope evidence for diet and mobility in Roman Gloucester, UK. J. Archaeol. Sci. 37, 150–163.

Chenery, C.A., Pashley, V., Lamb, A.L., Sloane, H..J., Evans, J.A., 2012. The oxygen isotope relationship between the phosphate and structural carbonate fractions of human bioapatite. Rapid Commun. Mass Spectrom. 26, 309-319.

Cheung, P.C.K. and Mehta B.M., 2015. Handbook of food chemistry. Springer Reference, p639.

Dansgaard, W., 1964. Stable isotopes in precipitation. Tellus 16, 436-468.

DeNiro, M.J., Epstein, S., 1978. Influence of diet on the distribution of carbon isotopes in

animals. Geochim. Cosmochim. Acta 42, 495–506.

Dettman D. L., Kohn M. J., Quade J., Ryerson F. J., Ojha T. P. and Hamidullah S., 2001. Seasonal stable isotope evidence for a strong Asian monsoon throughout the past 10.7 m.y. Geology 29, 31–34.

Edwards, T.W.D., Aravena, R.O., Fritz, P., Morgan, A. V., 1985. Interpreting paleoclimate from ^{18}O and ^2H in plant cellulose: comparison with evidence from fossil insects and relict permafrost in southwestern Ontario. Can. J. Earth Sci. 22, 1720–1726.

Ehleringer, J.R., Cooper, T.A., 1988. Correlations between carbon isotope ratio in desert plants. Oecologica 76, 562–566.

Ellsworth, P.Z., Ellsworth, P. V., Cousins, A.B., 2017. Relationship of leaf oxygen and carbon isotopic composition with transpiration effciency in the C_4 grasses Setaria viridis and Setaria italica. J. Exp. Bot. 68, 3513–3528.

Epstein, S., Zeiri, L., 1988. Oxygen and carbon isotopic compositions of gases respired by humans. Proc. Natl. Acad. Sci. U. S. A. 85, 1727–1731.

Evans, N.P., Bauska, T.K., Gázquez-Sánchez, F., Brenner, M., Curtis, J.H., Hodell, D.A., 2018. Quantification of drought during the collapse of the classic Maya civilization. Science (80-.). 361, 498–501.

Feng, D.S., Tütken, T., Löffler, N., Tröster, G., Pack, A., 2022. Isotopically anomalous metabolic oxygen in marine vertebrates as physiology and atmospheric proxy. Geochim. Cosmochim. Acta , in review.

Foster, G.L., Royer, D.L., Lunt, D.J., 2017. Future climate forcing potentially without precedent in the last 420 million years. Nat. Commun. 8, 1–8.

Gat, J.R., 1996. Oxygen and hydrogen isotopes in the hydrologic cycle. Annu. Rev. Earth Planet. Sci. 24: 225-262.

Gat, J.R., Mook, W.G., Meijer, H.A.J., 2000. Volume II : Atmospheric Water. in: Environmental isotopes in the hydrological cycle. Mook WG (ed) UNESCO, Paris.

Gázquez, F., Morellón, M., Bauska, T., Herwartz, D., Surma, J., Moreno, A., Staubwasser, M., Valero-Garcés, B., Delgado-Huertas, A., Hodell, D.A., 2018. Triple oxygen and hydrogen isotopes of gypsum hydration water for quantitative paleo-humidity reconstruction. Earth Planet. Sci. Lett. 481, 177–188.

Gehler, A., Tütken, T., Pack, A., 2011. Triple oxygen isotope analysis of bioapatite as tracer for diagenetic alteration of bones and teeth. Palaeogeogr. Palaeoclimatol. Palaeoecol. 310, 84–91.

Gehler A., Tütken T., Pack A., 2012. Oxygen and Carbon Isotope Variations in a Modern

Rodent Community - Implications for Palaeoenvironmental Reconstructions. PLoS ONE 7, 16–27.

Gehler A., Gingerich P. D., Pack A., 2016. Temperature and atmospheric CO_2 concentration estimates through the PETM using triple oxygen isotope analysis of mammalian bioapatite. Proc. Natl. Acad. Sci. U. S. A. 113, 7739–7744.

Guo W., Zhou C., 2019. Triple oxygen isotope fractionation in the DIC-H_2O-CO_2 system: A numerical framework and its implications. Geochim. Cosmochim. Acta 246, 541–564.

Hayles, J., Gao, C., Cao, X., Liu, Y., Bao, H., 2018. Theoretical calibration of the triple oxygen isotope thermometer. Geochim. Cosmochim. Acta 235, 237–245.

Horita, J., Wesolowski, D.J., 1994. Horita and Wesolowski 1994. Geochim. Cosmochim. Acta 58, 1–13.

Hulston J R and Thode H G, 1965. Variations in the S^{33} S^{34} and S^{36} Contents of Meteorites and Their Relation to Chemical and Nuclear Effects. J. Geophys. Res. 70, 3475–3484.

Kleiber, M., 1947. Physiological reviews. J. Physiol. 27, 511–541.

Kohn, M.J., 1996. Predicting animal $\delta^{18}O$: Accounting for diet and physiological adaptation. Geochim. Cosmochim. Acta 60, 4811–4829.

Kohn, M.J., Cerling, T.E., 2002. Stable isotope compositions of biological apatite. Phosphates Geochemical, Geobiol. Mater. Importance 48, 455–488.

Kohn, M.J., McKay, M.P., Knight, J.L., 2005. Dining in the Pleistocene - Who's on the menu? Geology 33, 649–652.

Kohn, M.J., Schoeninger, M.J., Barker, W.W., 1999. Altered states: Effects of diagenesis on fossil tooth chemistry. Geochim. Cosmochim. Acta 63, 2737–2747.

Kohn, M.J., Schoeninger, M.J., Valley, J.W., 1998. Variability in oxygen isotope compositions of herbivore teeth: reflections of seasonality or developmental physiology? Chem. Geol. 152, 97–112.

Kolodny, Y., Luz, B., Navon, O., 1983. Oxygen isotope variations in phosphate of biogenic apatites, I. Fish bone apatite-rechecking the rules of the game. Earth Planet. Sci. Lett. 64, 398–404.

König, A., Hudler, M., Dahl, S.A., Bolduan, C., Brugger, D., Windisch, W., 2020. Response of roe deer (*Capreolus capreolus*) to seasonal and local changes in dietary energy content and quality. Anim. Prod. Sci. 60, 1315–1325.

Kürschner, W.M., Kvaček, Z., Dilcher, D.L., 2008. The impact of Miocene atmospheric carbon dioxide fluctuations on climate and the evolution of terrestrial ecosystems. Proc. Natl. Acad. Sci. U. S. A. 105, 449–453.

Landais, A., Barkan, E., Yakir, D., Luz, B., 2006. The triple isotopic composition of oxygen in leaf water. Geochim. Cosmochim. Acta 70, 4105–4115.

Landais, A., Risi, C., Bony, S., Vimeux, F., Descroix, L., Falourd, S., Bouygues, A., 2010. Combined measurements of $^{17}O_{excess}$ and d_{excess} in African monsoon precipitation: Implications for evaluating convective parameterizations. Earth Planet. Sci. Lett. 298, 104–112.

Lécuyer, C., Grandjean, P., O'Neil, J.R., Cappetta, H., Martineau, F., 1993. Thermal excursions in the ocean at the Cretaceous-Tertiary boundary (northern Morocco): $\delta^{18}O$ record of phosphatic fish debris. Palaeogeogr. Palaeoclimatol. Palaeoecol. 105, 235–243.

Lee-Thorp, J.A., Van der Merwe, N.J., 1987. Carbon isotope analysis of fossil bone apatite. South African Journal of Science, 83, 712-715.

Lee-Thorp, J.A., Sponheimer, M., Luyt, J., 2007. Tracking changing environments using stable carbon isotopes in fossil tooth enamel: an example from the South African hominin sites. J. Hum. Evol. 53, 595–601.

Lehmann, S.B., Levin, N.E., Passey, B.H., Hu, H., Cerling, T.E., Miller, J.H., Arppe, L., Beverly, E.J., Hoppe, K.A., Luyt, J., Sealy, J., 2021. Triple oxygen isotope distribution in modern mammal teeth and potential geologic applications. Geochim. Cosmochim. Acta, in review.

Leuenberger M.C. and Ranjan S., 2021. Disentangle kinetic from equilibrium fractionation using primary ($\delta^{17}O$, $\delta^{18}O$, δD) and secondary ($\Delta^{17}O$, d_{ex}) stable isotope parameters on samples from the Swiss precipitation network. Front. Earth Sci, 9: 1-15.

Levin, N.E., Cerling, T.E., Passey, B.H., Harris, J.M., Ehleringer, J.R., 2006. A stable isotope aridity index for terrestrial environments. Proc. Natl. Acad. Sci. U. S. A. 103, 11201–11205.

Li, S., Levin, N.E., Chesson, L.A., 2015. Continental scale variation in $^{17}O_{excess}$ of meteoric waters in the United States. Geochim. Cosmochim. Acta 164, 110–126.

Li, S., Levin, N.E., Soderberg, K., Dennis, K.J., Caylor, K.K., 2017. Triple oxygen isotope composition of leaf waters in Mpala, central Kenya. Earth Planet. Sci. Lett. 468, 38–50.

Lifson, N., McClintock, R., 1966. Theory of use of the turnover rates of body water for measuring energy and material balance. J. Theor. Biol. 12, 46–74.

Lin, Y., Clayton, R.N., Huang, L., Nakamura, N., Lyons, J.R., 2013. Oxygen isotope anomaly observed in water vapor from Alert, Canada and the implication for the stratosphere. Proc. Natl. Acad. Sci. U. S. A. 110, 15608–15613.

Lindars, E.S., Grimes, S.T., Mattey, D.P., Collinson, M.E., Hooker, J.J., Jones, T.P., 2001. Phosphate $\delta^{18}O$ determination of modern rodent teeth by direct laser fluorination: An appraisal of methodology and potential application of palaeoclimate reconstruction. Geochim. Cosmochim. Acta 65, 2535–2548.

Longinelli, A., 1984. Oxygen isotopes in mammal bone phosphate: A new tool for paleohydrological and paleoclimatological research? Geochim. Cosmochim. Acta 48, 385–390.

Lüthi, D., Le Floch, M., Bereiter, B., Blunier, T., Barnola, J.M., Siegenthaler, U., Raynaud, D., Jouzel, J., Fischer, H., Kawamura, K., Stocker, T.F., 2008. High-resolution carbon dioxide concentration record 650,000-800,000 years before present. Nature 453, 379–382.

Luz, B., Barkan, E., 2010. Variations of $^{17}O/^{16}O$ and $^{18}O/^{16}O$ in meteoric waters. Geochim. Cosmochim. Acta 74, 6276–6286.

Luz, B., Barkan, E., 2005. The isotopic ratios $^{17}O/^{16}O$ and $^{18}O/^{16}O$ in molecular oxygen and their significance in biogeochemistry. Geochim. Cosmochim. Acta 69, 1099–1110.

Luz, B., Barkan, E., Bender, M.L., Thiemens, M.H., Boering, K.A., 1999. Triple-isotope composition of atmospheric oxygen as a tracer of biosphere productivity. Nature 400, 547–550.

MacFadden, B.J., Solounias, N., Cerling, T.E., 1999. Ancient diets, ecology, and extinction of 5-million-year-old horses from Florida. Science (80-.). 283, 824–827.

McKendry, P., 2002. Energy production from biomass (part 1): overview of biomass. Bioresour. Technol. 83, 37–64.

Nave R., 2000. HyperPhysics Thermodynamics. http://hyperphysics.phy-astr.gsu.edu/hbase/Kinetic/relhum.html.

Onderscheka K. (1999) Das Rehwild: seine Ernährung und Fütterung. In 'Rehwild in der Kulturlandschaft. Nürnberg. Schriftenreihe des Landesjagdverbandes Bayern e.V.: München, Germany, 7, p. 37–60.

Pack, A., Gehler, A., Süssenberger, A., 2013. Exploring the usability of isotopically anomalous oxygen in bones and teeth as paleo-CO_2-barometer. Geochim. Cosmochim. Acta 102, 306–317.

Pack A., Tanaka R., Hering M., Sengupta S., Peters S. and Nakamura E. (2016) The oxygen isotope composition of San Carlos olivine on the VSMOW2-SLAP2 scale. Rapid Commun. Mass Spectrom. 30, 1495–1504.

Pack, A., Höweling, A., Hezel, D.C., Stefanak, M.T., Beck, A.K., Peters, S.T.M., Sengupta,

S., Herwartz, D., Folco, L., 2017. Tracing the oxygen isotope composition of the upper Earth's atmosphere using cosmic spherules. Nat. Commun. 8, 1–7.

Pack, A., 2021. Isotopic Traces of Atmospheric O_2 in Rocks, Minerals, and Melts. Rev. Mineral. Geochemistry 86, 217–240.

Pagani, M., Zachos, J.C., Freeman, K.H., Tipple, B., Bohaty, S., 2005. Atmospheric science: Marked decline in atmospheric carbon dioxide concentrations during the Paleogene. Science (80-.). 309, 600–603.

Passey, B.H., Hu, H., Ji, H., Montanari, S., Li, S., Henkes, G.A., Levin, N.E., 2014. Triple oxygen isotopes in biogenic and sedimentary carbonates. Geochim. Cosmochim. Acta 141, 1.

Passey, B.H., Ji, H., 2019. Triple oxygen isotope signatures of evaporation in lake waters and carbonates: A case study from the western United States. Earth Planet. Sci. Lett. 518, 1–12.

Passey, B.H., Levin, N.E., 2021. Triple oxygen isotopes in carbonates, biological apatites, and continental paleoclimate reconstruction. Rev. Mineral. Geochemistry 86, 429–626.

Pearson, P.N., Foster, G.L., Wade, B.S., 2009. Atmospheric carbon dioxide through the Eocene-Oligocene climate transition. Nature 461, 1110–1113.

Petit, J.R., Jouzel, J., Raynaud, D., Barnola, J.M., Basile, I., Bender, M., Chappellaz, J., Davis, M., Delaygue, G., Delmotte, M., Kotlyakov, V.M., Legrand, M., Lipenkov, V.Y., Loriu, C., Pepin, L., Ritz, C., Saltzman, E., Stievenard, M., 1999. Climate and atmospheric history of the past 420,000 years from the Vostok ice core, Antarctica. Nature 399, 348–358.

Roth-Nebelsick, A., 2005. Reconstructing atmospheric carbon dioxide with stomata: Possibilities and limitations of a botanical pCO$_2$-sensor. Trees - Struct. Funct. 19, 251–265.

Royer, D.L., Berner, R.A., Beerling, D.J., 2001. Phanerozoic atmospheric CO_2 change: Evaluating geochemical and paleobiological approaches, Earth-Science Reviews 54, 349-392.

Schmidt-Nielsen, K., 1972. Locomotion: energy cost of swimming, flying, and running. Science 177: 222-228.

Schmidt-Nielsen, K., 1984. Scaling, why is animal size so important? Cambridge Universiy Press, Cambridge, p241.

Schoeller, D.A., Leitch, C.A., Brown, C., 1986. Doubly labeled water method: In vivo oxygen and hydrogen isotope fractionation. Am. J. Physiol. - Regul. Integr. Comp.

Physiol. 251, 1137–1143.

Sha, L., Mahata, S., Duan, P., Luz, B., Zhang, P., Baker, J., Zong, B., Ning, Y., Brahim, Y.A., Zhang, H., Edwards, R.L., Cheng, H., 2020. A novel application of triple oxygen isotope ratios of speleothems. Geochim. Cosmochim. Acta 270, 360–378.

Sharp, Z.D., 1990. A laser-based microanalytical method for the in situ determination of oxygen isotope ratios of silicaes and oxides. Geochim. Cosmochim. Acta 54, 1353-1357.

Sharp, Z.D., Cerling, T.E., 1998. Fossil isotope records of seasonal climate and ecology: Straight from the horse's mouth. Geology 26, 219–222.

Sharp Z.D., Gibbons J.A., Maltsev O., Atudorei V., Pack A., Sengupta S., Shock E.L., Knauth L.P. (2016) A calibration of the triple oxygen isotope fractionation in the SiO_2 - H_2O system and applications to natural samples. Geochim. Cosmochim. Acta 186, 105–119.

Sharp, Z.D., Wostbrock, J.A.G., Pack, A., 2018. Mass-dependent triple oxygen isotope variations in terrestrial materials. Geochemical Perspect. Lett. 7, 27–31.

Shemesh, A., Kolodny, Y., Luz, B., 1983. Oxygen isotope variations in phosphate of biogenic apatites, II. Phosphorite rocks. Earth Planet. Sci. Lett. 64, 405–416.

Singer, M.A., 2001. Of mice and men and elephants: Metabolic rate sets glomerular filtration rate. American Journal of Kidney Diseases 37, 164–178.

Sisma-Ventura, G., Tütken, T., Peters, S.T.M., Bialik, O.M., Zohar, I., Pack, A., 2019. Past aquatic environments in the Levant inferred from stable isotope compositions of carbonate and phosphate in fish teeth. PLoS ONE. 14, 1-18.

Sternberg, L.D.S.L, 1989. Oxygen and Hydrogen Isotope Ratios in Plant Cellulose. Mechanisms and Applications, 124–141.

Surma, J., Assonov, S., Bolourchi, M.J., Staubwasser, M., 2015. Triple oxygen isotope signatures in evaporated water bodies from the Sistan Oasis, Iran. Geophys. Res. Lett. 42, 8456–8462.

Surma, J., Assonov, S., Herwartz, D., Voigt, C., Staubwasser, M., 2018. The evolution of [17]O-excess in surface water of the arid environment during recharge and evaporation. Sci. Rep. 8, 1–10.

Surma, J., Assonov, S., Staubwasser, M., 2021. Triple Oxygen Isotope Systematics in the Hydrologic Cycle. Rev. Mineral. Geochemistry 86, 401–428.

Tian, C., Wang, L., Kaseke, K.F., Bird, B.W., 2018. Stable isotope compositions (δ^2H, $\delta^{18}O$ and $\delta^{17}O$) of rainfall and snowfall in the central United States. Sci. Rep. 8, 1–15.

Tian, C., Wang, L., Tian, F., Zhao, S., Jiao, W., 2019. Spatial and temporal variations of tap

water $^{17}O_{excess}$ in China. Geochim. Cosmochim. Acta 260, 1–14.

Tütken, T., Vennemann, T.W., Janz, H., Heizmann, E.P.J., 2006. Palaeoenvironment and palaeoclimate of the Middle Miocene lake in the Steinheim basin, SW Germany: A reconstruction from C, O, and Sr isotopes of fossil remains. Palaeogeogr. Palaeoclimatol. Palaeoecol. 241, 457–491.

Tütken, T., Vennemann, T., 2009. Stable isotope ecology of Miocene large mammals from Sandelzhausen, southern Germany. Palaontologische Zeitschrift 83, 207–226.

Uechi, Y., Uemura, R., 2019. Dominant influence of the humidity in the moisture source region on the $^{17}O_{excess}$ in precipitation on a subtropical island. Earth Planet. Sci. Lett. 513, 20–28.

Urey, H.C., Lowenstam, H. a., Epstein, S., McKinney, C.R., 1951. Measurement of Paleotemperatures and Temperatures and the Southeastern United States. Bull. Geol. Soc. Am. 62, 399–416.

Veizer, J., Godderis, Y., François, L.M., 2000. Evidence for decoupling of atmospheric CO_2 and global climate during the Phanerozoic eon. Nature 408, 698–701.

Vennemann T. W., Fricke H. C., Blake R. E., O'Neil J. R., Colman A., 2002. Oxygen isotope analysis of phosphates: A comparison of techniques for analysis of Ag_3PO_4. Chem. Geol. 185, 321–336.

Voigt, C., Herwartz, D., Dorador, C., Staubwasser, M., 2021. Triple oxygen isotope systematics of evaporation and mixing processes in a dynamic desert lake system. Hydrol. Earth Syst. Sci. 25, 1211–1228.

Wacker, U., Rutz, T., Löffler, N., Conrad, A.C., Tütken, T., Böttcher, M.E., Fiebig, J., 2016. Clumped isotope thermometry of carbonate-bearing apatite: Revised sample pre-treatment, acid digestion, and temperature calibration. Chem. Geol. 443, 97–110.

Wallach, A.D., Inbar, M., Scantlebury, M., Speakman, J.R., Shanas, U., 2007. Water requirements as a bottleneck in the reintroduction of European roe deer to the southern edge of its range. Can. J. Zool. 85, 1182–1192.

Wong, W.W., Cochran, W.J., Klish, W.J., O'Brian Smith, E., Lee, L.S., Klein, P.D., 1988. In vivo isotope-fractionation factors and the measurement of deuterium- and oxygen-18-dilution spaces from plasma, urine, saliva, respiratory water vapor, and carbon dioxide. Am. J. Clin. Nutr. 47, 1–6.

Wostbrock J. A. G., Cano, E. J. and Sharp, Z. D., 2020. An internally consistent triple oxygen isotope calibration of standards for silicates, carbonates and air relative to VSMOW2 and SLAP2. Chem. Geol. 533, 119432.

Yakir, D., 1992. Variations in the natural abundance of oxygen-18 and deuterium in plant carbohydrates. Plant. Cell Environ. 15, 1005–1020.

Yeung, L.Y., Hayles, J.A., Hu, H., Ash, J.L., Sun, T., 2018. Scale distortion from pressure baselines as a source of inaccuracy in triple-isotope measurements. Rapid Commun. Mass Spectrom. 32, 1811–1821.

Young, E.D., Galy, A., Nagahara, H., 2002. Kinetic and equilibrium mass-dependent isotope fractionation laws in nature and their geochemical and cosmochemical significance. Geochim. Cosmochim. Acta 66, 1095–1104.

Young, E.D., Yeung, L.Y., Kohl, I.E., 2014. On the $\delta^{17}O$ budget of atmospheric O_2. Geochim. Cosmochim. Acta 135, 102–125.

Yung, Y.L., W.B., D., Pinto, J.P., 1991. isotopic exchange between carbon dioxide and ozong via O(1D) in the stratosphere. Geophys. Res. Lett. 18, 13–16.

Chapter 4 Triple oxygen based reconstruction of Mesozoic atmospheric CO$_2$ concentrations from dinosaur tooth enamel

Dingsu Feng, Thomas Tütken, Niklas Löffler, Gert Tröster, Gisa Heinemann & Andreas Pack, 2022. This work will be submitted to *Proceedings of the National Academy of Sciences of the United States of America*.

Abstract

This study showcases the potential of triple oxygen-based (Δ'^{17}O) reconstruction of atmospheric CO$_2$ concentrations (pCO$_2$). Nine modern bird species ranging from 0.23 to 145 kg and seven Mesozoic dinosaur taxa with estimated body masses of 750 to 40,000 kg are analyzed for their triple oxygen isotope composition of the phosphate group in bioapatite from bone (birds) and tooth enamel (dinosaurs) using a recently developed analytical technique that bases on the liberation of O$_2$ from bioapatite by means of laser fluorination and high-precision gas source mass spectrometry.

It is demonstrated that modern bird bone Δ'^{17}O values plot in line with previously published data that define the dependencies of Δ'^{17}O vs. δ^{18}O$_{PO4}$ for a wide body mass range of modern terrestrial vertebrates. This allows for the application of taxon specific oxygen mass balance models to the Mesozoic dinosaur data to approximate the isotopic compositions of a variety of oxygen in and outfluxes including inhaled air O$_2$ – which is dependent on atmospheric pCO$_2$ – and gross primary production (*GPP*). The results collectively verify the applicability of triple oxygen isotope analysis of oxygen bound to the phosphate group (PO$_4^{3-}$) of bioapatite for paleo pCO$_2$ reconstruction. From tooth enamel of dinosaurs, we reconstruct the Late Cretaceous atmospheric pCO$_2$ to 817 ± 579 ppmv and the Late Jurassic pCO$_2$ to 1605 ± 934 ppmv.

1   Introduction

Atmospheric carbon dioxide plays an important role in global climate throughout Earth's history. Arrhenius (1896) first discussed that variations in atmospheric CO$_2$ concentrations can be related to climate variability. A close correlation between atmospheric CO$_2$ partial pressure (pCO$_2$) is well-established for the past ~ 800 ka from ice core data (Foster et al., 2017; Lüthi et al., 2008; Petit et al., 1999). Atmospheric CO$_2$ levels are estimated from mass balance models (GEOCRAB, Berner, 2006a, 2006b) or geological proxies (Breecker et al., 2010; Gabriela et al., 2011; Kürschner et al., 2008; Lowenstein and Demicco, 2006; Pagani et

al., 2005; Pearson et al., 2009; Roth-Nebelsick, 2005; Royer, 2006; Royer et al., 2001; Retallack, 2001), such as paleosols, phytoplankton, stomata, marine baron and calcium, liverworts and nahcolite. These proxies are associated with unavoidable analytical uncertainties and individual limitations. This highlights the importance of developing additional pCO_2 proxies to further increase the precision of reconstructed pCO_2, *e.g.* by a multiproxy approach.

Bao et al. (2008) reconstructed a high pCO_2 level of ~ 12,000 ppm during the Early Cambrian (750 Ma) through sulphate and suggested that the sulphate $\Delta'^{17}O$ record can be used to evaluate extreme levels of atmospheric CO_2 or O_2 throughout Earth's history. Pack et al. (2013) then moved to another analyte and reconstructed pCO_2 through bioapatite from Eocene to Miocene. Feng et al. (2022a) developed a high-precision $\Delta'^{17}O$ technique for the analysis of bioapatite and presented that marine vertebrate bioapatite is a valuable new proxy for animal physiology opening new research avenues. In this study, we present high precision oxygen isotope data obtained from dinosaur tooth enamel and explore the pCO_2 concentration during the Late Cretaceous (66 to 83 Ma) and Late Jurassic (145 to 163 Ma).

2   Materials and Methods

2.1   Definitions

Variations in oxygen isotope ratios are reported in the conventional $\delta^{17}O$ (Eq. 1) and $\delta^{18}O$ (Eq. 2) notation as:

$$\delta^{17}O^{sample}_{VSMOW2} = 1000 \times \left(\frac{\left(^{17}O/^{16}O\right)_{sample}}{\left(^{17}O/^{16}O\right)_{VSMOW2}} - 1 \right) \qquad \text{Eq. 1}$$

$$\delta^{18}O^{sample}_{VSMOW2} = 1000 \times \left(\frac{\left(^{18}O/^{16}O\right)_{sample}}{\left(^{18}O/^{16}O\right)_{VSMOW2}} - 1 \right) \qquad \text{Eq. 2}$$

VSMOW2 denotes the international reference material Vienna Standard Mean Ocean Water 2. The linearized forms of the δ-notations $\delta'^{17}O$ (Eq. 3) and $\delta'^{18}O$ (Eq. 4) (Hulston and Thode, 1965; Young et al., 2002) are defined as:

$$\delta'^{17}O^{sample}_{VSMOW2} = 1000 \times \ln\left(\frac{\delta^{17}O^{sample}_{VSMOW2}}{1000} + 1 \right) \qquad \text{Eq. 3}$$

$$\delta'^{18}O^{sample}_{VSMOW2} = 1000 \times \ln\left(\frac{\delta^{18}O^{sample}_{VSMOW2}}{1000} + 1 \right) \qquad \text{Eq. 11}$$

Oxygen isotope anomalies are expressed with the $\Delta'^{17}O$ (Eq. 5) notation. In a $\delta'^{17}O$ vs. $\delta'^{18}O$ space, $\Delta'^{17}O$ is defined by the deviation of a sample in $\delta'^{17}O$ from a given reference line (RL) with a particular slope (λ_{RL}) as follows:

$$\Delta'^{17}O_{0.528} = \delta'^{17}O^{sample}_{VSMOW2} - \lambda_{RL} \times \delta'^{18}O^{sample}_{VSMOW2} \qquad \text{Eq. 12}$$

In this study, a λ_{RL} of 0.528 is applied.

2.2 Materials

In this study, oxygen isotopes of 11 modern bird (Aves) bones and tooth enamel of 9 dinosaur specimens are analyzed. A detailed overviews on the sample information are presented in Table 1. All samples were treated with 2% NaClO for 45 minutes and 0.1% CH_3COOH for 15 minutes, then rinsed with distilled water 5 times for each step and dried overnight at 70 °C (Lee-Thorp et al., 2007) before the analysis.

1 Table 1: List of all samples that were analysed for their triple oxygen isotopic composition.

Sample	Taxon	Common name	body mass (M_b, kg)	Material	Age	Further information	Bone type	Ontogenetic age, sex	Country	Museum
B01	*Phasianidae*	pheasant	0.23…2.75[a]	bone	modern	–	skull	–	Germany	
B02	*Strix aluco*	tawny owl	0.325…0.716[b]	bone	modern	–	skull	–	Germany	
B03	*Anodorhynchus hyacinthinus*	hyacinth macaw	1.2…1.7[c]	bone	modern	–	skull	–	Germany	
B04	*Ardea cinerea*	grey heron	1.02…2.08[d]	bone	modern	–	skull	–	Germany	
B05	*Threskiornis aethiopicus*	African sacred ibis	1.50…3.30[d]	bone	modern	–	skull	–	Africa	Zoologisches Museum of the University of Göttingen, Germany
B06	*Leptoptilos*	marabou stork	4…8.9[e]	bone	modern	–	skull	–	Africa	
B07	*Casuarius casuarius*	southern cassowary	17…70[f]	bone	modern	–	skull	–	Africa	
B08	*Struthio camelus*	ostrich	86…145[d]	bone	modern	livestock	skull	–	Germany	
B09	*Ciconia ciconia*	white stork	2.2…4.4[g]	bone	modern	–	skull	–	Germany	
B10	*Ardea cinerea*	grey heron	1.02…2.08[d]	bone	modern	–	skull	–	Germany	
B16	*Struthio camelus*	ostrich	86…145[d]	bone	modern	livestock from Gemarkenhof, Remagen	femur	adult, male	Germany	–

Sample	Taxon	Common name	body mass (M_b, kg)	Material	Age	Site	Formation	Layer	Country	Museum	Collection number
F11	*Tyrannosaurus rex*	tyranosaur	5580…9940[h]	enamel	Late Cretaceous, Maastrichtian	Greaswood Ridge	Lance Formation	bonebed	U.S.A.	Senckenberg Museum für Naturkunde, Frankfurt, Germany	–
F21	*Tyrannosaurus rex*	tyranosaur	5000[i]	enamel	Late Cretaceous, Maastrichtian	South of Jordan, Montana	Hell Creek Formation	Top of formation, below K-Pg boundary	U.S.A.	Schulp A.S.	RGM 792.000
F24	*Theropod* sp.	theropod	1685[j]	enamel	Late Cretaceous, late Maastrichtian	Knob Microsite	Scollard Formation	Base of formation	Canada	Tyrell Museum, Drumheller, Canada	2010 J.23
F26	*Albertosaurus sarcophagus*	albertosaur	762…2500[k]	enamel	Late Cretaceous, late Campanian	Southern Alberta, Montana	Horseshoe Canyon Formation	Albertosaurus bonebed	Canada	Tyrrell Museum, Drumheller, Canada	93.31.145-7
F40	*Diplodocus* sp.	sauropod	16000[l]	enamel	Late Jurassic, Kimmeridgian to Tithonian	Howe Ranch, Wyoming	Morrison Formation	–	U.S.A.	Dinosaurier Museum Aathal, Aathal, Switzerland	–
F27	*Europasaurus holgeri*	sauropod	750[m]	enamel	Late Jurassic, middle Kimmeridgian	Oker Langenberg, Harz	Süntel Formation	Europasaurus bonebed	Germany	Dinosaurier-Park Münchehagen, Germany	–
F30	*Giraffatitan brancai*	sauropod	40000[m]	enamel	Late Jurassic, late Kimmeridgian to Tithonian	Tendaguru	Tendaguru Formation	Middle or Upper Dinosaur Member	Tanzania	Museum für Naturkunde Berlin, Germany	MB.R.3381
F36	*Sauropod* sp.	sauropod	2600…20600[l]	enamel	Late Jurassic, late Kimmeridgian to Tithonian	Tendaguru	Tendaguru Formation	Transition Indotrigonia africana Member to Upper Dinosaur Member	Tanzania	Museum für Naturkunde Berlin, Germany	MB.R.2136
F38	*Sauropod* sp.	sauropod	2600…20600[l]	enamel	Late Jurassic, late Kimmeridgian	Tendaguru	Tendaguru Formation	Middle Dinosaur Member	Tanzania	Museum für Naturkunde Berlin, Germany	MB.R.2127 1-3

–: unknown.

a: Dunning Jr (2007), b: König and Weick (2008), c: Hagen (2004), d: Cramp and Perrins (1992), e: Hancock et al. (1992), f: Burnie and Wilson (2005), g: Cramp and Perrins (1992); Hancock et al. (1992), h: Bates et al. (2009); Hutchinson et al. (2011), i: Löffler et al. (2020), j: Christiansen and Fariña (2004), k: Erickson et al. (2004); Paul (2013), l: Mazzetta et al. (2004), m: Paul (2013).

2

2.3 Oxygen isotope analyses

2.3.1 Carbon and Oxygen isotope analyses of the bioapatite carbonate group

The bulk carbon ($\delta^{13}C$) and oxygen ($\delta^{18}O_{CO3}$) isotopic compositions were analyzed on a Thermo Finnigan Delta Plus gas source mass spectrometer in dual inlet mode at the stable isotope laboratory of the Geoscience Center at the University of Göttingen, Germany. Details on the analytical systems and protocols are provided in Gehler et al. (2012), Sisma-Ventura et al. (2019), and Feng et al. (2022b).

2.3.2 Laser fluorination triple oxygen isotope analyses

The triple oxygen isotope analyses were conducted by laser fluorination (LF) in combination with multi collector isotope ratio gas source mass spectrometry (IRMS) (Sharp, 1990). Details on this specific setup are provided in Pack et al. (2016) and Feng et al. (2022a). Briefly, after the chemical pretreatment, samples were heated under 10% H_2 mixed with 90% N_2 atmosphere to 1000 °C for 30 minutes in a furnace to remove residual organic material as well as carbonate and hydroxyl groups. Approximately 2.5 mg preheated samples were loaded into a polished Ni metal sample holder with 14 pits, along with the AG-Lox and San Carlos Olivine reference materials. The $\delta^{18}O$ of all samples were normalized to San Carlos Olivine with $\delta^{18}O = 5.3‰$ and $\Delta'^{17}O_{0.528} = -52$ ppm (Pack et al., 2016; Sharp et al., 2016; Wostbrock et al., 2020). The uncertainties of the internal reference material AG-Lox were $\pm0.63‰$ for $\delta^{18}O$ and ± 11 ppm for $\Delta'^{17}O$ (1 σ SD). Data on apatite originating from the laser fluorination line are presented as $\delta^{17}O_{AP}$, $\delta^{18}O_{AP}$, and $\Delta'^{17}O_{AP}$, i.e., with the subscript "AP" for apatite, and are listed in tables 2 and 3.

2.3.3 Measurement of $\delta^{18}O_{PO4}$ of bioapatite phosphate oxygen by thermal combustion elemental analyzer (TC/EA)

The phosphate fraction of the chemically pretreated samples was precipitated as silver phosphate (Ag_3PO_4) independently constrain $\delta^{18}O_{PO4}$ and verify the laser fluorination results. Ag_3PO_4 was analyzed by means of high temperature reduction using a Thermo Finnigan TC/EA coupled via a ConFlo IV to a Micromass 100 GC-IRMS (Micromass UK Ltd, Manchester, United Kingdom) or a Delta V Plus at the stable isotope center in the Forest Faculty of University of Göttingen, Germany. Details on the precipitation procedure can be found in Dettman et al. (2001), Tütken et al. (2006) and Feng et al. (2022a).

2.3.4   Combining laser fluorination $\Delta'^{17}O_{AP}$ with $\delta^{18}O_{PO4}$ from TC/EA

The $\delta^{18}O_{PO4}$ from TC/EA are combined with the $\Delta'^{17}O_{AP}$ from laser fluorination due to an observed constant offset between the $\delta^{18}O_{PO4}$ from both methods: The $\delta^{18}O_{AP}$ from laser fluorination is typically ~2.5‰ lower than that from TC/EA (long-term value; this study: 1.95 ±1.20‰), which is attributed to possible fractionation processes between liberated O_2 and residual fluorides during laser fluorination. Even though this potential process would alter the absolute $\delta^{18}O_{PO4}$ and $\delta^{17}O_{PO4}$ values, the effect on $\Delta'^{17}O_{AP}$ would be strongly limited if one assumes similar fractionation factors for ^{18}O and ^{17}O as $\Delta'^{17}O$ refers to a difference of these values.

3   Results

3.1   Birds

The birds' oxygen isotope data are listed in Table 2 and illustrated in Figure 1. The average $\delta^{18}O_{PO4}$ range from 12.2 to 23.3‰ and the $\Delta'^{17}O_{AP}$ range from -182 to -112 ppm.

Table 2: List of oxygen isotope data (individual measurements and means) of bone of birds. The $\delta^{18}O_{AP}$ and $\Delta'^{17}O_{AP}$ values were obtained by laser fluorination and $\delta^{18}O_{PO4}$ by using a temperature conversion elemental analyzer (TC/EA). The uncertainty in $\Delta'^{17}O_{AP}$ is 0.011‰ (1σ SD). The ID refers to the internal measurement identification number.

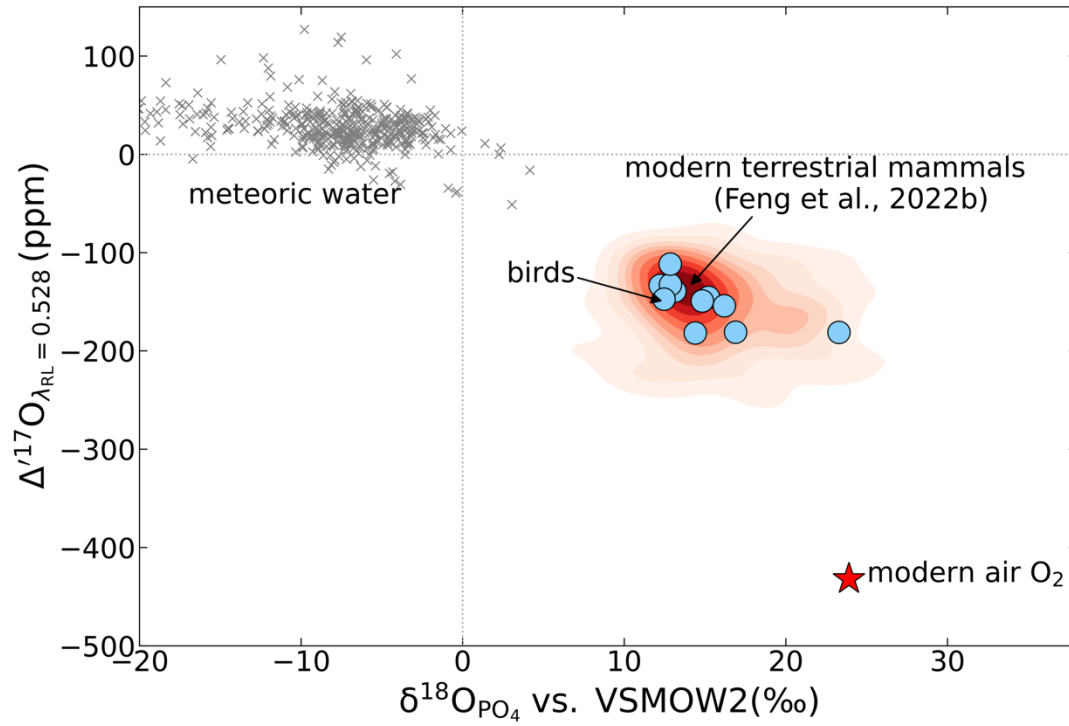| Sample Slope	ID	$\delta^{18}O_{AP}$ (‰)	$\Delta'^{17}O_{AP}$ (ppm) 0.528	$\delta^{18}O_{PO4}$ (‰)	Sample Slope	ID	$\delta^{18}O_{AP}$ (‰)	$\Delta'^{17}O_{AP}$ (ppm) 0.528	$\delta^{18}O_{PO4}$ (‰)
		pheasant					marabou stork		
	10028	8.699	-124			10064	15.186	-147	
B01	10003	10.804	-153		B06	10018	13.830	-164	
	10313	11.527	-124			10320	13.291	-151	
	average	10.343	-133	12.2		average	14.102	-154	16.2
		tawny owl					southern cassowary		
	10063	12.669	-178			10066	12.276	-135	
B02	10004	12.417	-185		B07	10019	12.236	-136	
	10315	12.082	-182			10321	12.711	-127	
	average	12.389	-182	14.4		average	12.407	-133	12.9
		hyacinth macaw					ostrich		
	10060	14.728	-170			10021	13.064	-139	
B03	10167	14.401	-194		B08	10171	13.614	-154	
	10316	14.578	-178			10322	13.690	-148	
	average	14.569	-181	16.9		average	13.456	-147	12.5
		grey heron					white stork		
	10061	13.394	-133			10022	19.886	-179	
B04	10169	12.578	-138		B09	10173	19.326	-193	
	10318	13.374	-146			10587	19.216	-172	
	average	13.115	-139	13.1		average	19.476	-181	23.3
		African sacred ibis					grey heron		
	10062	14.995	-137			10024	11.880	-112	
B05	10170	14.431	-145		B10	10174	11.117	-105	
	10319	14.195	-154			10588	10.751	-118	
	average	14.541	-145	15.2		average	11.249	-112	12.8
							ostrich		
						10473	13.783	-146	
					B16	10604	12.841	-152	
						average	13.312	-149	14.8

Figure 1: Overview on the bioapatite $\delta^{18}O_{PO4}$ and $\Delta'^{17}O_{AP}$ data of birds. Blue points: birds, red shaded area: modern terrestrial mammals (Feng et al., 2022b), grey crosses: meteoric water, and red asterisk: modern air O_2 (Pack, 2021).

3.2 Dinosaurs

The dinosaur oxygen isotope data are listed in Table 3 and illustrated in Figure 2 and 3. For the Late Cretaceous dinosaurs, the $\delta^{13}C$ ranges from -8.73 to -6.15‰ and the $\delta^{18}O_{CO3}$ ranges from 15.40 to 20.35‰. The $\delta^{18}O_{PO4}$ ranges from 9.8 to 20.8‰ and the average $\Delta'^{17}O_{AP}$ ranges from -232 to -151 ppm, as shown in Figure 2. For the Late Jurassic dinosaurs, the $\delta^{13}C$ ranges from -9.19 to -3.54‰ and the $\delta^{18}O_{CO3}$ ranges from 26.14 to 32.85‰. The $\delta^{18}O_{PO4}$ ranges from 20.1 to 23.1‰ and the average $\Delta'^{17}O_{AP}$ ranges from -291 to -176 ppm, as showed in Figure 3.

Table 3: List of oxygen isotope data (individual measurements and means) of tooth enamel of dinosaurs. The $\delta^{18}O_{AP}$ and $\Delta'^{17}O_{AP}$ values were obtained by laser fluorination and $\delta^{18}O_{PO4}$ by

using a temperature conversion elemental analyzer (TC/EA). The uncertainty in $\Delta'^{17}O_{AP}$ is 0.011‰ (1σ SD). The ID refers to the internal measurement identification number.

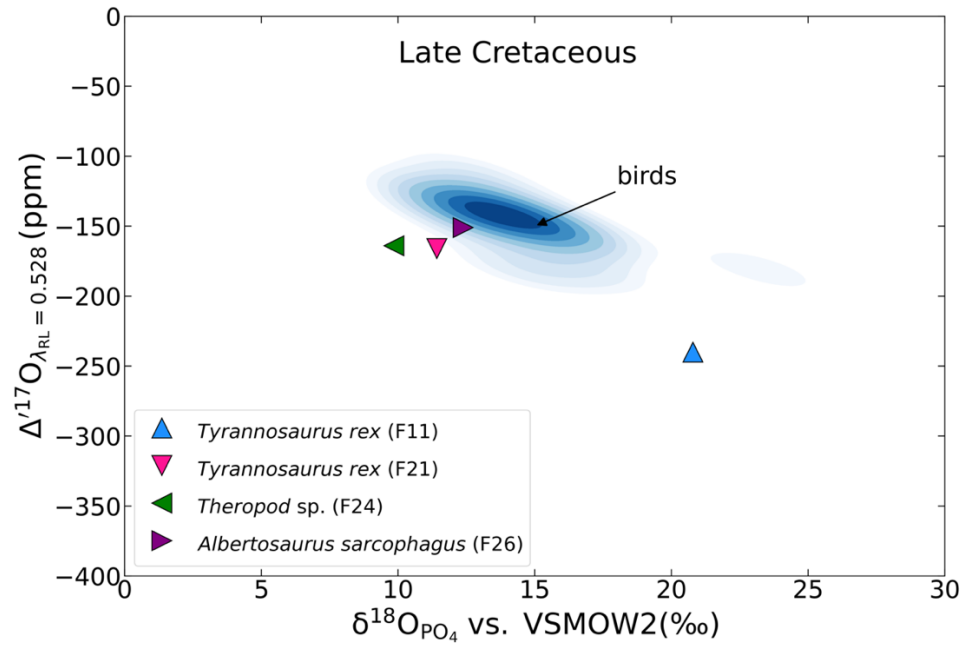| Sample	ID	$\delta^{13}C$ (‰)	$\delta^{18}O_{CO3}$ (‰)	$\delta^{18}O_{AP}$ (‰)	$\Delta'^{17}O_{AP}$ (ppm)	$\delta^{18}O_{PO4}$ (‰)	pCO_2 (ppmv)
Slope					0.528		$GPP_t/GPP_0 = 1$
				Tyrannosaurus rex			
	10081			18.183	-229		
F11	10184			18.146	-234		
	average	-7.94	20.35	18.164	-232	20.8	1665 ± 530
				Tyrannosaurus rex			
	10288			8.865	-175		
F21	10285			9.167	-157		
	average	-8.73	20.07	9.016	-166	11.4	667 ± 210
				Theropod sp.			
F24	10386	-6.15	15.40	7.046	-164	9.8	568 ± 100
				Albertosaurus sarcophagus			
F26	10452	-6.95	19.53	10.687	-151	12.4	368 ± 100
						average (1σ, SD)	817 ± 579
				Diplodocus sp.			
	10438			17.701	-285		
F40	10526			18.925	-298		
	average	-6.24	26.14	18.313	-291	22.1	3260 ± 550
				Europasaurus holgeri			
	10442			18.445	-215		
F27	10524			19.358	-205		
	average	-3.54	32.85	18.901	-210	21.1	967 ± 100
				Giraffatitan brancai			
	10689			16.756	-173		
F30	10688			16.922	-178		
	average	-8.85	27.13	16.839	-176	20.1	1266 ± 390
				Sauropod sp.			
	10485			20.786	-196		
F36	10542			20.294	-198		
	average	-9.19	29.18	20.540	-197	23.1	1266 ± 250
				Sauropod sp.			
	10489			17.904	-193		
F38	10543			22.036	-191		
	average	-8.90	28.87	19.970	-192	22.4	1266 ± 200
						average (1σ, SD)	1605 ± 934

Figure 2: Overview on the bioapatite $\delta^{18}O_{PO4}$ and $\Delta'^{17}O_{AP}$ data from Late Cretaceous dinosaur tooth enamel. Blue triangle pointing upwards: *Tyrannosaurus rex* (F11), pink triangle pointing downwards: *Tyrannosaurus rex* (F21), green triangle pointing left: *Theropod* sp. (F24), purple triangle pointing right: *Albertosaurus sarcophagus* (F26). Blue shaded area: Modern birds.
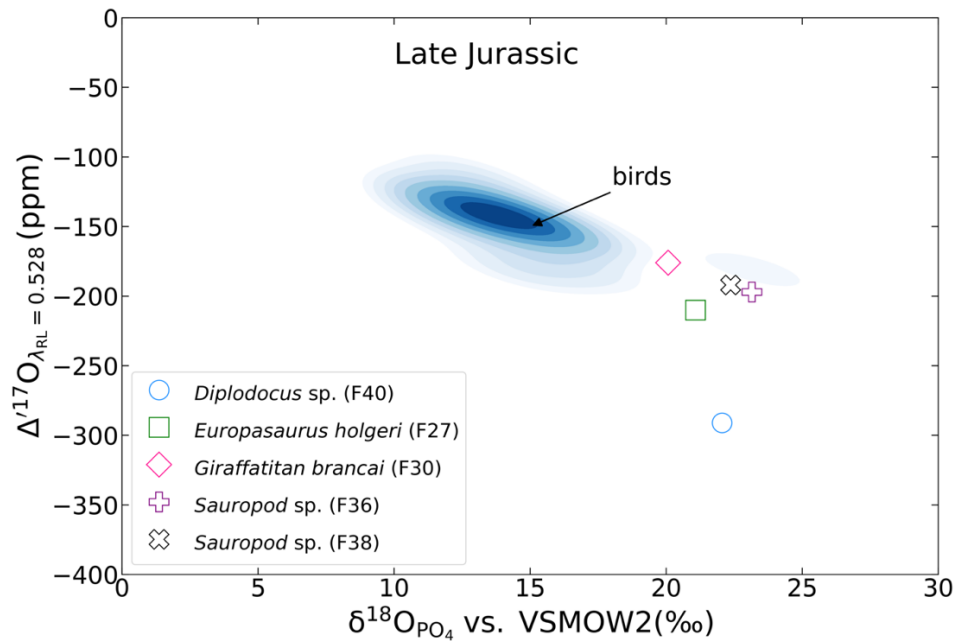

Figure 3: Overview on the bioapatite $\delta^{18}O_{PO4}$ and $\Delta'^{17}O_{AP}$ data from Late Jurassic dinosaur tooth enamel. Blue circle: *Diplodocus* sp. (F40), green square: *Europasaurus holgeri* (F27), pink diamond: *Giraffatitan brancai.* (F30), purple cross: *Sauropod* sp. (F36), black X: *Sauropod* sp. (F38). Blue shaded area: Birds.

4 Discussion

4.1 Comparison of birds to modern terrestrial mammals

As illustrated in Figure 1, $\Delta'^{17}O$ of birds plot in the same range of terrestrial mammals (Feng et al. 2022b) even though birds have similar or higher metabolic rates when compared to terrestrial mammals with identical body masses and food habits (Mcnab, 1988). Because birds, besides reptiles, are interpreted as one of the closest present-day analogues of dinosaurs (Hicks and Farmer, 1999; Ji et al., 1996), the close agreement of our modern bird and terrestrial mammal data allows – in a first approximation – for the application of the established oxygen mass balance models from modern taxa (Feng et al., 2022b) to the dinosaur data. The mass balance model (Feng et al. 2022b) predicts that the $\Delta'^{17}O$ of bioapatite decreases with decreasing M_b and with decreasing air $\Delta'^{17}O_{air\,O2}$.

4.2 Preservation of primary isotopic signatures

Fossil tooth enamel was used to approximate the animal body water from $\Delta'^{17}O$ values because tooth enamel is widely thought to be more resistant to diagenetic alteration than dentine or bone (Fricke et al., 1998; Kohn et al., 1999; Kohn and Cerling, 2002; Kolodny et al., 1983; Luz et al., 1984; Shemesh et al., 1983). Because of the strength of P-O bounds, the phosphate group is less prone to isotopic exchange during diagenesis than the carbonate group. Thus PO_4 is preferred for most bioapatite-based applications when dealing with fossil material (Kohn and Cerling, 2002). Eagle et al. (2011) showed a variety of approaches to study the preservation of stable isotope signatures in fossil bioapatite, including the examination of offsets between $\delta^{18}O_{CO3}$ and $\delta^{18}O_{PO4}$ ($\Delta^{18}O_{CO3-PO4}$). Well preserved bioapatite generally shows a consistent $\Delta^{18}O_{CO3-PO4}$ offset of 7.5 to 11.4‰ (Chenery et al.,2012; Gehler et al., 2012) which is confirmed by the data from terrestrial mammals from Feng et al. (2022) (Figure 4, green shaded area), which average to 9.54 ± 3.02‰ (n=96; figure 4, dashed black line. However, if such an offset is out of the 7.5 to 11.4‰ range, this can also be due to an isotopic alteration of the carbonate group, while the phosphate group remains (largely) unaltered.

Eagle et al. (2011) discussed that the variation of offset between $\delta^{18}O_{CO3}$ and $\delta^{18}O_{PO4}$ limits the definition of strict cut off points for acceptable $\delta^{18}O_{CO3}$ - $\delta^{18}O_{PO4}$ values. Based on a statistical definition of confidence intervals of the modern distribution of offsets as shown in Feng et al. (2022b), when both PO_4 and CO_3 are heavily altered, it is also possible that

$\Delta^{18}O_{CO3-PO4}$ values, by coincidence, fall into the modern range while the pristine isotopic information is overprinted. However, from Figure 4, we can see that *Tyrannosaurus rex* (F11), *Theropod* sp. (F24, 2010 J.23), *Diplodocus* sp. (F40), and two *Sauropod* sp. (F36; MB.R.2136, F38; MB.R.2127 1-3) fall away from the modern terrestrial mammal range. *Tyrannosaurus rex* (F21; RGM 792.000), *Albertosaurus sarcophagus* (F26; 93.31.145-7), *Europasaurus holgeri* (F27), and *Giraffatitan brancai* (F30; MB.R.3381) fall within or close to the modern terrestrial mammal range. This implies that the CO_3 isotopic composition of one *Tyrannosaurus rex* (F11), *Theropod* sp., *Diplodocus* sp. and two *Sauropod* sp. could have been exposed to diagenetic alteration, e.g. by oxygen isotopic exchange with fluids which led to decreasing $\delta^{18}O_{CO3}$. For the second *Tyrannosaurus rex* (F21), *Albertosaurus sarcophagus* (F26), *Europasaurus holgeri* (F27), and *Giraffatitan brancai* (F30), the impact of isotopic exchange seems rather small. Hence the $\delta^{18}O_{CO3}$ of those four dinosaurs most likely carry pristine PO_4 isotopic signatures. The $\delta^{18}O_{PO4}$ values of *Tyrannosaurus rex* (F11), *Diplodocus* sp. (F40), *Europasaurus holgeri* (F27), *Giraffatitan brancai.* (F30), *Sauropod* sp. (F36) and *Sauropod* sp. (F38), are over 20‰, a value that presently can be measured on terrestrial mammals from Africa (e.g. Feng et al., 2022b). When diagenetic alteration at shallow depths takes place, the $\delta^{18}O$ of a sample likely exchanges with the $\delta^{18}O$ of a fluid, that feeds from meteoric water (Figure 1, grey crosses), but which can also be altered by fluid-rock interactions. As for *Tyrannosaurus rex* (F21), *Albertosaurus* sarcophagus (F26), and the *Europasaurus holgeri* (F27), and *Giraffatitan brancai* (F30), PO_4 are interpreted to be unaltered because the $\Delta^{18}O_{CO3-PO4}$ offsets are, within error, in the expected range (8.6, 7.1, 11.8, and 7.1‰, respectively). All other dinosaur samples show lower $\Delta^{18}O_{CO3-PO4}$ (-0.4 to 6.5‰). While the absolute range of all dinosaur $\delta^{18}O_{CO3}$ (27.1‰) is 9.7‰ larger when compared to the respective range of modern terrestrial mammals (17.4‰; derived from Feng et al., 2022b; their table S1), their range in $\delta^{18}O_{PO4}$ of 22.4‰ is comparable to the modern range which is derived from taxa that cover a variety of habitats with distinct climates (21.1‰; derived from Feng et al., 2022b; their table S1) (Figure 4). This implies that there is a high chance that the dinosaur $\delta^{18}O_{PO4}$ are still preserved isotopically unaltered, even though the $\delta^{18}O_{CO3}$ are not – provided that the formation of dinosaur teeth and associated fractionation processes where similarly uniform as for terrestrial mammals.

Future analysis of the samples with e.g. Raman spectroscopy (Thomas et al., 2011) or XRD and FTIR (Li and Pasteris, 2014) could help to further assess the extent of alteration.
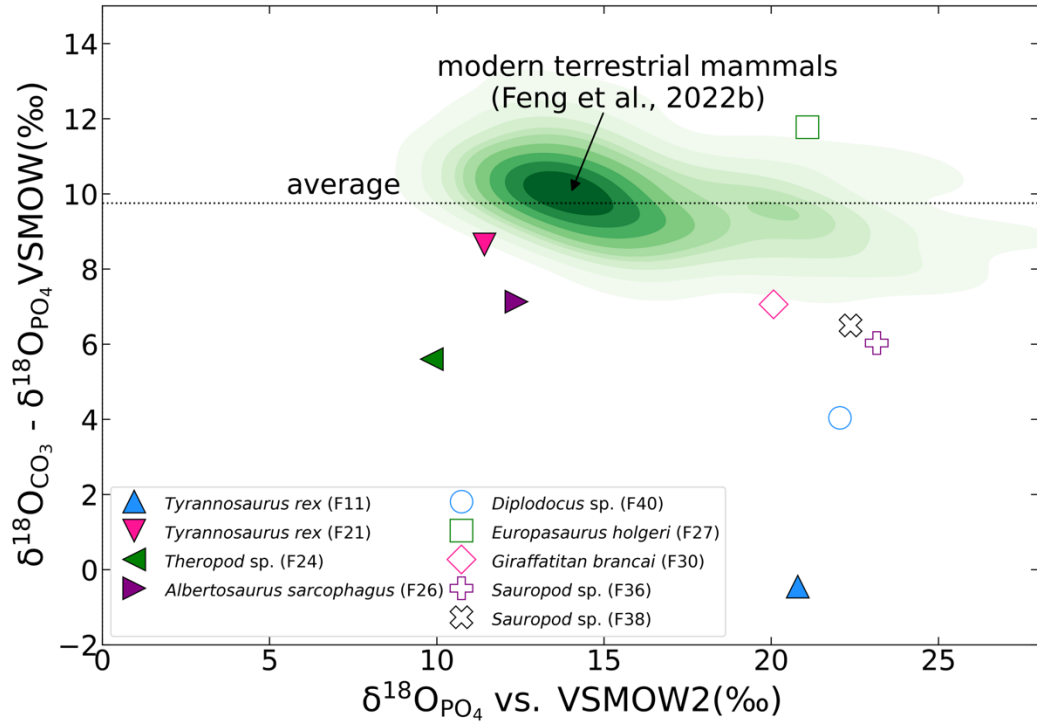
Figure 4: Overview on the bioapatite $\delta^{18}O_{PO4}$ and $\Delta'^{17}O$ data of Late Jurassic dinosaurs. Blue triangle pointing upwards: *Tyrannosaurus rex* (F11), pink triangle pointing downwards: *Tyrannosaurus rex* (F21), green triangle pointing left: *Theropod* sp. (F24), purple triangle pointing right: *Albertosaurus sarcophagus* (F26), blue circle: *Diplodocus* sp. (F40), green square: *Europasaurus holgeri* (F27), pink diamond: *Giraffatitan brancai.* (F30), purple cross: *Sauropod* sp. (F36), black X: *Sauropod* sp. (F38). Green shaded area: terrestrial mammals (Feng et al. 2022b), black dashed line: average value from modern terrestrial mammals (Feng et al. 2022b).

4.3 $\Delta'^{17}O$ of tooth enamel as a paleo-CO₂ proxy

By running 42 taxon specific mass balance models (i.e. varying body masses), Feng et al. (2022b), showed that the sensitivity of bioapatite $\Delta'^{17}O$ from terrestrial mammals not only increases with decreasing body mass, but also with decreasing $\Delta'^{17}O_{air}$, as shown in Figure 5 and 6 (black solid curve with $\Delta'^{17}O_{air} = -0.432‰$).

We therefore tuned the $\Delta'^{17}O_{air}$ of the oxygen mass balance models to the $\Delta'^{17}O_{AP}$ data for each dinosaur sample and calculated average $\Delta'^{17}O_{air}$ values for both the Late Jurassic and Late Cretaceous to acknowledge potential populational variations that can be expected from individually varying behavior and physiology (comp. Feng et al. 2022b; their *Capreolus capreolus* dataset) and increase the statistical significance of the reconstructed pCO₂. When

$\Delta'^{17}O_{air}$ adjusted to -0.55‰ (ranging from -0.60‰ to -0.50‰), the measured $\Delta'^{17}O_{AP}$ from tooth enamel of *Albertosaurus sarcophagus* (F26) fits into the range (Figure 5, green solid curve). When $\Delta'^{17}O_{air}$ decreased to -0.65‰ (ranging from -0.70‰ to -0.60‰), *Theropod* sp. (F24) fits into the range (Figure 5, between purple solid curve and green solid curve) and when $\Delta'^{17}O_{air}$ decreased to -0.70‰ (ranging from -0.80‰ to -0.60‰), *Tyrannosaurus rex* (F21) fits into the range of the mass balance model (Figure 5, purple solid curve). For *Tyrannosaurus rex* (F11), when $\Delta'^{17}O_{air}$ decreased to -1.2‰ (ranging from -1.5‰ to -1.05‰), it fits into the range of the mass balance model (Figure 5, teal solid curve). Overall, the paleo air O_2 composition in the Late Cretaceous ranges from -1.5‰ to -0.5‰ and averages at -0.78 ± 0.29‰.
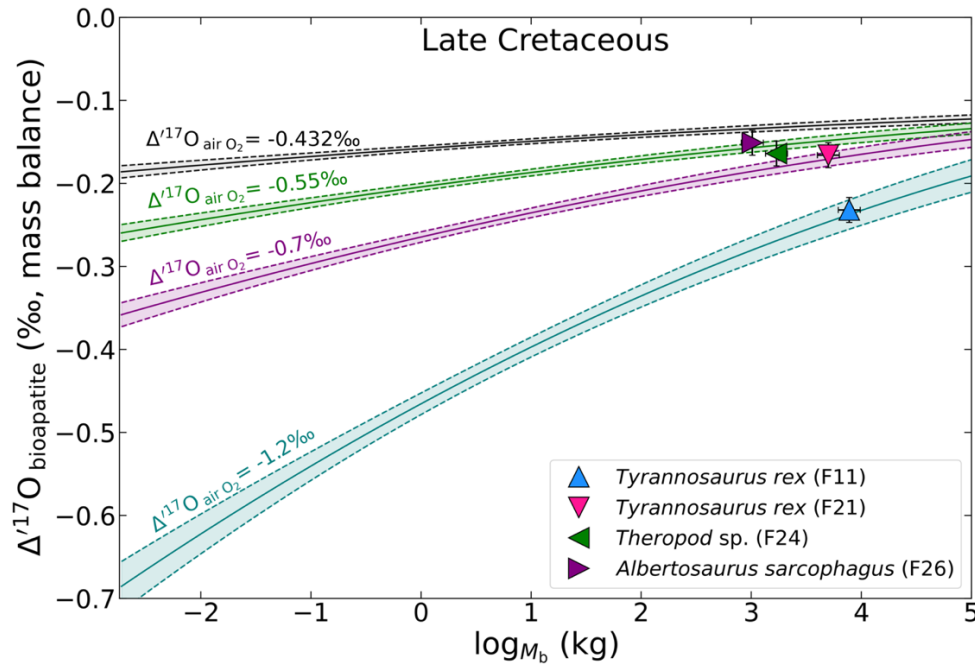

Figure 5: Plot of $\Delta'^{17}O$ of bioapatite (from mass balance models and measured tooth enamel data) vs. the logarithmic body mass with air O_2 $\Delta'^{17}O$ ($\Delta'^{17}O_{air\ O2}$) ranging from -1.2‰ to -0.432‰. Blue triangle pointing up: *Tyrannosaurus rex* (F11), pink triangle pointing down: *Tyrannosaurus rex* (F21), green triangle pointing left: *Theropod* sp. (F24), purple triangle pointing right: *Albertosaurus sarcophagus* (F26). Black star: average value. Black solid curve: $\Delta'^{17}O$ of bioapatite vs. the logarithmic body mass with air O_2 $\Delta'^{17}O$ = -0.432‰ (Feng et al. 2022b), green solid curve: $\Delta'^{17}O$ of bioapatite vs. the logarithmic body mass with air O_2 $\Delta'^{17}O$ = -0.55‰, purple solid curve: $\Delta'^{17}O$ of bioapatite vs. the logarithmic body mass with air O_2 $\Delta'^{17}O$ = -0.7‰, teal solid curve: $\Delta'^{17}O$ of bioapatite vs. the logarithmic body mass with air O_2 $\Delta'^{17}O$ = -1.2‰. Dashed lines: 1σ SD uncertainty.

When $\Delta'^{17}O_{air}$ decreased to -0.85‰ (ranging from -0.90‰ to -0.80‰), the measured $\Delta'^{17}O_{AP}$ from tooth enamel of *Europasaurus holgeri* (F27) fits into the range (Figure 6, blue violet solid curve). When $\Delta'^{17}O_{air}$ decreased to -1‰ (ranging from -1.2‰ to -0.9‰), *Giraffatitan brancai* (F30) fit into the range (Figure 6, blue solid curve) and when $\Delta'^{17}O_{air}$ decreased to -1‰ (ranging from -1.15‰ to -0.90‰), *Sauropod* sp. (F36) fit into the range of the mass balance model (Figure 6, blue solid curve). For *Sauropod* sp. (F38), when $\Delta'^{17}O_{air}$ decreased to -1.00‰ (ranging from -1.10‰ to -0.90‰), it fits to the range of the mass balance model (Figure 6, blue solid curve). For *Diplodocus* sp. (F40), when $\Delta'^{17}O_{air}$ decreased to -2.00‰ (ranging from -2.30‰ to -1.50‰), it fits into the range of the mass balance model (Figure 6, dark blue solid curve). Overall, the Late Jurassic (145 to 157 Ma) paleo air O_2 composition ranges from -2.3‰ to -0.9‰ and averages at -1.17 ± 0.47‰.
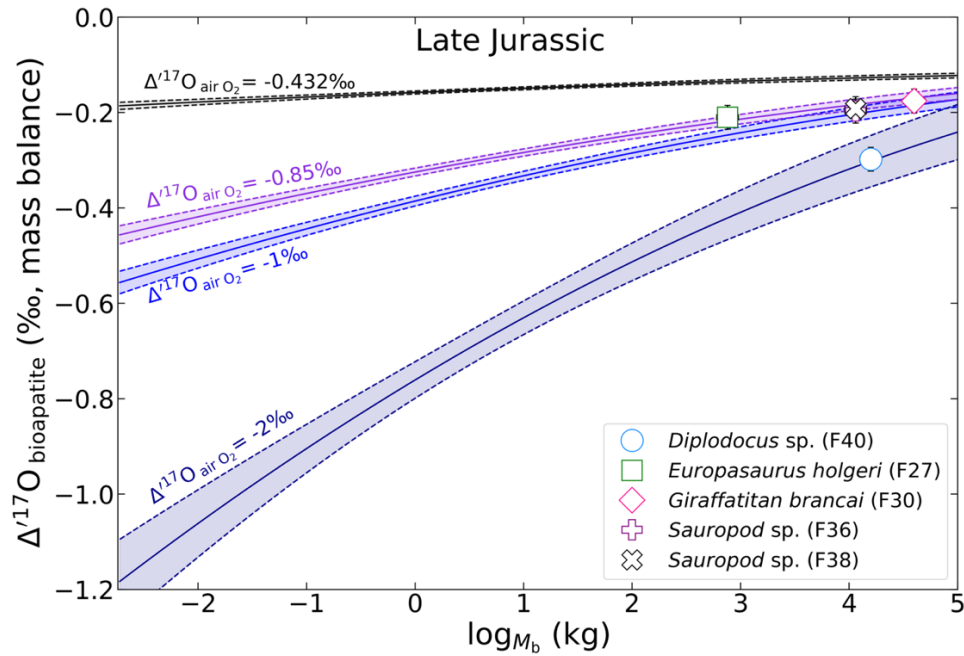

Figure 6: Plot of $\Delta'^{17}O$ of bioapatite (from mass balance models and measured tooth enamel data) vs. the logarithmic body mass with air O_2 $\Delta'^{17}O$ ($\Delta'^{17}O_{air\ O2}$) ranging from -2.00‰ to -0.432‰. Blue circle: *Diplodocus* sp. (F40), green square: *Europasaurus holgeri* (F27), pink diamond: *Giraffatitan brancai.* (F30), purple plus: *Sauropod* sp. (F36), black X: *Sauropod* sp. (F38). Grey star: average value. Black solid curve: $\Delta'^{17}O$ of bioapatite vs. the logarithmic body mass with air O_2 $\Delta'^{17}O$ = -0.432‰ (Feng et al. 2022b), blue violet solid curve: $\Delta'^{17}O$ of bioapatite vs. the logarithmic body mass with air O_2 $\Delta'^{17}O$ = -0.85‰, blue solid curve: $\Delta'^{17}O$ of bioapatite vs. the logarithmic body mass with air O_2 $\Delta'^{17}O$ = -1‰, dark blue solid curve: $\Delta'^{17}O$ of bioapatite vs. the logarithmic body mass with air O_2 $\Delta'^{17}O$ = -2‰. Dashed lines: 1σ SD uncertainty.

The relation of $\Delta'^{17}O$ of tropospheric O_2 and atmospheric CO_2 concentration has been explored by Bao et al. (2008) by investigating sulphate triple oxygen isotope compositions. As shown in Figure 7, $\Delta'^{17}O_{air\ O2}$ is related to pCO_2 and GPP (Luz et al., 1999; Bao et al., 2008; Figure 7). We calculated pCO_2 according to $GPP_t / GPP_0 = 0.67$, 1, and 1.5, where the subscript t denotes time before present and subscript 0 denotes present. With $GPP_t / GPP_0 = 1$, GPP is assumed to have been constant over the past 150 Ma.

Based on tooth enamel $\Delta'^{17}O_{AP}$, the estimated Late Cretaceous $\Delta'^{17}O_{air\ O2}$ ranges from -1.5‰ to -0.5‰ which is slightly lower as the estimated Late Jurassic $\Delta'^{17}O_{air\ O2}$ which range from -2.3‰ to -0.9‰. With $GPP_t / GPP_0 = 1$, the Late Cretaceous pCO_2 averages at 817 ± 579 ppmv (abs. range: 269 to 2263 ppmv) while the Late Jurassic pCO_2 averages at 1605 ± 934 ppmv (abs. range: 867 to 3859 ppmv) (Table 3, Figure 8).

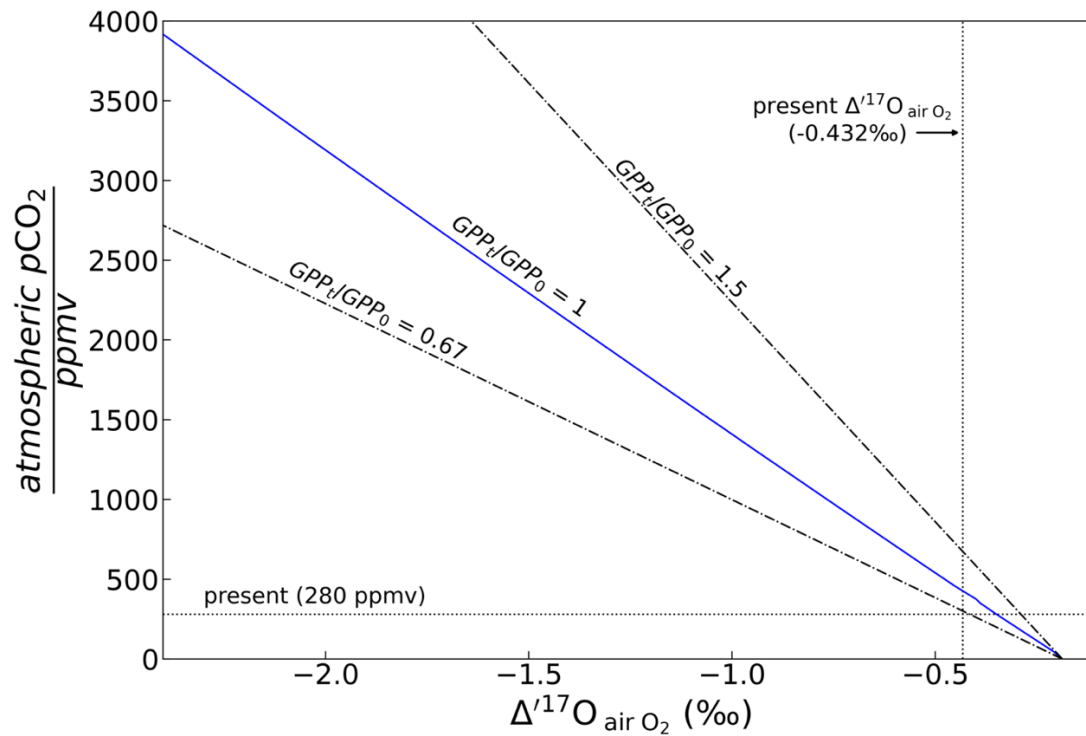Figure 7: Plot of pCO_2 (ppmv) vs. $\Delta'^{17}O$ of tropospheric O_2 (‰). The relation is taken from Bao et al. (2008) and recalculated with $\lambda = 0.528$. Shown are relations for GPP_t / GPP_0 of 0.67, 1.0 and 1.5 (see Luz et al., 1999).
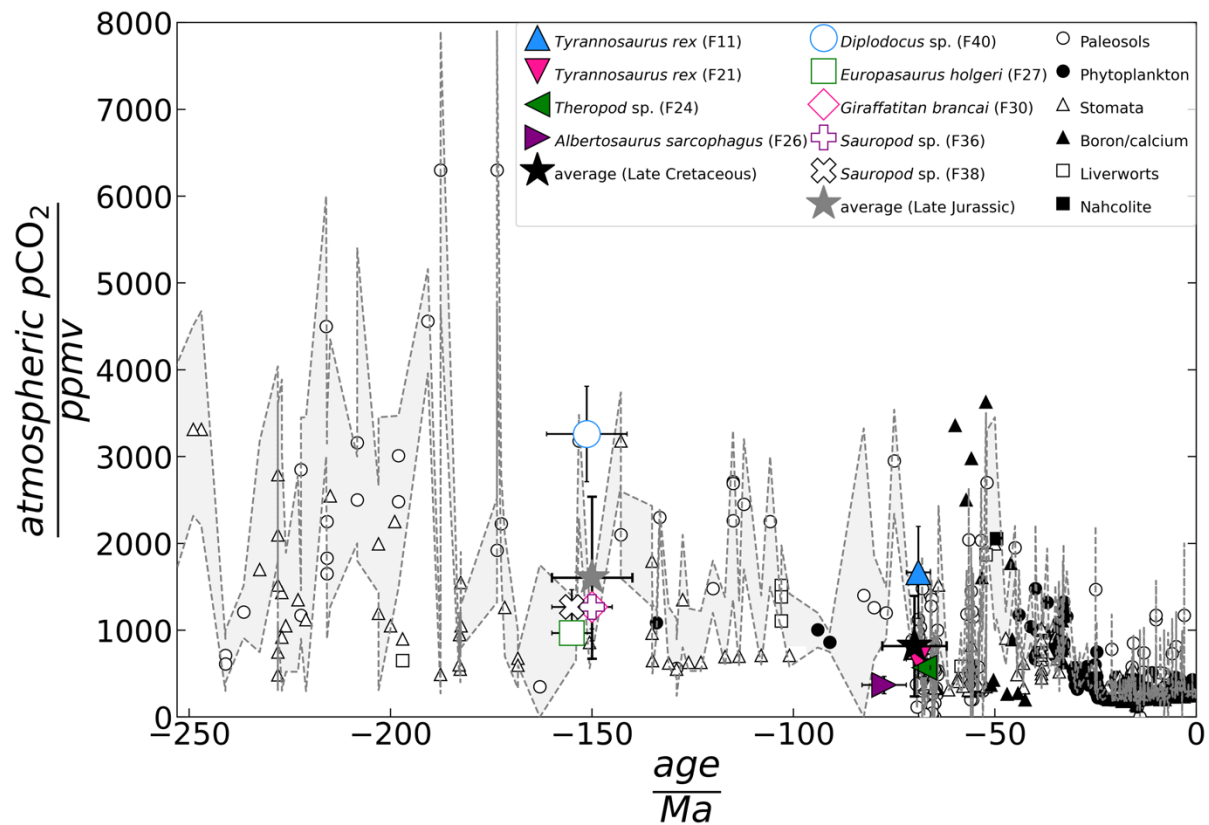
Figure 8: Plot of pCO_2 (ppmv) vs. time (Ma) from a compilation of available proxies (Royer, 2006; Beerling and Royer, 2011). Blue triangle pointing upwards: *Tyrannosaurus rex* (F11), pink triangle pointing downwards: *Tyrannosaurus rex* (F21), green triangle pointing left: *Theropod* sp. (F24), purple triangle pointing right: *Albertosaurus sarcophagus* (F26), black star: average during the Late Cretaceous. Blue circle: *Diplodocus* sp. (F40), green square: *Europasaurus holgeri* (F27), pink diamond: *Giraffatitan brancai.* (F30), purple cross: *Sauropod* sp. (F36), black X: *Sauropod* sp. (F38), grey star: average during the Late Jurassic. With $GPP_t / GPP_0 = 1$.

4.4   Comparison to other proxies

Figure 8 shows the past pCO_2 concentrations from different proxies in different geological periods (Beerling and Royer, 2011; Royer, 2006). Figure 8, During the Late Cretaceous, the higher pCO_2 value of 1665 ± 530 ppmv obtained from the *Tyrannosaurus rex* (F11; Figure 8) agrees within uncertainty with the pCO_2 reconstructed from paleosols (1480 ppmv, Beerling and Royer, 2002; Ekart et al., 1999; Nordt et al., 2003, 2002; Royer et al., 2001; Ghosh et al., 2005) and stomata (Beerling and Royer, 2002; Royer et al., 2001). The lowest pCO_2 value 368 ± 100 ppmv obtained from this study also falls into the range of the other proxies displayed in Figure 8. For the Late Jurassic, the higher pCO_2 value of 3260 ± 550 ppmv

obtained from the *Diplodocus* sp. also agrees with the pCO_2 reconstructed from paleosols (3180 ppmv, Ekart et al., 1999) and the lowest pCO_2 value of 967 ± 100 ppmv obtained from the *Europasaurus holgeri* fall into the range obtained from leaf stomata (McElwain, 1998; Retallack, 2001). The Late Cretaceous (817 ± 579 ppmv) and Late Jurassic (1605 ± 934 ppmv) average pCO_2 values from this study are indistinguishable from the averaged values derived from Royer (2006), Beerling and Royer (2011) (Late Cretaceous: 751 ± 543 ppmv; Late Jurassic (1670 ± 1333 ppmv) during the respective time intervals covered by our samples.

5   Conclusions

Triple oxygen ($\Delta'^{17}O$) and $\delta^{18}O$ data from modern bird bones agree with recent results from a large variety of modern terrestrial mammals (128; Feng et al., 2022b).

Applying the analytical approach of Feng et al. (2022a; 2022b) to fossil Mesozoic dinosaur tooth enamel results in the detection of anomalous $\Delta'^{17}O$ signatures that reflect the respective compositions of respired air O_2 ($\Delta'^{17}O_{air}$) which in turn depend on *GPP* and pCO_2.

Combining these findings with oxygen mass balance models based on Feng et al. (2022a; 2022b) gives significantly elevated atmospheric CO_2 concentrations when compared to today – a result that is confirmed by pCO_2 proxy data from previous studies (Royer, 2006; Beerling and Royer, 2011).

In summary, we reconstruct the Late Cretaceous atmospheric pCO_2 to 817 ± 579 ppmv from tooth enamel of four dinosaurs and the Late Jurassic pCO_2 to 1605 ± 934 ppmv from tooth enamel of five dinosaurs. Because pCO_2 data from other studies corroborate our results, it is concluded that the oxygen of the phosphate group of fossil tooth enamel sampled for this study carries pristine signatures of paleo air O_2 and hence paleo CO_2, even though indications for a diagenetic alteration of the bioapatite carbonate group is found for individual samples. Hence, $\Delta'^{17}O$ of tooth enamel proves its high potential for future paleoenvironmental studies, especially in settings where diagenetic alteration limits the successful application of carbonate-based techniques.

6   Acknowledgements

7   References

Arrhenius, S., 1896. On the Influence of Carbonic Acid in the Air Upon the Temperature of the Ground.

Bao, H., Lyons, J.R., Zhou, C., 2008. Triple oxygen isotope evidence for elevated CO_2 levels after a Neoproterozoic glaciation. Nature 453, 504–506.

Bates, K. T., Manning, P. L., Hodgetts, D., Sellers, W. I., 2009. Estimating mass properties of dinosaurs using laser imaging and 3D computer modelling. PLoS One 4, 1-26.

Beerling, D.J., Royer, D.L., 2011. Convergent Cenozoic CO_2 history. Nat. Geosci. 4, 418–420.

Beerling, D.J., Royer, D.L., 2002. Fossil plants as indicators of the phanerozoic global carbon cycle. Annu. Rev. Earth Planet. Sci. Lett. 30, 527–556.

Berner, R.A., 2006a. Inclusion of the weathering of volcanic rocks in the GEOCARBSULF model. Am. J. Sci. 306, 295–302.

Berner, R.A., 2006b. GEOCARBSULF: A combined model for Phanerozoic atmospheric O_2 and CO_2. Geochim. Cosmochim. Acta 70, 5653–5664.

Breecker, D.O., Sharp, Z.D., McFadden, L.D., 2010. Atmospheric CO_2 concentrations during ancient greenhouse climates were similar to those predicted for A.D. 2100. Proc. Natl. Acad. Sci. U. S. A. 107, 576–580.

Burnie, D., Wilson, D.E., 2005. Animal: The Definitive Visual Guide to the World's Wildlife. DK Adult, p129.

Chenery, C.A., Pashley, V., Lamb, A.L., Sloane, H..J., Evans, J.A., 2012. The oxygen isotope relationship between the phosphate and structural carbonate fractions of human bioapatite. Rapid Commun. Mass Spectrom. 26, 309-319.

Christiansen, P., Fariña, R. A., 2004. Mass prediction in theropod dinosaurs. Hist. Biol. 16, 85–92.

Cramp, S., and C. M. Perrins (editors). 1992. Handbook of the birds of Europe, the Middle East, and North Africa. Oxford University Press, Oxford, UK, Volumes 1, P37, 302, 328, 336, 352.

Dettman, D.L., Kohn, M.J., Quade, J., Ryerson, F.J., Ojha, T.P., Hamidullah, S., 2001. Seasonal stable isotope evidence for a strong Asian monsoon throughout the past 10.7 m.y. Geology 29, 31–34.

Dunning, Jr. J. B., 2007. Handbook of Avian Body Masses second edition. CRC Press, P83-84.

Eagle, R.A., Tütken, T., Martin, T.S., Tripati, A.K., Fricke, H.C., Connely, M., Cifelli, R.L., Eiler, J.M., 2011. Dinosaur body temperatures determined from isotopic (^{13}C-^{18}O) ordering in fossil biominerals. Science (80-.). 333, 443–445.

Ekart, D.D., Cerling, T.E., Montañez, I.P., Tabor, N.J., 1999. A 400 million year carbon isotope record of pedogenic carbonate: Implications for paleoatmospheric carbon dioxide. Am. J. Sci. 299, 805-827.

Erickson, G. M., Makovicky, P. J., Currie, P. J., Norell, M. A., Yerby, S. A., Brochu, C. A., 2004. Gigantism and comparative life-history parameters of tyrannosaurid dinosaurs. Nature 430, 772–775.

Feng, D.S., Tütken, T., Löffler, N., Tröster, G., Pack, A., 2022a. Isotopically anomalous metabolic oxygen in marine vertebrates as physiology and atmospheric proxy. Geochim. Cosmochim. Acta , in review.

Feng, D.S., Tütken, T., Löffler, N., Tröster, G., Zahnow, F., Surma, J., Pack, A., 2022b. Triple oxygen isotopes of modern terrestrial mammalian tooth enamel - new implications for paleoenvironmental and physiological research. Earth Planet. Sci. Lett. , in prepration.

Foster, G.L., Royer, D.L., Lunt, D.J., 2017. Future climate forcing potentially without precedent in the last 420 million years. Nat. Commun. 8, 1–8.

Fricke, H.C., Clyde, W.C., O'Neil, J.R., Gingerich, P.D., 1998. Evidence for rapid climate changes in North America during the latest Paleocene thermal maximum: oxygen isotope compositions of biogenic phosphate from the Bighorn Basin (Wyoming). Earth Planet. Sci. Lett. 160, 193–208.

Gabriela, D., Royer, D.L., Wolfe, A.P., Fox, A., Westgate, J.A., Beerling, D.J., 2011. Declining atmospheric CO_2 during the late Middle Eocene climate transition. Am. J. Sci. 311, 63–75.

Gehler, A., Tütken, T., Pack, A., 2012. Oxygen and Carbon Isotope Variations in a Modern Rodent Community - Implications for Palaeoenvironmental Reconstructions. PLoS One 7, 16–27.

Ghosh, P., Bhattacharya, S.K., and Ghosh, P., 2005, Atmospheric CO_2 during the Late Paleozoic and Mesozoic: Estimates from Indian soils, in Ehleringer, J.R., Cerling, T.E., and Dearing, M.D., eds., A History of Atmospheric CO_2 and Its Effects on Plants, Animals, and Ecosystems: New York, Springer, p. 8-34.

Hagan, E. (2004). Anodorhynchus hyacinthinus. Animal Diversity Web.

Hancock, J. A., Kushlan, J. A., Kahl, M. P., 1992. Storks, ibises, and spoonbills of the world.

Academic Press, New York. 474, p97, 133.

Hicks, J.W., Farmer, C.G., 1999. Gas exchange potential in reptilian lungs: Implications for the dinosaur-avian connection. Respir. Physiol. 117, 73–83.

Hulston J R and Thode H G, 1965. Variations in the S^{33} S^{34} and S^{36} Contents of Meteorites and Their Relation to Chemical and Nuclear Effects. J. Geophys. Res. 70, 3475–3484.

Hutchinson, J. R., Bates, K. T., Molnar, J., Allen, V., Makovicky, P. J., 2011. A computational analysis of limb and body dimensions in tyrannosaurus rex with implications for locomotion, ontogeny, and growth. PLoS One 6, 1-20.

Ji, Q., Ji, S., Museum, C.G., Geology, C., By, T., Downs, W., 1996. On the Discovery of the earliest fossil bird in China (Sinosauropteryx gen. nov.) and the origin of birds. Chinese Geol. 233, 30–33.

Kohn, M.J., Cerling, T.E., 2002. Stable isotope compositions of biological apatite. Phosphates Geochemical, Geobiol. Mater. Importance 48, 455–488.

Kohn, M.J., Schoeninger, M.J., Barker, W.W., 1999. Altered states: Effects of diagenesis on fossil tooth chemistry. Geochim. Cosmochim. Acta 63, 2737–2747.

Kolodny, Y., Luz, B., Navon, O., 1983. Oxygen isotope variations in phosphate of biogenic apatites, I. Fish bone apatite-rechecking the rules of the game. Earth Planet. Sci. Lett. 64, 398–404.

König, Claus & Weick, Friedhelm. 2008. "Owls: A Guide to the Owls of the World (Second Edition)". Yale University Press, P24.

Kürschner, W.M., Kvaček, Z., Dilcher, D.L., 2008. The impact of Miocene atmospheric carbon dioxide fluctuations on climate and the evolution of terrestrial ecosystems. Proc. Natl. Acad. Sci. U. S. A. 105, 449–453.

Lee-Thorp, J.A., Sponheimer, M., Luyt, J., 2007. Tracking changing environments using stable carbon isotopes in fossil tooth enamel: an example from the South African hominin sites. J. Hum. Evol. 53, 595–601.

Li, Z., Pasteris, J.D., 2014. Tracing the pathway of compositional changes in bone mineral with age: Preliminary study of bioapatite aging in hypermineralized dolphin's bulla. Biochim. Biophys. Acta - Gen. Subj. 1840, 2331–2339.

Lowenstein, T.K., Demicco, R. V., 2006. Elevated eocene atmospheric CO_2 and its subsequent decline. Science (80-.). 313, 1928.

Lüthi, D., Le Floch, M., Bereiter, B., Blunier, T., Barnola, J.M., Siegenthaler, U., Raynaud, D., Jouzel, J., Fischer, H., Kawamura, K., Stocker, T.F., 2008. High-resolution carbon dioxide concentration record 650,000-800,000 years before present. Nature 453, 379–

382.

Luz, B., Kolodny, Y., Horowitz, M., 1984. Fractionation of oxygen isotopes between mammalian bone-phosphate and environmental drinking water. Geochim. Cosmochim. Acta 48, 1689–1693.

Luz, B., Barkan, E., Bender, M.L., Thiemens, M.H., Boering, K.A., 1999. Triple-isotope composition of atmospheric oxygen as a tracer of biosphere productivity. Nature 400, 547–550.

Löffler, N., 2020. Application of the refined clumped isotope temperature calibration on Tyrannosaurus rex teeth from the adult specimen "Trix" (RGM 792.000). Ph.D Thesis chapter 3, p67.

Mazzetta, G. V., Christiansen, P., Fariña, R. A., 2004. Giants and bizarres: Body size of some Southern South American Cretaceous dinosaurs. Hist. Biol. 16, 71–83.

McElwain, J.C., 1998. Do fossil plants signal palaeoatmospheric CO_2 concentration in the geological past? Philos. Trans. R. Soc. B Biol. Sci. 353, 83–96.

Mcnab, B.K., 1988. Food habits and the basal rate of metabolism in birds. Oecologia 77, 343-349.

Nordt, L., Atchley, S., Dworkin, S., 2003. Terrestrial evidence for two greenhouse events in the latest Cretaceous. GSA Today 13, 4–9.

Nordt, L., Atchley, S., Dworkin, S.I., 2002. Paleosol barometer indicates extreme fluctuations in atmospheric CO_2 across the Cretaceous-Tertiary boundary. Geology 30, 703–706.

Pack, A., 2021. Isotopic Traces of Atmospheric O_2 in Rocks, Minerals, and Melts. Rev. Mineral. Geochemistry 86, 217–240.

Pack, A., Gehler, A., Süssenberger, A., 2013. Exploring the usability of isotopically anomalous oxygen in bones and teeth as paleo-CO_2-barometer. Geochim. Cosmochim. Acta 102, 306–317.

Pack, A., Tanaka, R., Hering, M., Sengupta, S., Peters, S., Nakamura, E., 2016. The oxygen isotope composition of San Carlos olivine on the VSMOW2-SLAP2 scale. Rapid Commun. Mass Spectrom. 1495–1504.

Pagani, M., Zachos, J.C., Freeman, K.H., Tipple, B., Bohaty, S., 2005. Atmospheric science: Marked decline in atmospheric carbon dioxide concentrations during the Paleogene. Science (80-.). 309, 600–603.

Paul, G. S., 2013. The Princeton field guide to dinosaurs 2nd edition. Princeton University Press, p112, 226, 227.

Pearson, P.N., Foster, G.L., Wade, B.S., 2009. Atmospheric carbon dioxide through the

Eocene-Oligocene climate transition. Nature 461, 1110–1113.

Petit, J.R., Jouzel, J., Raynaud, D., Barnola, J.M., Basile, I., Bender, M., Chappellaz, J., Davis, M., Delaygue, G., Delmotte, M., Kotlyakov, V.M., Legrand, M., Lipenkov, V.Y., Loriu, C., Pepin, L., Ritz, C., Saltzman, E., Stievenard, M., 1999. Climate and atmospheric history of the past 420,000 years from the Vostok ice core, Antarctica. Nature 399, 348–358.

Retallack, G.J., 2001. A 300-million-year record of atmospheric carbon dioxide from fossil plant cuticles. Nature 411, 287–290.

Roth-Nebelsick, A., 2005. Reconstructing atmospheric carbon dioxide with stomata: Possibilities and limitations of a botanical pCO$_2$-sensor. Trees - Struct. Funct. 19, 251–265.

Royer, D.L., 2006. CO$_2$-forced climate thresholds during the Phanerozoic. Geochim. Cosmochim. Acta 70, 5665–5675.

Royer, D.L., Berner, R.A., Beerling, D.J., 2001. Phanerozoic atmospheric CO$_2$ change: Evaluating geochemical and paleobiological approaches, Earth-Science Reviews.

Sharp, Z.D., 1990. A laser-based microanalytical method for the in situ determination of oxygen isotope ratios of silicates and oxides. Geochim. Cosmochim. Acta 54, 1353–1357.

Sharp, Z.D., Gibbons, J.A., Maltsev, O., Atudorei, V., Pack, A., Sengupta, S., Shock, E.L., Knauth, L.P., 2016. A calibration of the triple oxygen isotope fractionation in the SiO$_2$-H$_2$O system and applications to natural samples. Geochim. Cosmochim. Acta 186, 105–119.

Shemesh, A., Kolodny, Y., Luz, B., 1983. Oxygen isotope variations in phosphate of biogenic apatites, II. Phosphorite rocks. Earth Planet. Sci. Lett. 64, 405–416.

Sisma-Ventura, G., Tütken, T., Peters, S.T.M., Bialik, O.M., Zohar, I., Pack, A., 2019. Past aquatic environments in the Levant inferred from stable isotope compositions of carbonate and phosphate in fish teeth. PLoS One 14, 1–18.

Thomas, D.B., McGoverin, C.M., Fordyce, R.E., Frew, R.D., Gordon, K.C., 2011. Raman spectroscopy of fossil bioapatite - A proxy for diagenetic alteration of the oxygen isotope composition. Palaeogeogr. Palaeoclimatol. Palaeoecol. 310, 62–70.

Tütken, T., Vennemann, T.W., Janz, H., Heizmann, E.P.J., 2006. Palaeoenvironment and palaeoclimate of the Middle Miocene lake in the Steinheim basin, SW Germany: A reconstruction from C, O, and Sr isotopes of fossil remains. Palaeogeogr. Palaeoclimatol. Palaeoecol. 241, 457–491.

Wostbrock, J.A.G., Cano, E., Sharp, Z.D., 2020. An internally consistent triple oxygen isotope calibration of standards for silicates, carbonates and air relative to VSMOW2 and SLAP2. Chem. Geol. 533, 119432.

Young, E.D., Galy, A., Nagahara, H., 2002. Kinetic and equilibrium mass-dependent isotope fractionation laws in nature and their geochemical and cosmochemical significance. Geochim. Cosmochim. Acta 66, 1095–1104.

Chapter 5 Techniques for high-precision analysis of triple oxygen isotope ratios of bioapatite

Abstract

Since the utilization of bioapatite as an archive for (palaeo)climatic, (palaeo)ecological and (palaeo)environmental reconstructions, a variety of stable isotope-based proxies have been developed and applied. Since 2011, high precision triple oxygen isotope analysis of bioapatite has repeatedly shown its potential for deriving new insights into important research questions of Earth Sciences (Gehler et al., 2011, 2016; Pack et al., 2013). One particular challenge during triple oxygen isotope analyses of bioapatite is to ensure that only one single oxygen reservoir (e.g. CO_3^{2-} *vs.* PO_4^{3-}) contributes to the analyte O_2. Here we present the analytical techniques that we tested for high precision triple oxygen isotope analysis of oxygen from the bioapatite phosphate group. Our approach is based on mass spectrometric analysis of bioapatite or Ag_3PO_4 powder by infrared-laser fluorination. We obtained the triple oxygen isotope anomaly of $\Delta'^{17}O$ of bioapatite with a high precision of $\pm$ 11 ppm (1σ SD, n=162). Our new technique allows accurate and precise determination of investigating triple oxygen isotope analysis of bioapatite.

1   Introduction

Because of the strong P–O bonds in apatite and the associated high resistance to diagenesis alteration (Shemesh et al., 1983; Kohn et al., 1999; Kohn and Cerling, 2002; Vennemann et al., 2002; Sharp, 2017), oxygen isotope ratios of biogenic phosphate is considered a more powerful paleoenvironmental proxy than carbonates. Tudge (1960) was the pioneer to devise a reliable method for oxygen isotope analysis of biogenic phosphate, in which large amounts (100 mg) of biogenic phosphate were dissolved in nitric acid, transferred to ammonium phosphomolabdate and magnesium ammonium phosphate, and ultimately reprecipitated as $BiPO_4$. The $BiPO_4$ was then fluorinated with BrF_3 to yield O_2 gas. This method was used in all early studies of oxygen isotope variations of biogenic phosphate despite the tedious precipitation procedures and hygroscopicity. Crowson et al. (1991) resurrected and refined the Ag_3PO_4 precipitation method of Firsching (1961). Since then, Ag_3PO_4 has been widely used for the $\delta^{18}O$ oxygen isotope measurements instead of $BiPO_4$ (Ayliffe et al., 1992; Lécuyer et al., 1993; Bryant and Froelich, 1995; Fricke and O'Neil, 1996; Lécuyer et al.,

1996; Blake et al., 1997; Fricke et al., 1998; Vennemann and Hegner, 1998; Fricke and Rogers, 2000; Vennemann et al., 2001; Vennemann et al., 2002; Lécuyer, 2004; Tütken et al., 2006; Tütken and Vennemann, 2009). The most widespread analytical technique for $\delta^{18}O$ measurements of Ag_3PO_4 involves high-temperature reduction with graphite in a glassy carbon reactor, using TCEA peripherals. With this technique the oxygen in Ag_3PO_4 is converted quantitatively to CO and analyzed by continuous flow mass spectrometry (IRMS) (Vennemann et al., 2001; Vennemann et al., 2002; Lécuyer, 2004; Tütken et al., 2006; Tütken and Vennemann, 2009).

Levin et al. (2006), Passey et al. (2014) and Passey and Levin (2021) reported a sequential acid digestion, reduction and fluorination approach for triple oxygen isotope analysis of biogenic carbonates. Due to the digenetic alteration of carbonates, this method is strongly limited to modern materials.

Gehler et al. (2011, 2016), and Pack et al. (2013) developed a method for triple oxygen ($\Delta'^{17}O$) isotope measurements of biogenic phosphate. However, they reported large uncertainties for $\Delta'^{17}O$ ($\pm$ 50 ppm) measured in continuous flow IRMS. Here we represent experimental analytical techniques that were tested for high precision $\Delta'^{17}O$ analysis of bioapatite by means of laser fluorination dual inlet IRMS.

2   The laser fluorination extraction line (LF)

The gas extraction line employed for laser fluorination and O_2 purification is illustrated in Figure 1 (modified after Pack et al., 2016). The analytical procedure is fully automated using *Labview*™.

For the measurements, aliquots of approximately 2 mg were loaded into a vacuum chamber and evacuated overnight down to ~ 3×10^{-6} mbar.
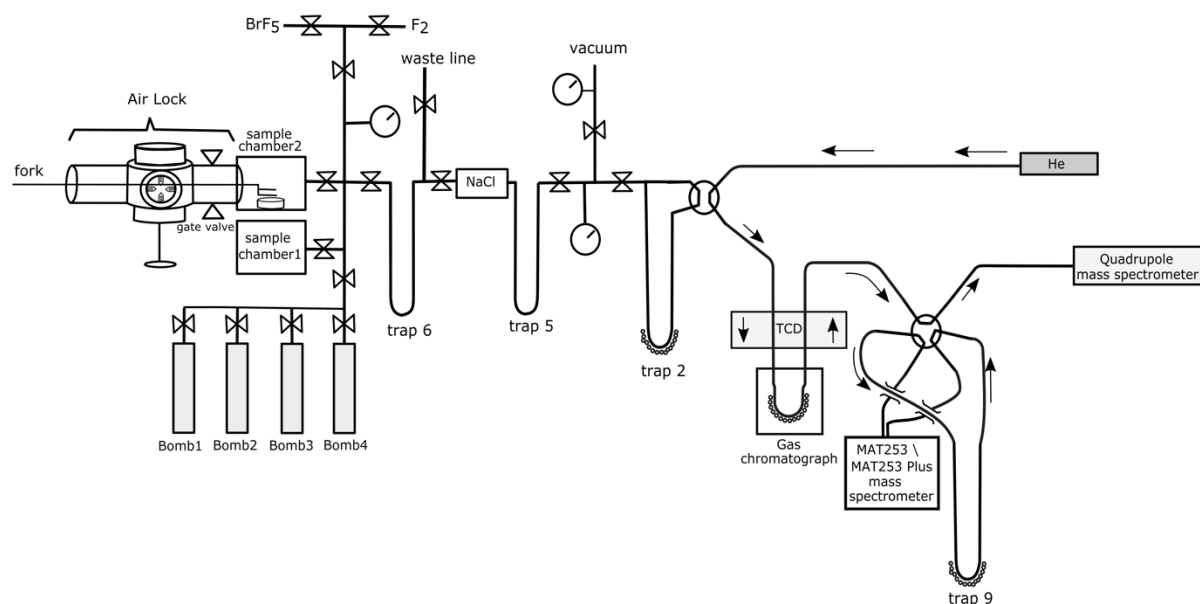
Figure 1: Schematic of the laser fluorination extraction line (modified after Pack et al., 2016).

Sample materials were then laser fluorinated (Sharp, 1990) in the presence of ~100 mbar of BrF_5 (or F_2), used as fluorinating agent. Following fluorination, condensable gases (e.g. BrF_5 and HF) were cryo-trapped at liquid nitrogen temperature (T= –192 °C in trap 6). Traces of F_2 were reacted with heated NaCl (T= 180 °C) to produce Cl_2, which was cryo-trapped in trap 5. The purified O_2 was then transferred to trap 2, which was filled with 5 Å molecular sieve, for ~ 10 mins. From trap 2, the sample O_2 was transported via a He carrier gas stream (10 mL min^{-1}) through a gas chromatograph (Agilent Technologies, Santa Clara, CA, USA) to separate O_2 from N_2, NF_3 and other incondensable gases. The gas chromatograph is equipped with a 4 m column packed with 5 Å molecular sieve (1/8" OD, 80-100 mesh). Separation was conducted at 50 °C and a quadrupole mass spectrometer was connected to monitor the gas separation. A thermal conductivity detector (TCD) was also connected to the GC to monitor the extracted O_2 gas volumes.

After separation of contaminating gas, the eluted pure O_2 gas was trapped in trap 9 (T= –192 °C) filled with 5 Å molecular sieve. The residual He carrier gas was evacuated through the pumping system of the mass spectrometer. Then, the sample O_2 and molecular sieve were heated to 50 °C in a water bath. Afterwards, the sample O_2 was expanded into the sample bellows of a Thermo MAT 253 or 253 Plus (Thermo Fisher Scientific, Bremen, Germany) gas source isotope ratio mass spectrometer (IRMS).

The isotope ratios in the extracted sample O_2 gas were measured with a Thermo MAT 253 or 253 Plus IRMS in dual inlet model with simultaneous detection of m/z 32, 33 and 34. For each sample, 40 cycles were measured with a total measurement time of ~ 90 mins. The intensity on mass 32 was adjusted to ~ 5V. The reference O_2 gas was measured before, between, and after each session's sample O_2 measurements. The reference gas was calibrated using O_2 released from San Carlos olivine ($\delta^{18}O = 5.23‰$, $\Delta'^{17}O_{0.528} = -52$ ppm; see Pack, 2021) and has an isotopic composition of $\delta^{18}O = 15.7‰$ and $\Delta'^{17}O_{0.528} = -450$ ppm vs. VSMOW2. We routinely run the reference gas to monitor its isotopic stability. Besides, we scan the sample O_2 gas to check the gas purification quality and to verify the absence of potential contaminants.

The gas extraction procedure has been continuously improved and simplified for better efficiency and accuracy since 2017 with technical upgrades (e.g., two sample chamber setup and automatic measurement procedure).

3 Ag_3PO_4 laser fluorination with air-lock system

A first attempt to measure the triple oxygen isotope composition of the phosphate fraction of tooth enamel was carried out by using the air-lock system after precipitation of samples as silver phosphate (Ag_3PO_4). This precipitation was performed according to Dettman et al. (2001), modified by Tütken et al. (2006). Precipitation details are explained in Chapter 2.4.2.

Briefly, Ag_3PO_4 aliquots of 2.5 mg precipitated from bioapatite were mounted in small, 2-pits sample ships (Figure 2 A) together with San Carlos Olivine, introduced into the sample chamber 2 through the air lock system (i.e. from vacuum to vacuum), equipped with a gate valve and pumped down to ~5 x 10^{-6} mbar for at least 12 hours. The air lock system was installed to the extraction line with the specific goal to allow fluorination of potentially highly reactive material, such as Ag_3PO_4, and minimize potential cross contamination as in a conventional multi-pit sample holder (Figure 2 B). Samples were laser fluorinated in the presence of ~100 mbar of BrF_5 used as fluorinating agent. The Ag_3PO_4 was analyzed first, followed by San Carlos Olivine from the same sample ship.
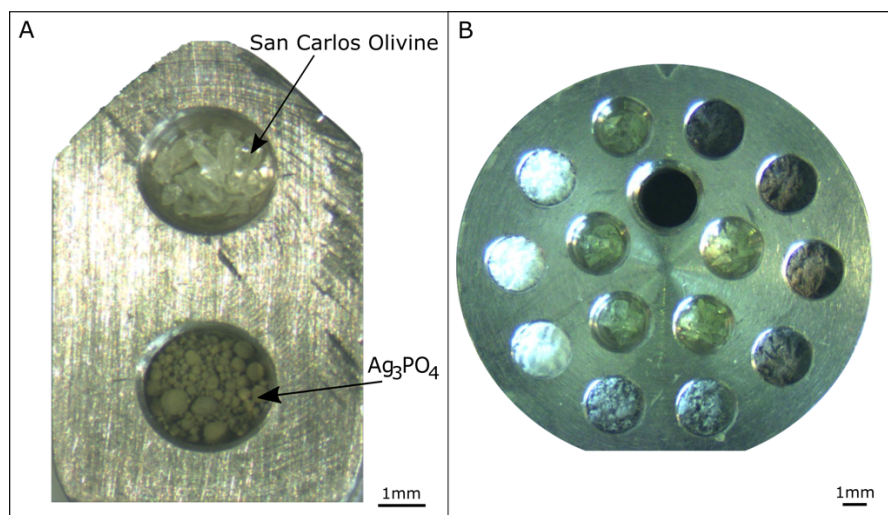
Figure 2 A: the sample ships with San Carlos Olivine and silver phosphate (Ag_3PO_4). B: 14 pits sample holder.

$\Delta'^{17}O$ of Ag_3PO_4 precipitated from 4 bioapatite samples measured with BrF_5 laser fluorination air-lock system (LF air-lock) are listed in Table 1 and referred to as $\delta^{18}O_{Ag3PO4}$ and $\Delta'^{17}O_{Ag3PO4}$. The same Ag_3PO_4 samples were analyzed with TC/EA. The results are also listed in Table 1 and referred to as $\delta^{18}O_{PO4}$. Identical materials of those 4 bioapatite were heated in 10% H_2 mixed with 90% N_2 gas and then measured within a 14 pits sample holder by laser fluorination (LF). These results are also showed on Table 1 and referred to as $\Delta'^{17}O_{AP}$ (details in Chapter 2).

Table 1 Triple oxygen isotope data from Ag_3PO_4.

Sample	Name	$\delta^{18}O_{Ag3PO4}$ (‰)	$\Delta'^{17}O_{Ag3PO4}$ (ppm)	Yield (%)	$\delta^{18}O_{PO4}$ (‰)	$\Delta'^{17}O_{AP}$ (ppm)	Yield (%)
		LF air-lock	LF air-lock	LF air-lock	TC/EA	LF	LF
M150	Sand tiger shark	17.64	-108	41	21.05	-124	92
		16.47	-49	56			
M151	Sandbar shark	18.37	-113	56			
		18.48	-108	50			
average		17.77	-90	54	20.90	-109	100
M154	Greenland shark	20.10	-103	27	24.34	-134	96
	AG-Lox	14.56	-84	35	20.50	-107	92

The results show that the $\delta^{18}O$ of Ag_3PO_4 from LF is 4.2‰ lower on average comparing to the data obtained from TC/EA. The $\Delta'^{17}O$ of Ag_3PO_4 from LF is 20 ppm higher on average comparing to the data obtained from bioapatite as illustrated by Figure 3.

Further downsides of LF air-lock technique on Ag_3PO_4, were that the reaction caused intense fogging of the laser window and that the yields were all bellow 60%.
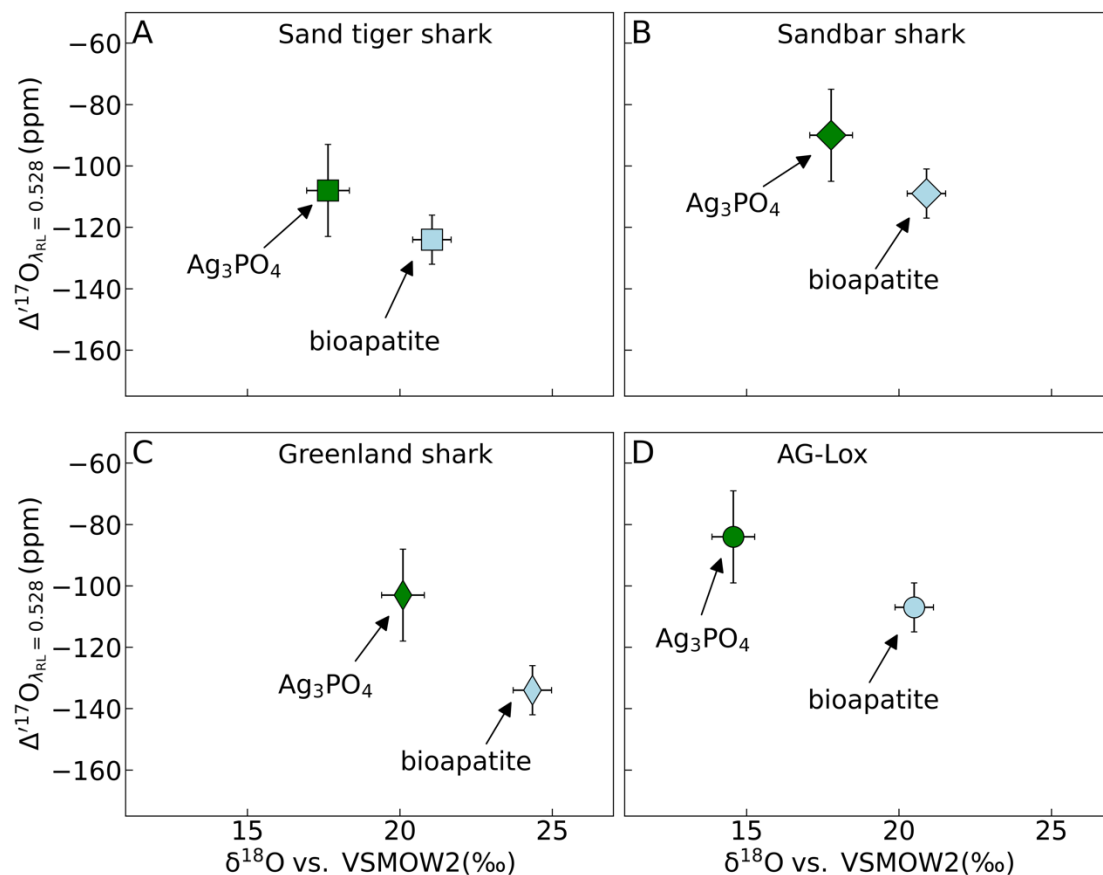

Figure 3: The $\delta^{18}O$ and $\Delta'^{17}O$ of Ag_3PO_4 from air-lock system vs. $\delta^{18}O$ and $\Delta'^{17}O$ of bioapatite (heated in H_2+N_2) from 14 pits sample holder. A: sand tiger shark; B: sandbar shark; C: Greenland shark; D: AG-Lox.

4 Ag_3PO_4 fluorination with bombs

Because of the low $\delta^{18}O$ of Ag_3PO_4 and low yield from air-lock system, we tested the usability of nickel bombs to measure the triple oxygen isotope of Ag_3PO_4 (see Lécuyer et al., 1993). The nickel bombs were attached to the extraction line, evacuated, baked out at high temperature and passivated (Figure 1).

The suitability of the traditional fluorination method using Ni bombs for Ag_3PO_4 was tested as follows. About 7 mg of Ag_3PO_4 were inserted into the bombs and fluorinated with 200 mbar of BrF_5. The bombs were externally heated at 750º C for 48 hours. The tests with Ni-bomb revealed to be unsuccessful as the produced gas mixture showed negligible amount of O_2 and very high amount of CF_3 with mass 69 (Figure 4).
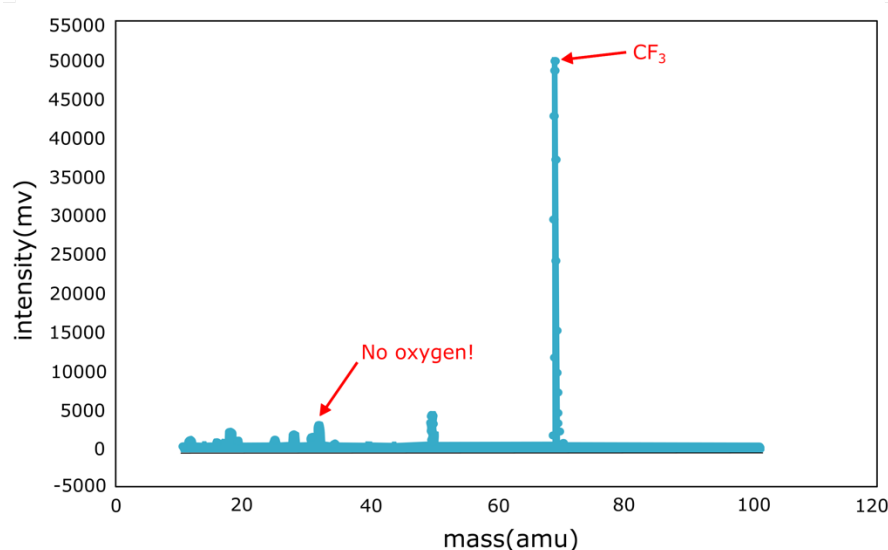
Figure 4: The scan file of the gas in the mass spectrometer from the bombs.

5 Laser fluorination of bioapatite

5.1 Preheating techniques of bioapatite

In order to remove organic material from bioapatite (which could be the source of contamination), different heating procedure were tested. We used *Dama dama* (male) bones and *Loxodonta africana* teeth enamel (AG-Lox, Gehler et al., 2012) as test materials.

The sample powders were treated with 2 ml H_2O_2 (30%) for more than 12 hours to remove the organic matter. Afterwards pre-treated samples were heated to 1000 °C in a horizontal furnace to remove residual organic material and carbonate and hydroxy groups in bioapatite.

Instead of H_2O_2 for the pre-treatment, we also treated with 2% NaClO for 45 minutes and 0.1% CH_3COOH for 15 minutes including centrifugal separation, then rinsed the samples with distilled water 5 times for each step and dried overnight at 70 °C.

Afterwards, pre-treated samples were heated to 1000 °C in a horizontal furnace to remove residual organic material and carbonate and hydroxy groups in bioapatite. Several gases were tested in the furnace during this procedure, including air, Ar, and 10% H_2 mixed with 90% N_2 ($H_2 + N_2$) (Figure 5). The gas flow rate was adjusted to 50 ml min^{-1} a gas flow controller. The heating times varied from 1 minute up to 40 minutes. After the heating was done, the samples were cooled down in the same atmosphere, weighed for the sample mass lose after heating and saved in the desiccator.
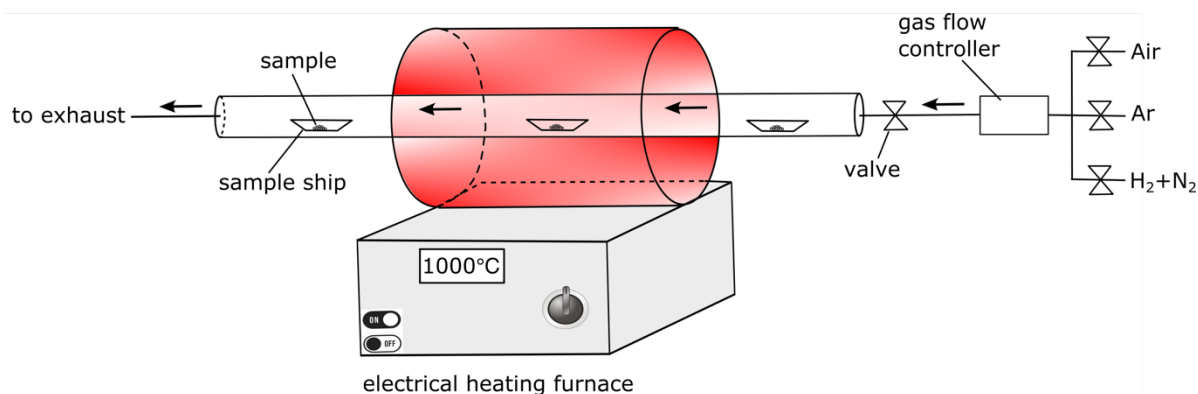
Figure 5: The electrical heating furnace. We could change the flushing gas from air, Ar to H_2+N_2.

Our tests show that after 1 min, the organic materials decomposed resulting in a mass loss of about 45%wt. for *Dama dama* and 10%wt. for AG-Lox (Figure 6). We tested with different heating time up to 3 hours and observed consistent mass loss.
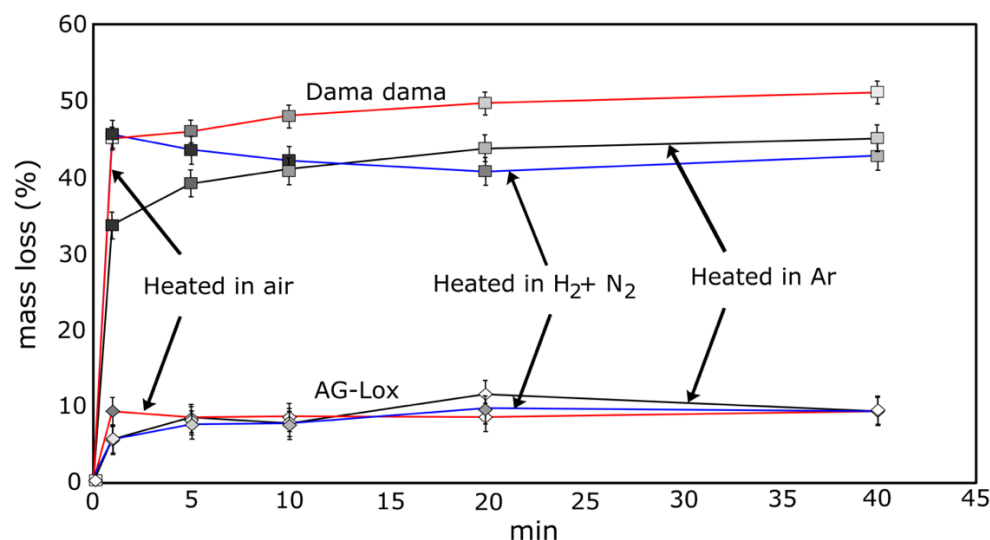

Figure 6: The sample mass loss (%) of *Dama dama* and AG-Lox after heating to 1000 degree in furnace with different gas flushing.

5.2 Organic matter combustion of bioapatite

The presence of organic and inorganic carbon content in bioapatite was tested using a gradual heating method on a LECO RC612 multi-phase carbon analyzer (Leco, St Joseph, MI, USA), calibrated against LECO carbon standards (1.00%C, 4.98%C and 12.00%C).

After weighing in 20 mg of bioapatite, the sample was introduced into the combustion chamber of the LECO carbon analyzer. With a preprogrammed temperature profile of 150 °C to 900 °C, the samples were fed with an O_2+N_2 mixture (1:1 at 3.5 bar) reacted with a gas flow of 2.5 ml min^{-1}. O_2 is used for oxidation and N_2 for transporting CO_2 to the UV detector.

The LECO carbon standards were measured between measuring each sample twice to calibrate the values.

For the raw AG-Lox (i.e. without chemical pretreatment and pre-heating in the horizontal furnace), two large peaks were detected by the LECO carbon analyzer (Figure 8, blue curve). The different peaks result from the different temperature stability of the carbon compounds. The organics were converted at lower temperatures than structure carbonates (Figure 8). After heating for more than 30 mins, no CO_2 gas was liberated indicating a complete removal of organic and inorganic carbon. In total there we estimate that AG-Lox contains approximately 0.37% of carbon.

Tests conducted on bioapatite pretreated with NaClO and CH_3COOH but unheated in the horizontal furnace show that although most of the carbon was successfully chemically removed, residual carbon were still detectable by the LECO apparatus (Figure 8, black curve).

For AG-Lox pre-heated in the horizontal furnace (in $H_2 + N_2$ atmosphere) and chemically pretreated, no CO_2 was produced (Figure 8, green curve). This demonstrated that the heating in $H_2 + N_2$ atmosphere successfully removed all the organic and inorganic carbon.

Consequently, we applied NaClO and CH_3COOH pretreatment prior to heating the bioapatite in $H_2 + N_2$ for 30 mins at 1000 °C to fully remove carbon from bioapatite samples. We could not observe any impact of this pretreatment on the phosphate group in the bioapatite.
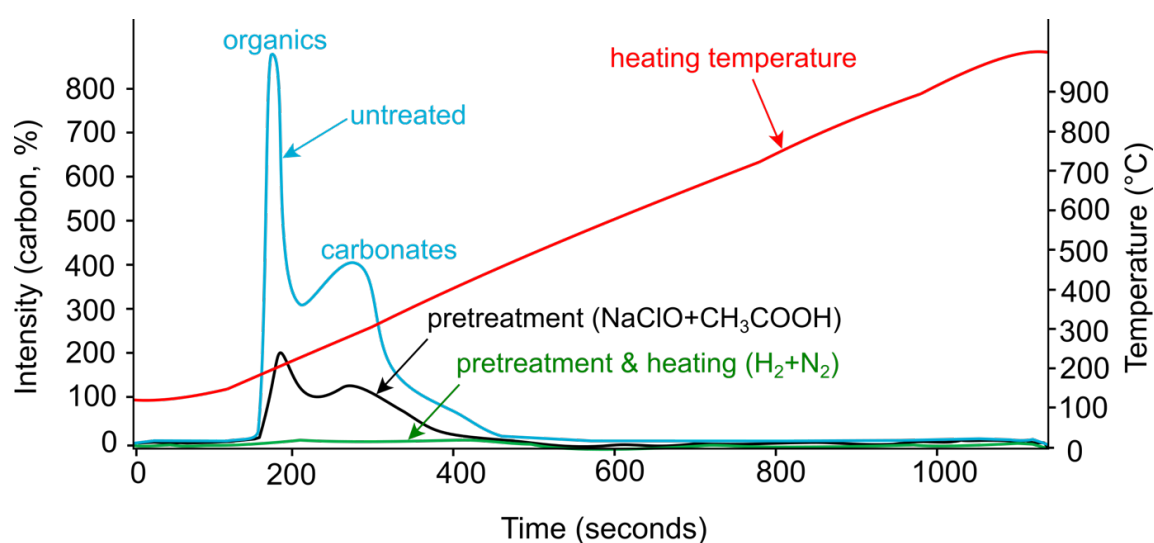

Figure 7: Overview on the CO_2 volumes of AG-Lox tooth enamel combusted in the LECO carbon analyzer. Blue curve: untreated; black curve: treated with NaClO and CH_3COOH; green curve: treated with NaClO and

CH3COOH, and then heated to 1000 °C in the furnace flushed with $H_2 + N_2$. This figure is also been presented in Chapter 2.

5.3 Results

5.3.1 Pre-heated in air & Ar

We measured the samples heated in air and Ar with BrF_5 laser fluorination (LF) using the air-lock system. The results are showed in Figure 7 and listed in Table 2. For AG-Lox heated in air, the oxygen isotopic composition plot closer to the composition of air, implying an isotopic exchange during heating. The scan files from the samples heated in Ar showed high amount of CF_3 (similar to the samples measured in bombs; section 4) (Figure 4). Heating bioapatite in air or Ar therefore results in no analytical improvement.

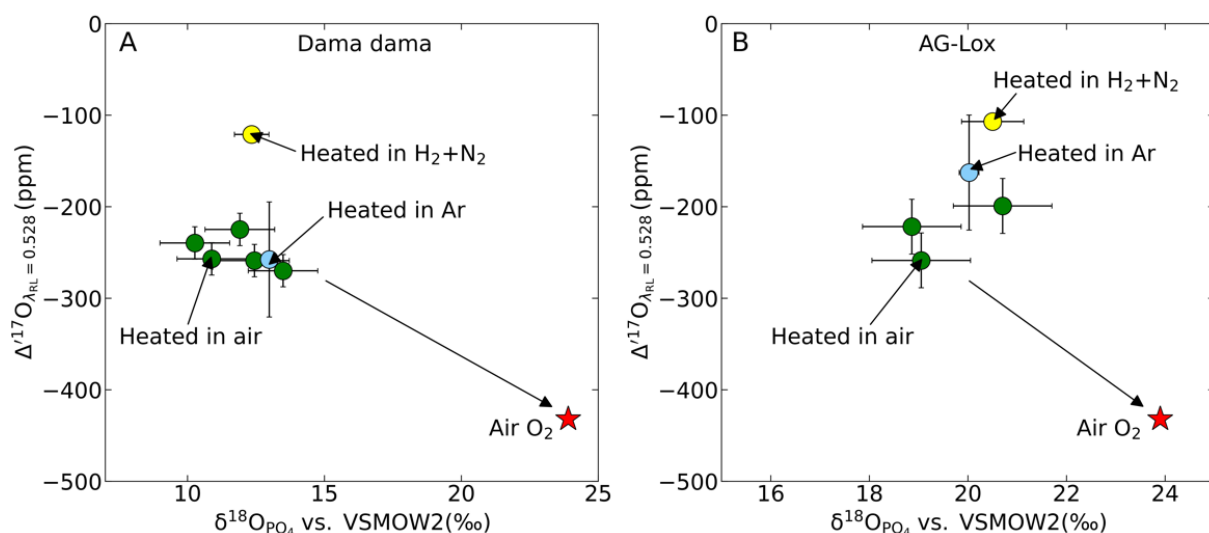
Figure 8: The $\delta^{18}O$ and $\Delta'^{17}O$ of bioapatite heated to 1000 °C. A: *Dama dama*. B: AG-Lox. Green points: heated in air, blue points: heated in Ar. The red star represents the air O_2 and the yellow points represents data from samples heated in $H_2 + N_2$.

Table 2 Triple oxygen isotope data of *Dama dama* and AG-Lox.

Sample	Heating gas	$\delta^{18}O_{PO4}$ (‰)	$\Delta'^{17}O_{PO4}$ (ppm)
		LF	LF
Dama dama	air	12.45	-259
	air	13.49	-270
	air	10.27	-240
	air	11.91	-225
	air	10.89	-257
	Ar	12.99	-258
	$H_2 + N_2$	12.34	-121
AG-Lox	air	18.86	-222
	air	19.05	-259
	air	20.70	-199
	Ar	20.02	-163
	$H_2 + N_2$	20.50	-107

5.3.2   Pre-heated in $H_2 + N_2$

After the chemical and thermal pretreatment, approximately 2.5 mg preheated bioapatite was loaded into a polished Ni metal sample holder with 14 pits, along with the AG-Lox and San Carlos Olivine reference materials. After installing the sample holder into the sample chamber and evacuating it for at least 12 hours, the tooth enamel was pre-melted with up to 5.5% laser power (SYNRAD 50 W CO_2 laser). The samples were laser fluorinated after being evacuated overnight at 70 °C.

We run AG-Lox as internal bioapatite standard. The scan files of the analyte gases released from the AG-Lox heated in H_2+N_2 in the mass spectrometer showed high amounts of O_2 gas and verified the absence of contaminants (e.g. CF_3) (Figure 9).

The AG-Lox $\delta^{18}O_{AP}$ and $\Delta'^{17}O_{AP}$ of from laser fluorination are shown in Figure 10. The overall mean $\delta^{18}O_{AP}$ and $\Delta'^{17}O$ (Figure 10, black asterisk) derived from laser fluorination analyses are $\delta^{18}O_{AP} = 19.53 \pm 0.86$‰ and $\Delta'^{17}O_{AP} = -109 \pm 11$ ppm (n = 162). This is statistically indistinguishable when compared to the respective TC/EA derived $\delta^{18}O_{PO4}$ value of 20.53 ± 0.79‰ (Chapter 2, section 3). These data are listed in Appendix table S3.
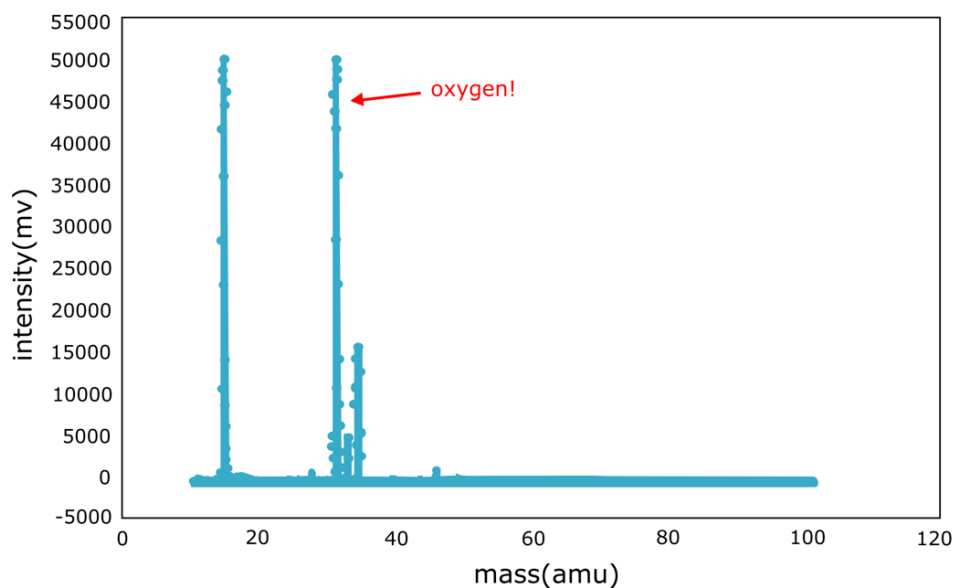
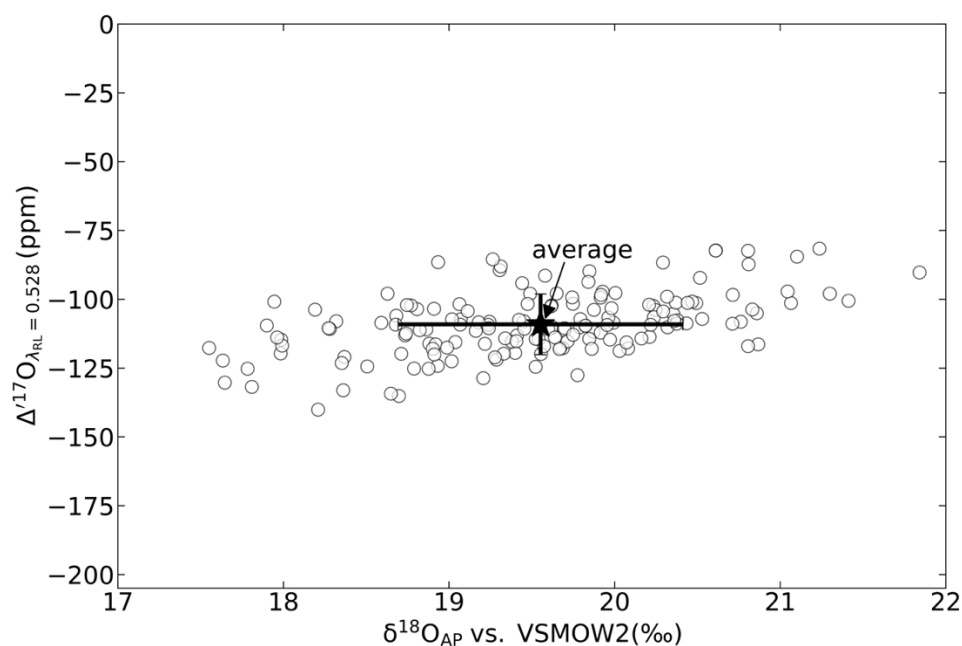Figure 9: The scan file of the gas in the mass spectrometer from the AG-Lox (heated in H_2+N_2).

Figure 10: The $\delta^{18}O_{AP}$ and $\Delta'^{17}O_{AP}$ data of the AG-Lox from laser fluorination. The black asterisk is the overall (n=162) average. The error bars indicate the 1σ standard deviation.

6   Conclusion

Different chemical and thermal pretreatment methods for bioapatite as well as varying introductions of the powdered samples into the laser fluorination line (*e.g.* air-lock system, bombs, 14 pits sample holder) have been tested for their applicability for high precision $\Delta'^{17}O$ analysis of bioapatite by means of laser fluorination. The results suggest that high precision

results can be obtained by laser fluorination with BrF_5 of chemically pretreated and samples heated to 1000 °C in the $H_2 + N_2$ atmosphere.

We recommend to preheat the bioapatite materials for $\Delta'^{17}O$ at 1000 °C in a H_2+N_2 atmosphere in a furnace for 30 mins first. Before conducting $\Delta'^{17}O$ measurements in the laser fluorination line, extensive pre-fluorination and pre-melting are necessary to achieve stable yields and constant results.

7 Appendix

Supplementary data S1 to this article can be found online at https://data.goettingen-research-online.de/dataset.xhtml?persistentId=doi:10.25625/1IUKIC

8 Acknowledgements

9   References

Ayliffe L. K., Lister A. M. and Chivas A. R. (1992) The preservation of glacial-interglacial climatic signatures in the oxygen isotopes of elephant skeletal phosphate. *Palaeogeogr. Palaeoclimatol. Palaeoecol.* **99**, 179–191.

Blake R. E., O'Neil J. R. and Garcia G. A. (1997) Oxygen isotope systematics of biologically mediated reactions of phosphate: I. Microbial degradation of organophosphorus compounds. *Geochim. Cosmochim. Acta* **61**, 4411–4422.

Bryant D. J. and and Froelich P. N. (1995) A model of oxygen isotope fractionation in body water of large mammals. *Geochim. Cosmochim. Acta* **59**, 4523–4537.

Crowson R. A., Showers W. J., Wright E. K. and Hoering T. C. (1991) Preparation of Phosphate Samples for Oxygen Isotope Analysis. *Anal. Chem.* **63**, 2397–2400.

Dettman D. L., Kohn M. J., Quade J., Ryerson F. J., Ojha T. P. and Hamidullah S. (2001) Seasonal stable isotope evidence for a strong Asian monsoon throughout the past 10.7 m.y. *Geology* **29**, 31–34.

Firsching F. H. (1961) Precipitation of Silver Phosphate from Homogeneous Solution. *Anal. Chem.* **33**, 873–874.

Fricke H. C. and O'Neil J. R. (1996) Inter- and intra-tooth variation in the oxygen isotope composition of mammalian tooth enamel phosphate: Implications for palaeoclimatological and palaeobiological research. *Palaeogeogr. Palaeoclimatol. Palaeoecol.* **126**, 91–99.

Fricke H. C., Clyde W. C., O'Neil J. R. and Gingerich P. D. (1998) Evidence for rapid climate changes in North America during the latest Paleocene thermal maximum: oxygen isotope compositions of biogenic phosphate from the Bighorn Basin (Wyoming). *Earth Planet. Sci. Lett.* **160**, 193–208.

Fricke H. C. and Rogers R. R. (2000) Multiple taxon-multiple locality approach to providing oxygen isotope evidence for warm-blooded theropod dinosaurs. *Geology* **28**, 799–802.

Gehler A., Tütken T. and Pack A. (2011) Triple oxygen isotope analysis of bioapatite as tracer for diagenetic alteration of bones and teeth. *Palaeogeogr. Palaeoclimatol. Palaeoecol.* **310**, 84–91.

Gehler A., Tütken T. and Pack A. (2012) Oxygen and Carbon Isotope Variations in a Modern Rodent Community - Implications for Palaeoenvironmental Reconstructions. *PLoS ONE* **7**, 16–27.

Gehler A., Gingerich P. D. and Pack A. (2016) Temperature and atmospheric CO_2

concentration estimates through the PETM using triple oxygen isotope analysis of mammalian bioapatite. *Proc. Natl. Acad. Sci. U. S. A.* **113**, 7739–7744.

Kohn M. J., Schoeninger M. J. and Barker W. W. (1999) Altered states: Effects of diagenesis on fossil tooth chemistry. *Geochim. Cosmochim. Acta* **63**, 2737–2747.

Kohn M. J. and Cerling T. E. (2002) Stable isotope compositions of biological apatite. *Phosphates Geochemical, Geobiol. Mater. Importance* **48**, 455–488.

Lécuyer C., Grandjean P., O'Neil J. R., Cappetta H. and Martineau F. (1993) Thermal excursions in the ocean at the Cretaceous-Tertiary boundary (northern Morocco): δ^{18}O record of phosphatic fish debris. *Palaeogeogr. Palaeoclimatol. Palaeoecol.* **105**, 235–243.

Lécuyer C., Grandjean P. and Emig C. C. (1996) Phosphate From Living Lingulids : Potential Application To. *Palaeogeogr. Palaeoclimatol. Palaeoecol.* **126**, 101–108.

Lécuyer C. (2004) CHAPTER 22 Oxygen Isotope Analysis of Phosphate. *Analysis* **3**.

Levin N. E., Cerling T. E., Passey B. H., Harris J. M. and Ehleringer J. R. (2006) A stable isotope aridity index for terrestrial environments. *Proc. Natl. Acad. Sci. U. S. A.* **103**, 11201–11205.

Pack A., Gehler A. and Süssenberger A. (2013) Exploring the usability of isotopically anomalous oxygen in bones and teeth as paleo-CO_2-barometer. *Geochim. Cosmochim. Acta* **102**, 306–317.

Pack A., Tanaka R., Hering M., Sengupta S., Peters S. and Nakamura E. (2016) The oxygen isotope composition of San Carlos olivine on the VSMOW2-SLAP2 scale. *Rapid Commun. Mass Spectrom.*, 1495–1504.

Passey B. H., Hu H., Ji H., Montanari S., Li S., Henkes G. A. and Levin N. E. (2014) Triple oxygen isotopes in biogenic and sedimentary carbonates. *Geochim. Cosmochim. Acta* **141**, 1.

Passey B. H. and Levin N. E. (2021) Triple oxygen isotopes in carbonates, biological apatites, and continental paleoclimate reconstruction. *Rev. Mineral. Geochemistry* **86**, 429–626.

Sharp Z. D. (2017) Principles_of_Stable_Isotope_Geochemistry_2nd_Edition- Sharp.

Shemesh A., Kolodny Y. and Luz B. (1983) Oxygen isotope variations in phosphate of biogenic apatites, II. Phosphorite rocks. *Earth Planet. Sci. Lett.* **64**, 405–416.

Tudge A. P. (1960) A method of analysis of oxygen isotopes in orthophosphate-its use in the measurement of paleotemperatures. *Geochim. Cosmochim. Acta* **18**, 81–93.

Tütken T., Vennemann T. W., Janz H. and Heizmann E. P. J. (2006) Palaeoenvironment and

palaeoclimate of the Middle Miocene lake in the Steinheim basin, SW Germany: A reconstruction from C, O, and Sr isotopes of fossil remains. *Palaeogeogr. Palaeoclimatol. Palaeoecol.* **241**, 457–491.

Tütken T. and Vennemann T. (2009) Stable isotope ecology of Miocene large mammals from Sandelzhausen, southern Germany. *Palaontologische Zeitschrift* **83**, 207–226.

Vennemann T. W. and Hegner E. (1998) Oxygen, strontium, and neodymium isotope composition of fossil shark teeth as a proxy for the palaeoceanography and palaeoclimatology of the Miocene northern Alpine Paratethys. *Palaeogeogr. Palaeoclimatol. Palaeoecol.* **142**, 107–121.

Vennemann T. W., Hegner E., Cliff G. and Benz G. W. (2001) Isotopic composition of recent shark teeth as a proxy for environmental conditions. *Geochim. Cosmochim. Acta* **65**, 1583–1599.

Vennemann T. W., Fricke H. C., Blake R. E., O'Neil J. R. and Colman A. (2002) Oxygen isotope analysis of phosphates: A comparison of techniques for analysis of Ag_3PO_4. *Chem. Geol.* **185**, 321–336.

Chapter 6 Conclusions

High precision triple oxygen isotope analysis of bioapatite allows exploring subtle variations in the $\Delta'^{17}O$ values of tooth and bones enamel(oid) from marine vertebrates, terrestrial mammals, birds and fossil samples. This thesis proves that high precision triple oxygen isotope ratios of bioapatite is a compelling proxy to reconstruct the paleo CO_2 concentration. In particular we demonstrate that:

1) Our novel methodological approach, involving chemical pretreatment and high temperature heating of powdered tooth enamel, combined with laser fluorination dual inlet-IRMS technique is suitable for obtaining high precision triple oxygen isotope data of bioapatite. On average, an analytical uncertainty of ± 11 ppm (1σ SD) is obtained for $\Delta'^{17}O$ values.

2) $\Delta'^{17}O$ values for both sharks and marine mammals plot below the theoretical sea water-apatite equilibrium curve. This anomaly is larger for marine mammals, respect to sharks, suggesting a high water use efficiency for these vertebrates. Dolphin-sized fossil mammals or metabolically-similar marine vertebrates may well be used as new paleo-CO_2 barometer.

3) The combined use of tooth enamel $\delta^{13}C$ and $\delta^{18}O_{CO3}$ values is helpful to distinguish a suite of modern terrestrial mammals according to their eating habits and provenance, while $\Delta'^{17}O_{AP}$ values reflect differences in the physiology of the different taxa. Moreover, intra-population $\Delta'^{17}O_{AP}$ heterogeneity can be ascribed to individual differences in physiological parameters and behaviors, potentially related to different body masses and sex.

4) The mammalian $\Delta'^{17}O_{AP}$ of the phosphate group systematically decreases with body mass. This can be explained by the fact small mammals have higher metabolic rates compared to to larger taxa, which lead to the incorporation of a more negative $\Delta'^{17}O$ anomaly into their tooth enamel. Sensitivity analyses of $\Delta'^{17}O_{AP}$ reveal that tooth enamel from small fossil mammals most precisely records variations in $\Delta'^{17}O_{Air}$. This makes high precision triple oxygen isotope analysis of tooth enamel(oid) from fossil small mammals suitable for paleo-CO_2 reconstruction.

5) Modern birds overlap with terrestrial mammals in a triple oxygen isotope plot. The tooth enamels of measured Mesozoic dinosaurs show anomalous $\Delta'^{17}O$ values. By combining these analytical findings with mass balance modelling, developed for terrestrial mammals, we estimate much higher paleo atmospheric CO_2 concentrations than today. In particular, we obtain pCO_2 values of 817 ± 579 ppmv for Late Cretaceous and of 1605 ± 934 ppmv for the Late Jurassic atmosphere. pCO_2 data from different proxies corroborate our results, confirming that $\Delta'^{17}O$ of tooth enamel is a powerful tool for paleoenvironmental studies.

List of publications

The following lists all articles that are published, in press or in preparation during the time of the PhD study.

Peer-reviewed journals:

1. **Dingsu Feng**, Thomas Tütken, Niklas Löffler, Gert Tröster, Andreas Pack. 2021. Isotopically anomalous metabolic oxygen in marine vertebrates as physiology and atmospheric proxy. *Geochimica et Cosmochimica Acta*, **in review**.

2. **Dingsu Feng**, Jakub Surma, Niklas Löffler, Thomas Tütken, Gisa Hoffmann, Gert Tröster, Fabian Zahnow, Andreas Pack. 2021. Triple oxygen isotopes of modern terrestrial mammalian tooth enamel and body water. *Earth and Planetary Science Letters*, **in preparation**.

3. **Dingsu Feng**, Thomas Tütken, Niklas Löffler, Gisa Hoffmann, Gert Tröster, Andreas Pack. 2022. Late Jurassic and late Cretaceous paleo CO_2 concentration through dinosaurs tooth enamel. *Proceedings of the National Academy of Sciences of the United States of America*, **in preparation**.

4. Alicja Wudarska, Michael Wiedenbeck, Ewa Slaby, Malgorzata Lempart-Drozd, Chris Harris, Michael M. Joachimski, Christophe Lécuyer, Kenneth MacLeod, Andreas Pack, Torsten Vennemann, Frédéric Couffignal, **Dingsu Feng**, Johannes Glodny, Christof Kusebauch, Sathish Mayanna, Alexander Rocholl, Laura Speir, Yadong Sun, Franziska D.H. Wilke. 2021. Inter-laboratory characterization of apatite reference materials for oxygen isotope analysis and associated methodoiogical considerations. *Geostandards and Geoanalytical Research*, **in press**.

5. Peters Stefan TM, **Feng Dingsu**, Troll Valentin, Pack Andreas, Tornos Fernando, Andersson Ulf, Lehmann Bernd, Tommaso Di Rocco. 2021. Ubiquitous evaporite-derived oxygen in magnetite-apatite deposits. *Nature Communications*, **in review**.

Conference abstracts:

1. **Dingsu Feng**, Thomas Tütken, Jochen Hoefs, Andreas Pack. 2021. Triple oxygen isotope fractionation exponent between apatite and water. *Goldschmidt Leon 2021*.

2. **Dingsu Feng**, Thomas Tütken, Andreas Pack. 2019. Triple oxygen isotope composition of bioapatite. *Goldschmidt Barcelona 2019*.

3. **Dingsu Feng**, Andreas Pack. 2019. The relation between $\Delta'^{17}O$ and body mass for bioapatite. *GeoMünster 2019*.

4. Christian von Sperber, Andreas Pack, Tommaso Di Rocco, **Dingsu Feng**, Daniel Herwartz. 2022. Tracing phosphorus in the soil-plant system using triple oxygen isotope systematics. *World Congress Soil Science 2022*.

5. Daniel Herwartz, Andreas Pack, Tommaso Di Rocco, **Dingsu Feng**, Christian von Sperber. 2021. Identification of metabolic and enzymatic pathways in the phosphorus cycle using triple oxygen isotope systematics. *Goldschmidt Leon 2021*.

6. Peters Stefan, **Feng Dingsu**, Troll Valentin, Pack Andreas, Tornos Fernando, Andersson Ulf, Lehmann Bernd, Tommaso Di Rocco. 2021. Ubiquitous evaporite-derived oxygen in magnetite-apatite deposits. *The Gerontological Society of America 2021*.

7. Andreas pack, Meike Fischer, Christian Stübler, Stefan Peters, **Dingsu Feng**. 2020. Tracing the triple isotope composition of air by high-precision analyses of meteorites, rocks and fossils. *22nd EGU General Assembly 2020*.

Curriculum vitae

I was born in Renhuai, Guizhou province, China, completed a Bachelors of Natural Resources Prospecting Engineering (Solid Mineral) in China University of Geosciences in Beijing in 2014. I continued the bachelor work and earned a M.S. of Mineralogy, Petrology, Mineral Deposit Geology under Prof. Dr. Jingwen Mao in 2017. I have published 2 articles during my master study. Afterwards, I attended University of Göttingen to work as a PhD student under Prof. Dr. Andreas Pack in 2017. I have been an author on 5 studies and have presented my research at Goldschmidt conferences, GeoBonn, GeoMünster, DMG meeting Heidelberg 2019, and Geowissenschaftliches Kolloquium Göttingen during my PhD study.